E-ISSN: 2147-1959

MIRT

Molecular Imaging and Radionuclide Therapy

June 2026 Volume 35 Issue 2 www.tsnm.org

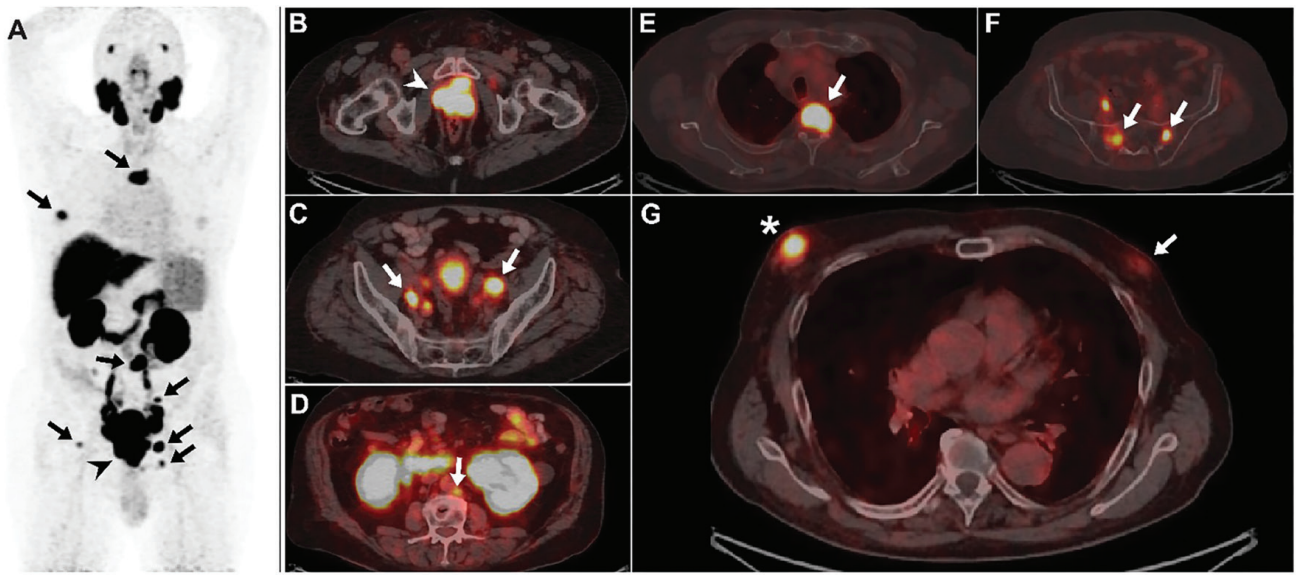

"Official Journal of the Turkish Society of Nuclear Medicine"

galenos yayınevi

TURKISH SOCIETY OF NUCLEAR MEDICINE 1975

MIRT

Molecular Imaging and Radionuclide Therapy

The Ownership: Turkish Society of Nuclear Medicine (TSNM)
Turkish Society of Nuclear Medicine
Address: Aziziye Mah. Pilot Sk. 10/12, Çankaya/Ankara, Türkiye
e-mail: dernekmerkezi@tsnm.org · Tel: +90 312 441 00 45

Publishing Manager
Prof. Elif Özdemir, MD.
Ankara Yıldırım Beyazıt University Faculty of Medicine, Department of Nuclear Medicine;
E-mail: ozdemire80@gmail.com

Editor in Chief
Prof. Murat Fani Bozkurt, MD, FEBNM
FEBNM Hacettepe University, Medical School, Department of Nuclear Medicine, Ankara, Türkiye
E-mail: fanibozkurt@gmail.com

Associate Editors
Prof. Nalan Selçuk, MD.
Yeditepe University, Medical School, Department of Nuclear Medicine, İstanbul, Türkiye
E-mail: nalanselcuk@yeditepe.edu.tr

Prof. Çiğdem Soydal, MD.
FEBNM, Ankara University Medical School, Department of Nuclear Medicine, Ankara, Türkiye
Email: csoydal@yahoo.com; csoydal@ankara.edu.tr

Statistics Editors
Prof. Gül Ergör, MD.
Dokuz Eylül University, Medical School, Department of Public Health, İzmir, Türkiye
E-mail:gulergor@deu.edu.tr

Prof. Sadettin Kılıçkap, MD.
Hacettepe University, Medical School, Department of Preventive Oncology, Ankara, Türkiye
E-mail: skilickap@yahoo.com

English Language Editor
Galenos Publishing House

MIRT

Molecular Imaging and Radionuclide Therapy

Turkish Society of Nuclear Medicine
Cinnah Caddesi Pilot Sokak No: 10/12 Çankaya 06650 Ankara, Türkiye **Phone:** +90 312 441 00 45 **Fax:** +90 312 441 12 95 **Web:** www.tsnm.org **E-mail:** dernekmerkezi@tsnm.org
"Formerly Turkish Journal of Nuclear Medicine"

Reviewing the articles' conformity to the publishing standards of the Journal, typesetting, reviewing and editing the manuscripts and abstracts in English, creating links to source data, and publishing process are realized by Galenos.

Publisher Contact

Address: Molla Gürani Mah. Kaçamak Sk. No: 21/1 34093 İstanbul, Türkiye
Phone: +90 (530) 177 30 97 / +90 (539) 307 32 03
E-mail: info@galenos.com.tr/yayin@galenos.com.tr
Web: www.galenos.com.tr
Publisher Certificate Number: 14521

Online Publication Date: June 2026
ISSN: 2146-1414 **E-ISSN:** 2147-1959

International scientific journal published quarterly.

MIRT

Molecular Imaging and Radionuclide Therapy

Please refer to the journal's webpage **(https://mirt.tsnmjournals.org/)** for "Aims and Scope", "Instructions to Authors" and "Ethical Policy".

The editorial and publication process of Molecular Imaging and Radionuclide Therapy are shaped in accordance with the guidelines of ICMJE, WAME, CSE, COPE, EASE, and NISO. The journal is in conformity with the Principles of Transparency and Best Practice in Scholarly Publishing.

Molecular Imaging and Radionuclide Therapy is indexed in **Pubmed, Pubmed Central (PMC), Emerging Sources Citation Index (ESCI), TUBITAK-ULAKBIM, Scopus, Gale/Cengage Learning, EBSCO databases, ProQuest Health** & **Medical Complete, CINAHL, Embase, J-Gate, IdealOnline, Türkiye Atıf Dizini-Turkiye Citation Index, Turk Medline, Hinari, GOALI, ARDI, OARE, AGORA** and **CNKI**.

The journal is published electronically.

Owner: Turkish Society of Nuclear Medicine

Responsible Manager: Murat Fani Bozkurt

MIRT
Molecular Imaging and Radionuclide Therapy

CONTENTS

Original Articles

Interesting Images

MIRT
Molecular Imaging and Radionuclide Therapy

CONTENTS

Original Article

Mol Imaging Radionucl Ther 2026;35(2):85-91 **DOI:***10.4274/mirt.galenos.2026.93764*

Diagnostic Value of ^{68}Ga-FAPI PET/CT Versus ^{18}F-FDG PET/CT in Laryngeal Cancer Staging

Laringeal Kanser Evrelemesinde ^{68}Ga-FAPI PET/BT ile ^{18}F-FDG PET/BT'nin Karşılaştırılması

Ebuzer Kalender, Edanur Ekinci Yıldırım, Buket Eren, Umut Elboğa, Ertan Şahin

Gaziantep University Faculty of Medicine, Department of Nuclear Medicine, Gaziantep, Türkiye

Abstract

Objectives: To investigate whether gallium-68 fibroblast activation protein inhibitor positron emission tomography/computed tomography ^{68}Ga-FAPI PET/CT is superior to ^{18}F-fluorodeoxyglucose positron emission tomography (^{18}F-FDG) PET/CT in the staging of patients with laryngeal cancer (LC).

Methods: A total of 14 patients diagnosed with LC were retrospectively included in the study, of whom 13 were male and 1 female, with a mean age of 65 years. All participants were initially referred to our department for staging with ^{18}F-FDG PET/CT. Subsequently, each patient underwent a ^{68}Ga-FAPI PET/CT scan three days following the ^{18}F-FDG PET/CT. Both sets of imaging studies were independently evaluated by two experienced nuclear medicine physicians, and the findings were systematically compared to assess potential differences in diagnostic performance.

Results: The median maximum standard uptake values (SUV_{max}) of primary tumors was significantly higher in ^{68}Ga-FAPI PET/CT 10.95; range: 3.5-19.2) compared to ^{18}F-FDG PET/CT (4.85; range: 2.2-10.9). Lymph node involvement was observed on FDG scans in 3 patients, in ipsilateral levels 2 and/or 3, with a median SUV_{max} of 3.7 (range: 2.4-4.1). FAPI PET/CT also detected lymph node involvement at the same levels in 3 patients, with a notably higher SUV_{max} of 7.9 (range: 6.8-10.4).

Conclusion: In this study, our results suggest that ^{68}Ga-FAPI PET/CT demonstrates superior radiotracer uptake in both primary tumors and lymph nodes, which may enhance detection sensitivity for LC staging compared with ^{18}F-FDG PET/CT. Nevertheless, further prospective studies with larger patient populations are warranted to validate these preliminary observations and determine the clinical value of this emerging imaging modality.

Keywords: Laryngeal cancer, ^{68}Ga-FAPI PET/CT, ^{18}F-FDG PET/CT

Öz

Amaç: Bu çalışmanın amacı, galyum-68 fibroblast aktivasyon protein inhibitörü pozitron emisyon tomografisi/bilgisayarlı tomografi (^{68}Ga-FAPI PET/BT) yönteminin, ^{18}F-florodeoksiglukoz pozitron emisyon tomografisi (^{18}F-FDG) PET/BT ile karşılaştırıldığında larinks kanseri (LC) hastalarının evrelendirilmesinde üstün olup olmadığını araştırmaktır.

Yöntem: Çalışmaya, LC tanısı almış 14 hasta retrospektif olarak dahil edilmiştir. Hastaların 13'ü erkek, 1'i kadın olup ortalama yaş 65 olarak bulunmuştur. Tüm katılımcılar başlangıçta bölümümüze ^{18}F-FDG PET/BT ile evreleme amacıyla yönlendirilmiştir. Daha sonra her hastaya ^{18}F-FDG PET/BT çekiminden üç gün sonra ^{68}Ga-FAPI PET/BT görüntülemesi uygulanmıştır. Her iki görüntüleme yöntemi iki deneyimli nükleer tıp uzmanı tarafından bağımsız olarak değerlendirilmiş ve tanısal performanstaki olası farklılıkları belirlemek amacıyla bulgular sistematik olarak karşılaştırılmıştır.

Address for Correspondence: Ebuzer Kalender, Gaziantep University Faculty of Medicine, Department of Nuclear Medicine, Gaziantep, Türkiye
E-mail: dr.ebuz@hotmail.com **ORCID ID:** orcid.org/0000-0001-8472-3174
Received: 13.08.2025 **Accepted:** 23.01.2026 **Epub:** 16.03.2026 **Publication Date:** 04.06.2026

Cite this article as: Kalender E, Ekinci Yıldırım E, Eren B, Elboğa U, Şahin E. Diagnostic value of ^{68}Ga-FAPI PET/CT versus ^{18}F-FDG PET/CT in laryngeal cancer staging. Mol Imaging Radionucl Ther. 2026;35(2):85-91.

Bulgular: Primer tümörlerin medyan maksimum standart tutulum değeri (SUV_{maks}), ^{68}Ga-FAPI PET/BT'de (10,95; aralık: 3,5-19,2), ^{18}F-FDG PET/BT'ye göre (4,85; aralık: 2,2-10,9) anlamlı derecede daha yüksek bulunmuştur. Lenf nodu tutulumu FDG görüntülemelerinde 3 hastada, ipsilateral seviye 2 ve/veya 3'te gözlenmiş olup medyan SUV_{maks} 3,7 (aralık: 2,4-4,1) olarak saptanmıştır. FAPI PET/BT'de aynı seviyelerde 3 hastada lenf nodu tutulumu göstermiş, ancak SUV_{maks} değeri belirgin şekilde daha yüksek (7,9; aralık: 6,8-10,4) bulunmuştur.

Sonuç: Bu çalışmanın sonuçları, ^{68}Ga-FAPI PET/BT'nin hem primer tümörlerde hem de lenf nodlarında daha yüksek radyotracer tutulumu gösterdiğini, bunun da larinks kanseri evrelemesinde ^{18}F-FDG PET/BT'ye kıyasla saptama duyarlılığını artırabileceğini düşündürmektedir. Bununla birlikte, bu ön bulguların doğrulanması ve bu yeni görüntüleme yönteminin klinik değerinin belirlenmesi için daha geniş hasta popülasyonlarını içeren ileriye dönük çalışmalara ihtiyaç vardır.

Anahtar Kelimeler: Laringeal kanser, ^{68}Ga-FAPI PET/BT, ^{18}F-FDG PET/BT

Introduction

Laryngeal cancer (LC) constitutes a significant proportion of head and neck malignancies, accounting for approximately 25% of all cases (1). The predominant histological subtype is squamous cell carcinoma (SCC), which comprises nearly 90% of LC cases and can arise in any region of the larynx. The disease exhibits a marked male predominance in incidence rates. Precise staging of LC is critical for guiding treatment decisions and estimating prognosis. Imaging techniques are indispensable in this context. Conventional modalities such as computed tomography (CT) and magnetic resonance imaging (MRI) are routinely utilized for staging; however, their sensitivity in differentiating metastatic from non-metastatic lymph nodes remains suboptimal (2,3). In contrast ^{18}F-fluorodeoxyglucose positron emission tomography/CT (^{18}F-FDG PET/CT) offers added value in initial staging, restaging, evaluation of therapeutic response, and the detection of locoregional and distant metastases during follow-up (3,4).

Fibroblast activation protein (FAP), primarily expressed by cancer-associated fibroblasts (CAFs), plays an instrumental role in tumor development and progression. Its upregulation across various tumor types has made it an attractive target for novel molecular imaging strategies. Gallium-68-labeled FAP inhibitors (^{68}Ga FAPI), used in PET/CT imaging, have shown promising results, particularly in malignancies where ^{18}F-FDG PET/CT demonstrates limited efficacy. The aim of the present study is to investigate the potential superiority of ^{68}Ga-FAPI PET/CT over ^{18}F-FDG PET/CT in staging patients with LC. To our knowledge, no previous studies have directly compared these two modalities in this specific clinical context. Therefore, this research may serve as a novel and foundational contribution to the existing body of literature.

Materials and Methods

This retrospective study was approved by the Clinical Research Ethics Committee of Gaziantep University (approval no: 2025/173, date: 06.08.2025). All procedures were conducted in accordance with the ethical standards of the institutional and/or national research committee and with the 1964 Declaration of Helsinki and its later amendments. A total of 14 patients diagnosed with LC were retrospectively included in the study, of whom 13 were male and 1 female, with a mean age of 65 years (range: 43-75). In all cases, the diagnosis of SCC was confirmed by histopathological analysis. All participants were initially referred to our department for staging with ^{18}F-FDG PET/CT. Subsequently, each patient underwent a ^{68}Ga-FAPI PET/CT scan three days following the ^{18}F-FDG PET/CT. All participants signed informed consent forms before undergoing either procedure. Both sets of imaging studies were independently evaluated by two experienced nuclear medicine physicians, and the findings were systematically compared to assess potential differences in diagnostic performance.

Patient Preparation and Imaging Protocol

Prior to ^{18}F-FDG PET/CT imaging, all patients were instructed to fast for a minimum of six hours and to discontinue any intravenous glucose infusions during this period to minimize non-specific uptake. Blood glucose levels were measured via finger-prick testing immediately before tracer administration and were required to be ≤150 mg/dL for the scan to proceed. Following this, ^{18}F-FDG was administered intravenously at a dose ranging from 3.5 to 5.5 MBq/kg of body weight. For the ^{68}Ga-FAPI PET/CT scan, the radiotracer was injected intravenously at a dose of 2 MBq/kg. Both PET/CT scans were acquired using a Discovery IQ PET/CT system (GE Healthcare, Milwaukee, WI, USA), equipped with five detector rings and a transaxial field of view of 20 cm. Image acquisition began approximately 60 minutes post-injection for both tracers. Whole-body PET/CT imaging was performed from the vertex of the skull to the mid-thigh in the supine position. The CT component was used for attenuation correction and anatomical localization and was acquired using the following parameters: 120 kVp, 80 mAs per slice, a scan field of view of 700 mm, no interslice gap, 64 × 0.625-mm

collimation, and a 3.3-mm slice thickness. PET images were acquired in three-dimensional mode, maintaining the same patient positioning as the CT scan. The acquisition time per bed position was 2.5 minutes, ensuring adequate coverage and image quality. All images were reconstructed and analyzed using the system's dedicated software platform.

Image-Analysis

All PET/CT images were independently interpreted by two board-certified nuclear medicine physicians, each blinded to the other's assessment to minimize observer bias. Image evaluation included multiplanar reconstructions (axial, coronal, and sagittal) of the PET, CT, and fused datasets to ensure comprehensive lesion localization and characterization. Semi-quantitative analysis was performed using dedicated image-processing software (AW VolumeShare; GE Healthcare). Radiotracer uptake was assessed using the maximum standard uptake value (SUV_{max}) for both ^{18}F-FDG and ^{68}Ga-FAPI scans. For each lesion, volumes of interest were manually delineated on three orthogonal planes to ensure accurate measurement and avoid partial volume effects SUV_{max} values were recorded for all detectable primary tumors as well as regional and distant metastatic lesions. These values served as the primary metrics for comparing the metabolic activity and diagnostic performance of the two radiotracers.

Statistical Analysis

All statistical analyses were performed using SPSS software (version 27, IBM Corp., Armonk, NY, USA). Descriptive statistics were presented as mean, median, minimum, and maximum values for continuous variables, and as frequencies (percentages) for categorical variables. The Wilcoxon signed-rank test was used to compare paired non-parametric SUV_{max} values between FDG and FAPI PET/CT scans. Spearman's rank correlation coefficient (ρ) was used to evaluate the strength and direction of associations between SUV_{max} values and clinical parameters such as age, primary tumor localization, and lymph node involvement. A p-value of <0.05 was considered statistically significant.

Results

A summary of patient demographics and imaging findings is shown in Table 1. A total of 14 patients [13 males (92.9%) and 1 female (7.1%)] with a mean age of 65 years (range: 43-75) were included in the study. The mean duration of smoking among the patients was 35.1 years (range: 25-50). All patients were histopathologically diagnosed with SCC. The most common tumor localization was glottic (64.3%), followed by supraglottic (28.6%) and subglottic (7.1%). The median SUV_{max} of primary tumors was significantly higher on ^{68}Ga-FAPI PET/CT (10.95; range: 3.5-19.2) than on ^{18}F-FDG PET/CT (4.85; range: 2.2-10.9) (Figure 1). Lymph node involvement was observed in 3 patients on FDG scans, located in ipsilateral level 2 and/or level 3, with a median SUV_{max} of 3.7 (range: 2.4-4.1). ^{68}Ga-FAPI PET/CT also detected lymph node involvement at the same levels in 3 patients, with a notably higher SUV_{max} of 7.9 (range: 6.8-10.4). No distant metastases were identified with either imaging modality (Table 1).

No statistically significant differences in SUV_{max} values across tumor localizations were observed for either FDG or FAPI (p>0.05).

Correlation analysis between SUV_{max} and the variables is shown in Table 2. A moderate positive correlation (r=0.46) was observed between FDG and FAPI SUV_{max} values; however, it was not statistically significant at the 0.05 level (p=0.098). The correlation between age and FDG SUV_{max} was weakly negative (r=-0.035, p=0.905),

Table 1. Summary of patient demographics and imaging findings (n=14)

Variable	Median (min-max), n (%)
Age (years)	65 (43-75)
Gender	
Male	13 (92.9%)
Female	1 (7.1%)
Smoking history	35.1 (25-50)
Pathology subtype	
SCC	14 (100.0%)
Primary tumor localization	
Glottic	9 (64.3%)
Subglottic	1 (7.1%)
Supraglottic	4 (28.6%)
FDG primary SUV	4.85 (2.2-10.9)
FAPI primary SUV	10.95 (3.5-19.2)
Lymph node FDG (location)	
Level 2	1 (7.14%)
Level 2 and 3	2 (14.28%)
Lymph node FDG (SUV)	3.7 (2.4-4.1)
Lymph node FAPI (SUV)	7.9 (6.8-10.4)
Lymph node FAPI (location)	
Level 2 and 3	2 (14.28%)
Level 2, 3, and 4	1 (7.14%)
Metastasis FDG	0
Metastasis FAPI	0

SCC: Squamous cell carcinoma, FDG: Fluorodeoxyglucose, SUV: Standard uptake value, FAPI: FAP inhibitor

while the correlation between age and FAPI SUV_{max} was nearly negligible and weakly positive (r=0.009, p=0.976). The correlation between age and FDG SUV_{max} was weakly negative (r=-0.04, p=0.905), while that between age and FAPI SUV_{max} was very weakly positive (r=0.01, p=0.976). A strong and statistically significant positive correlation was found between lymph node FDG SUV and FDG SUV_{max} (r=0.76, p=0.002), as well as between lymph node FDG SUV and FAPI SUV_{max} (r=0.59, p=0.015). Additionally, a statistically significant, moderate-to-strong correlation was observed between lymph node FAPI SUV and both FDG SUV_{max} (r=0.52, p=0.018) and FAPI SUV_{max} (r=0.63, p=0.008) (Table 2).

Table 2. Correlation analysis of between SUV_{max} and variables

Variables	FDG SUV_{max}	FAPI SUV_{max}
FDG SUV_{max} (p-value)	-	0.098
Correlation coefficient (r)	-	0.46
Age (p-value)	0.905	0.976
Correlation coefficient (r)	-0.04	0.01
Lymph node FDG (SUV) (p-value)	0.002	0.015
Correlation coefficient (r)	0.76	0.59
Lymph node FAPI (SUV) (p-value)	0.018	0.008
Correlation coefficient (r)	0.52	0.63

FDG: Fluorodeoxyglucose, FAPI: FAP inhibitor SUV_{max}: Maximum standard uptake value

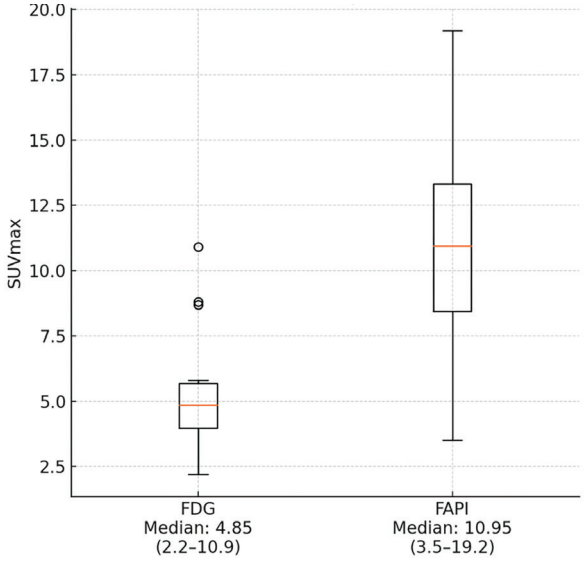

Figure 1. Comparison of FDG and FAPI SUV_{max} values with median and range in primary laryngeal tumors
SUV_{max}: Maximum standard uptake values, FDG: fluorodeoxyglucose, FAPI: FAP inhibitors

Discussion

LC is a relatively common malignancy of the respiratory tract and represents a significant subset of head and neck cancers (5). SCC is the predominant histological subtype and can arise from any anatomical region of the larynx. In contrast, rare histological variants, such as sarcomas, malignant melanomas, lymphomas, and minor salivary gland carcinomas, are infrequently encountered (6). Approximately 98% of LC originate in the glottic or supraglottic regions, with glottic tumors occurring nearly three times as often as supraglottic tumors. Subglottic cancers are rare, accounting for only about 2% of cases (7). Our findings are similar. The disease shows a clear male predominance, with a male-to-female ratio of approximately 3:1, and its incidence increases with advancing age. The pathogenesis of LC is multifactorial, with tobacco use and alcohol consumption recognized as the most significant risk factors. Smoking, in particular, shows a linear dose-response relationship with LC development and increases the risk 10-15-fold compared with non-smokers (8,9).

Management of LC is complex because of the larynx's essential roles in respiration, phonation, and swallowing. Treatment goals include complete tumor eradication, prevention of recurrence, and preservation of laryngeal function. The choice of treatment is primarily guided by the tumor's stage and anatomical subsite, as outcomes vary by location. Glottic tumors typically yield the highest success rates, followed by supraglottic and subglottic tumors (10). However, approximately 60% of patients are diagnosed at an advanced stage (11), often with deep tissue invasion and cartilage involvement (12). Early lymphatic dissemination is a defining feature of supraglottic carcinomas, with clinical nodal metastases identified in approximately 55% of patients at the time of diagnosis. Contralateral nodal involvement is observed in approximately 16% of cases. Cervical lymph node levels II, III, and IV are most frequently implicated (13).

Treatment modalities include surgery, radiotherapy, chemotherapy, or a combination thereof, with emerging interest in targeted therapies. Accurate staging is fundamental for selecting optimal treatment strategies and estimating prognosis. Understanding the specific patterns of tumor spread is equally critical, as it directly influences therapeutic planning. Detailed anatomical and pathological evaluation allows for maximal oncologic control while preserving organ function. The diagnostic workup for LC begins with a comprehensive clinical history and physical examination, followed by direct laryngoscopy to visualize the lesion and obtain biopsy samples for histological confirmation. These steps are essential for accurate staging and subsequent management. Imaging modalities serve as

crucial adjuncts to physical and endoscopic examination, enabling evaluation of local invasion, nodal involvement, and distant metastases (14,15).

CT, MRI, and PET are the primary imaging tools utilized in LC assessment (14). While CT and MRI are both integral to staging, MRI has demonstrated superior ability to detect cartilage invasion, perineural invasion and marrow involvement, and extracapsular spread (14,15,16,17). However, both modalities are frequently used complementarily, as they offer distinct advantages in delineating tumor extent and guiding therapeutic decisions. Despite their utility, conventional imaging (CI) often falls short in differentiating metastatic from benign lymphadenopathy (2,3). In this context, ^{18}F-FDG PET/CT has become an indispensable imaging modality for staging, response assessment, and long-term follow-up in LC patients (3,4). It also facilitates the detection of nodal metastases, distant lesions, and synchronous primary tumors (18). Notably, a retrospective study reported that PET/CT findings altered clinical management in approximately 31% of LC cases (18). While several studies have indicated that ^{18}F-FDG PET/CT and CI provide comparable diagnostic accuracy in LC (3,4,19,20), PET/CT offers superior sensitivity in detecting distant metastases due to whole-body coverage. However, its limited spatial resolution may hinder precise delineation of the primary tumor and T-staging (21). Recent advances have introduced hybrid PET/MRI as a promising modality, combining the functional benefits of PET with the superior soft-tissue contrast of MRI (22).

FAP, a serine protease selectively overexpressed in CAFs, is implicated in various oncogenic processes, including tumor proliferation, immune evasion, angiogenesis, extracellular matrix remodeling, and metastasis (23). Due to its minimal expression in normal tissues, FAP has emerged as a highly promising molecular target for both imaging and therapeutic applications (24,25,26). FAP-targeted radiotracers exhibit favorable pharmacokinetics, high tumor-to-background ratios, and broad applicability across various solid tumors (25). ^{68}Ga-FAPI have recently attracted attention as a novel class of radiotracers that may be superior to ^{18}F-FDG for oncologic imaging. Numerous studies have demonstrated enhanced sensitivity of ^{68}Ga-FAPI PET/CT for detecting both primary and metastatic lesions across a range of malignancies, including hepatocellular carcinoma, lung adenocarcinoma, gastrointestinal stromal tumors, gastric signet-ring cell carcinoma, and other metastatic malignancies (25,26,27,28,29,30).

In a study by Gu et al. (31), ^{68}Ga-FAPI PET/CT demonstrated improved detection rates of primary tumors in patients with head and neck cancers of unknown primary origin, particularly when ^{18}F-FDG PET/CT was negative. Similarly, Bhat et al. (32) reported a high diagnostic accuracy for ^{68}Ga-FAPI PET/CT, with a sensitivity of 88.3% and a specificity of 95.8% in a cohort of 41 patients with head and neck malignancies, including eight cases of LC.

Study Limitations

In our study, the small total number of patients and small subgroup sizes limited our ability to conduct reliable statistical analyses. Therefore, further prospective case-control studies with larger sample sizes and standardized methods are needed.

Conclusion

In this study, our results suggested that ^{68}Ga-FAPI PET/CT demonstrated superior radiotracer uptake in both primary tumors and lymph nodes, which may enhance detection sensitivity for LC staging compared with ^{18}F-FDG PET/CT (Figure 2). Nevertheless, further prospective studies with larger patient populations are warranted to validate these

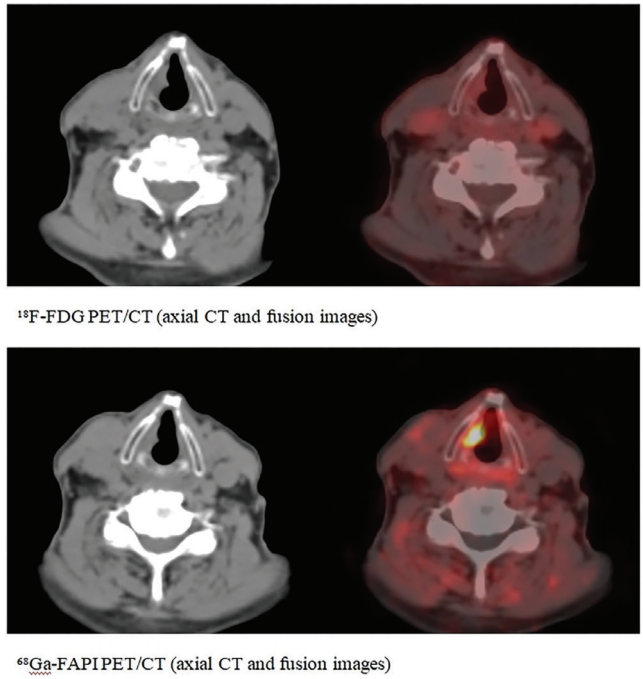

Figure 2. A 69-year-old man was diagnosed with glottic squamous cell carcinoma of the larynx. While the primary lesion in the right glottic region demonstrated low ^{18}F-FDG uptake (SUV_{max}: 2.2), it exhibited significantly increased uptake of ^{68}Ga-FAPI (SUV_{max}: 13.9), which is of particular note

^{68}Ga-FAPI PET/CT: Gallium-68 fibroblast activation protein inhibitor positron emission tomography/computed tomography, SUV_{max}: Maximum standard uptake value, FAPI: FAP inhibitors, ^{18}F-FDG: ^{18}F-fluorodeoxyglucose

preliminary observations and determine the clinical value of this emerging imaging modality.

Ethics

Ethics Committee Approval: This retrospective study was approved by the Clinical Research Ethics Committee of Gaziantep University (approval no: 2025/173, date: 06.08.2025). All procedures were conducted in accordance with the ethical standards of the institutional and/or national research committee and with the 1964 Declaration of Helsinki and its later amendments.

Informed Consent: This is retrospective study.

Footnotes

Authorship Contributions

Surgical and Medical Practices: U.E., Concept: B.E., E.Ş., Design: U.E., Data Collection or Processing: E.E.Y., E.Ş., Analysis or Interpretation: B.E., Literature Search: E.K., Writing: E.K.

Conflict of Interest: No conflict of interest was declared by the authors.

Financial Disclosure: The authors declared that this study has received no financial.

References

1. Parkin DM, Bray F, Ferlay J, Pisani P. Global cancer statistics, 2002. CA Cancer J Clin. 2005;55:74-108.
2. Kyzas PA, Evangelou E, Denaxa-Kyza D, Ioannidis JP. ^{18}F-fluorodeoxyglucose positron emission tomography to evaluate cervical node metastases in patients with head and neck squamous cell carcinoma: a meta-analysis. J Natl Cancer Inst. 2008;100:712-720.
3. Gao S, Li S, Yang X, Tang Q. 18FDG PET-CT for distant metastases in patients with recurrent head and neck cancer after definitive treatment. A meta-analysis. Oral Oncol. 2014;50:163-167.
4. Yongkui L, Jian L, Wanghan, Jingui L. 18FDG-PET/CT for the detection of regional nodal metastasis in patients with primary head and neck cancer before treatment: a meta-analysis. Surg Oncol. 2013;22:e11-e16.
5. Steuer CE, El-Deiry M, Parks JR, Higgins KA, Saba NF. An update on larynx cancer. CA Cancer J Clin. 2017;67:31-50.
6. Doğan S, Vural A, Kahriman G, İmamoğlu H, Abdülrezzak Ü, Öztürk M. Non-squamous cell carcinoma diseases of the larynx: clinical and imaging findings. Braz J Otorhinolaryngol. 2020;86:468-482.
7. Virtaniemi JA, Hirvikoski PP, Kumpulainen EJ, Johansson RT, Pukkala E, Kosma VM. Is the subsite distribution of laryngeal cancer related to smoking habits? Acta Oncol. 2000;39:77-79.
8. Rothman KJ, Cann CI, Flanders D, Fried MP. Epidemiology of laryngeal cancer. Epidemiol Rev. 1980;2:195-209.
9. Kuper H, Boffetta P, Adami HO. Tobacco use and cancer causation: association by tumour type. J Intern Med. 2002;252:206-224.
10. Department of Veterans Affairs Laryngeal Cancer Study Group; Wolf GT, Fisher SG, Hong WK, Hillman R, Spaulding M, Laramore GE, Endicott JW, McClatchey K, Henderson WG. Induction chemotherapy plus radiation compared with surgery plus radiation in patients with advanced laryngeal cancer. N Engl J Med. 1991;324:1685-1690.
11. Groome PA, O'Sullivan B, Irish JC, Rothwell DM, Schulze K, Warde PR, Schneider KM, Mackenzie RG, Hodson DI, Hammond JA, Gulavita SP, Eapen LJ, Dixon PF, Bissett RJ, Mackillop WJ. Management and outcome differences in supraglottic cancer between Ontario, Canada, and the surveillance, epidemiology, and end results areas of the United States. J Clin Oncol. 2003;21:496-505.
12. Becker M. Larynx and hypopharynx. Radiol Clin North Am. 1998;36:891-920, vi.
13. Oztürkcan S, Katilmiş H, Ozdemir I, Tuna B, Güvenç IA, Dündar R. Occult contralateral nodal metastases in supraglottic laryngeal cancer crossing the midline. Eur Arch Otorhinolaryngol. 2009;266:117-120.
14. Kuno H, Onaya H, Fujii S, Ojiri H, Otani K, Satake M. Primary staging of laryngeal and hypopharyngeal cancer: CT, MR imaging and dual-energy CT. Eur J Radiol. 2014;83:e23-e35.
15. Mongelluzzo GJ, Fourgas EC. Imaging for larynx cancer assessment. Operative Techniques in Otolaryngology. 2024;35:141-148.
16. Becker M, Zbären P, Casselman JW, Kohler R, Dulguerov P, Becker CD. Neoplastic invasion of laryngeal cartilage: reassessment of criteria for diagnosis at MR imaging. Radiology. 2008;249:551-559.
17. Maroldi R, Farina D, Borghesi A, Marconi A, Gatti E. Perineural tumor spread. Neuroimaging Clin N Am. 2008;18:413-429.
18. Quon A, Fischbein NJ, McDougall IR, Le QT, Loo BW Jr, Pinto H, Kaplan MJ. Clinical role of ^{18}F-FDG PET/CT in the management of squamous cell carcinoma of the head and neck and thyroid carcinoma. J Nucl Med. 2007;48 Suppl 1:58S-67S.
19. Fleming AJ Jr, Smith SP Jr, Paul CM, Hall NC, Daly BT, Agrawal A, Schuller DE. Impact of [^{18}F]-2-fluorodeoxyglucose-positron emission tomography/computed tomography on previously untreated head and neck cancer patients. Laryngoscope. 2007;117:1173-1179.
20. Goel R, Moore W, Sumer B, Khan S, Sher D, Subramaniam RM. Clinical practice in PET/CT for the management of head and neck squamous cell cancer. AJR Am J Roentgenol. 2017;209:289-303.
21. Baugnon KL, Beitler JJ. Pitfalls in the staging of cancer of the laryngeal squamous cell carcinoma. Neuroimaging Clin N Am. 2013;23:81-105.
22. Cavaliere C, Romeo V, Aiello M, Mesolella M, Iorio B, Barbuto L, Cantone E, Nicolai E, Covello M. Multiparametric evaluation by simultaneous PET-MRI examination in patients with histologically proven laryngeal cancer. Eur J Radiol. 2017;88:47-55.
23. Hamson EJ, Keane FM, Tholen S, Schilling O, Gorrell MD. Understanding fibroblast activation protein (FAP): substrates, activities, expression and targeting for cancer therapy. Proteomics Clin Appl. 2014;8:454-463.
24. Loktev A, Lindner T, Mier W, Debus J, Altmann A, Jäger D, Giesel F, Kratochwil C, Barthe P, Roumestand C, Haberkorn U. A Tumor-imaging method targeting cancer-associated fibroblasts. J Nucl Med. 2018;59:1423-1429.
25. Kratochwil C, Flechsig P, Lindner T, Abderrahim L, Altmann A, Mier W, Adeberg S, Rathke H, Röhrich M, Winter H, Plinkert PK, Marme F, Lang M, Kauczor HU, Jäger D, Debus J, Haberkorn U, Giesel FL. ^{68}Ga-FAPI PET/CT: tracer uptake in 28 different kinds of cancer. J Nucl Med. 2019;60:801-805.
26. Kobayashi H, Enomoto A, Woods SL, Burt AD, Takahashi M, Worthley DL. Cancer-associated fibroblasts in gastrointestinal cancer. Nat Rev Gastroenterol Hepatol. 2019;16:282-295.
27. Chen H, Pang Y, Wu J, Zhao L, Hao B, Wu J, Wei J, Wu S, Zhao L, Luo Z, Lin X, Xie C, Sun L, Lin Q, Wu H. Comparison of [^{68}Ga]Ga-DOTA-FAPI-04 and [^{18}F] FDG PET/CT for the diagnosis of primary and metastatic lesions in patients with various types of cancer. Eur J Nucl Med Mol Imaging. 2020;47:1820-1832.
28. Giesel FL, Kratochwil C, Lindner T, Marschalek MM, Loktev A, Lehnert W, Debus J, Jäger D, Flechsig P, Altmann A, Mier W, Haberkorn U. ^{68}Ga-FAPI PET/CT: biodistribution and preliminary dosimetry estimate of 2 DOTA-

containing FAP-targeting agents in patients with various cancers. J Nucl Med. 2019;60:386-392.

29. Koerber SA, Staudinger F, Kratochwil C, Adeberg S, Haefner MF, Ungerechts G, Rathke H, Winter E, Lindner T, Syed M, Bhatti IA, Herfarth K, Choyke PL, Jaeger D, Haberkorn U, Debus J, Giesel FL. The role of ^{68}Ga-FAPI PET/CT for patients with malignancies of the lower gastrointestinal tract: first clinical experience. J Nucl Med. 2020;61:1331-1336.
30. Guo W, Pang Y, Yao L, Zhao L, Fan C, Ke J, Guo P, Hao B, Fu H, Xie C, Lin Q, Wu H, Sun L, Chen H. Imaging fibroblast activation protein in liver cancer: a single-center post hoc retrospective analysis to compare [^{68}Ga] Ga-FAPI-04 PET/CT versus MRI and [^{18}F]-FDG PET/CT. Eur J Nucl Med Mol Imaging. 2021;48:1604-1617.
31. Gu B, Xu X, Zhang J, Ou X, Xia Z, Guan Q, Hu S, Yang Z, Song S. The added value of ^{68}Ga-FAPI PET/CT in patients with head and neck cancer of unknown primary with ^{18}F-FDG-negative findings. J Nucl Med. 2022;63:875-881.
32. Bhat RR, Shivalingappa SS, Ashok M, Kesari A, Kedilaya S, L YU. Utilization of gallium-68 fibroblast activation protein inhibitor positron emission tomography (^{68}Ga-FAPI PET) for head and neck malignancies with neck ımaging reporting and data system (Ni-RADS) correlation. Cureus. 2025;17:e78476.

Original Article

Mol Imaging Radionucl Ther 2026;35(2):92-104 **DOI:***10.4274/mirt.galenos.2026.39775*

Validation of Simplified Renal Dosimetry Protocols for ^{177}Lu-DOTATATE Therapy Using the IDAC-dose Software

IDAC-dose Yazılımı Kullanılarak ^{177}Lu-DOTATATE Tedavisi için Düzenlenmiş Basitleştirilmiş Böbrek Dozimetri Protokollerinin Doğrulanması

Anji Yokouchi[1,2], Takayuki Shibutani[2], Takahiro Konishi[1], Hiroto Yoneyama[1], Hajime Ichikawa[3], Hiroshi Wakabayashi[4]

[1]*Kanazawa University Hospital, Department of Radiological Technology, Kanazawa, Japan*
[2]*Kanazawa University, Graduate School of Medical Sciences, Department of Quantum Medical Technology, Division of Health Sciences, Kanazawa, Japan*
[3]*Niigata University of Health and Welfare, Department of Radiological Technology, Niigata, Japan*
[4]*Kanazawa University Hospital, Department of Nuclear Medicine, Kanazawa, Japan*

Abstract

Objectives: The multi-time-point imaging method for renal dosimetry in lutetium-177 (^{177}Lu)-DOTATATE therapy imposes a significant burden. This study aimed to validate simplified two-time-point (2TP) and three-time-point (3TP) protocols using the International Commission on Radiological Protection-compliant IDAC-Dose 2.1 software.

Methods: This retrospective study analyzed 28 kidneys obtained from 17 patients with neuroendocrine neoplasms. Renal absorbed doses from a reference four-time-point (4TP) schedule (4, 24, 72, and 120 hours) were compared with ten simplified protocols using statistical analyses of error and agreement.

Results: Protocols that included the 120-hour time point demonstrated significantly higher accuracy. The 2TP (4, 24) protocol showed a profound underestimation [mean percentage error (MPE): -14.3%] and a high error. In contrast, the 2TP (24, 120) protocol showed excellent agreement [MPE: 0.57%, mean absolute percent error (MAPE): 5.5%]. Among 3TP methods, the 3TP (24, 72, 120) protocol yielded the highest accuracy (MAPE: 1.97%).

Conclusion: Accurate renal dosimetry in ^{177}Lu-DOTATATE therapy can be achieved with simplified protocols. Incorporating a late-phase time point (around 120 hours) is essential for reliable estimation. The 2TP (24, 120) and 3TP (24, 72, 120) combinations are suggested as feasible alternatives to the standard 4TP method.

Keywords: ^{177}Lu-DOTATATE, renal dosimetry, peptide receptor radionuclide therapy, neuroendocrine neoplasms, simplified dosimetry

Öz

Amaç: Lutetyum-177 (^{177}Lu)-DOTATATE tedavisinde böbrek dozimetresi için çok zamanlı görüntüleme yöntemi önemli bir yük oluşturur. Bu çalışma, Uluslararası Radyolojik Koruma Komitesi'ne uygun IDAC-Dose 2.1 yazılımını kullanarak basitleştirilmiş iki zamanlı (2TP) ve üç zamanlı (3TP) protokollerinin doğruluğunu doğrulamayı amaçlamıştır.

Address for Correspondence: Takayuki Shibutani, Kanazawa University, Graduate School of Medical Sciences, Department of Quantum Medical Technology, Division of Health Sciences, Kanazawa, Japan
E-mail: iwsb03100621@staff.kanazawa-u.ac.jp **ORCID ID:** orcid.org/0000-0002-4718-7947
Received: 10.01.2026 **Accepted:** 21.04.2026 **Publication Date:** 04.06.2026

Cite this article as: Yokouchi A, Shibutani T, Konishi T, Yoneyama H, Ichikawa H, Wakabayashi H. Validation of simplified renal dosimetry protocols for ^{177}Lu-DOTATATE therapy using the IDAC-dose software. Mol Imaging Radionucl Ther. 2026;35(2):92-104.

Yöntem: Bu retrospektif çalışma, 17 hastadan alınan 28 böbreği analiz etmiştir. Bir referans dört zamanlı (4TP) takviminden (4, 24, 72 ve 120 saat) böbrek emilen dozlar, hata ve uyum istatistiksel analizleriyle on basitleştirilmiş protokolle karşılaştırılmıştır.

Bulgular: Yüz yirmi saatlik zaman dilimini içeren protokoller, anlamlı şekilde daha yüksek doğruluk göstermiştir. 2TP (4, 24) protokolü, derin bir düşük tahmin [ortalama yüzde hatası (MPE): %-14,3] ve yüksek hata göstermiştir. Buna karşılık, 2TP (24, 120) protokolü mükemmel bir uyum göstermiştir [MPE: %0,57, ortalama mutlak yüzde hatası (MAPE): %5,5]. 3TP yöntemleri arasında, 3TP (24, 72, 120) protokolü en yüksek doğruluğu elde etmiştir (MAPE: %1,97%).

Sonuç: ^{177}Lu-DOTATATE tedavisinde doğru böbrek dozimetresi, basitleştirilmiş protokollerle elde edilebilir. Geç evre bir zaman noktasının (yaklaşık 120 saat) dahil edilmesi, güvenilir bir tahmin için önemlidir. 2TP (24, 120) ve 3TP (24, 72, 120) kombinasyonları, standart 4TP yöntemine alternatif olarak uygun seçenekler olarak önerilmektedir.

Anahtar Kelimeler: ^{177}Lu-DOTATATE, böbrek dozimetresi, peptit reseptör radyonüklid tedavisi, nöroendokrin neoplaziler, basitleştirilmiş dozimetri

Introduction

Peptide receptor radionuclide therapy (PRRT) is a therapeutic approach that selectively delivers radiation to target organs in patients with somatostatin receptor-positive neuroendocrine neoplasms (NENs). The radiopharmaceutical lutetium-177 (^{177}Lu)-DOTATATE, representative of those used in PRRT, has been reported to significantly improve progression-free survival and overall survival (1,2). In PRRT, achieving high absorbed doses to tumors while minimizing radiation to normal organs such as the kidneys and bone marrow is essential (3,4,5,6,7). This principle is underscored in established international treatment guidelines (8). The kidneys are particularly radiosensitive, and a renal absorbed dose threshold of 23 Gy originally derived from external beam radiotherapy, is widely applied in clinical practice to avoid the risk of nephropathy (9). Renal absorbed dose estimates have directly influenced treatment modifications, as demonstrated in one cohort where 8 of 13 patients (62%) have discontinued the PRRT before completing the planned four cycles due to exceeding projected kidney tolerance doses (10). Furthermore, long-term follow-up studies have shown that renal dysfunction can appear several years after therapy, highlighting the importance of early dose assessment and individualized treatment planning (4). The established standard for individualized dosimetry is the multi-time-point (MTP) imaging method. This method involves generating a time-activity curve (TAC) from single photon emission computed tomography/computed tomography (SPECT/CT) images acquired at multiple time points over several days to accurately calculate the absorbed dose (11). However, this approach imposes a substantial burden on both patients and medical staff because it requires multiple days of outpatient care and prolonged SPECT acquisition. Indeed, a recent consensus statement from the Society of Nuclear Medicine and Molecular Imaging has highlighted the critical importance of personalized dosimetry in PRRT, while simultaneously acknowledging the logistical necessity of developing practical, simplified imaging schedules (12). Consequently, single-time-point (STP) methods applicable to PRRT have been proposed (13,14), and the accuracy of these methods has been evaluated in numerous studies (15,16,17). On the other hand, STP methods have also been reported to be less stable in terms of accuracy and reproducibility compared with MTP methods (18,19). The acquisition timing for renal dose assessment using SPECT is commonly based on a three-time-point (3TP) protocol, with imaging completed within 72 hours post-injection (15,16); however, this schedule may mischaracterize the critical terminal clearance phase of ^{177}Lu-DOTATATE from the kidneys. Specifically, omitting direct measurement at later time points necessitates extrapolation of the tail of the TAC, which can introduce substantial errors in the calculated time-integrated activity and, consequently, the final absorbed dose estimate. This is particularly relevant because approximately 70% of renal time-integrated activity occurs after 24 hours (20). To establish robust and reliable dosimetry, international guidelines, such as those from the European Association of Nuclear Medicine/Medical Internal Radionuclide Dose (MIRD) Committee, recommend a comprehensive imaging schedule. For radiopharmaceuticals with pharmacokinetics similar to ^{177}Lu-DOTATATE, this typically involves three to five acquisitions over a period of up to seven days to accurately characterize the TAC, including both uptake and washout phases. Therefore, a four-time-point (4TP) protocol spanning this period is widely considered the reference standard for validating simplified methods (21).

In recent years, numerous studies have investigated reduced time-point strategies, such as two-time-point (2TP) and 3TP protocols, to alleviate the clinical burden associated with MTP dosimetry. These studies have successfully demonstrated that simplified schedules can provide reliable dose estimates (10,15,22). However, these crucial validations have predominantly been performed using software based on the traditional MIRD formalism (e.g., OLINDA/EXM), which utilizes older, stylized anatomical phantoms (23).

The field of dosimetry is transitioning to a more modern, standardized framework proposed by the International Commission on Radiological Protection (ICRP). This transition represents a substantial shift from previous MIRD-based approaches, as the ICRP framework employs a new generation of anatomically realistic adult and pediatric reference phantoms alongside updated, nuclide-specific S-values. This modern framework is implemented in IDAC-Dose 2.1, an open-source, freely accessible software platform (24). The advantage over commercial and original software programs is accessibility, which is designed to promote a harmonized, internationally standardized approach to dosimetry. Removing software cost barriers and using a common ICRP-based calculation engine have the potential to unify dosimetry practices across institutions worldwide. However, to our knowledge, the performance and reliability of simplified dosimetry protocols have not yet been extensively evaluated using an ICRP-compliant platform. This validation provides additional evidence for moving the field towards genuine international standardization.

The aim of this study was to systematically evaluate, against a robust 4TP reference standard, various 2TP and 3TP combinations for renal dosimetry in ^{177}Lu-DOTATATE therapy using the ICRP-compliant, open-source software IDAC-Dose.

Materials and Methods

Patients and Treatment Protocol

PRRT in this study was performed using ^{177}Lu-DOTATATE, with a typical administered activity of 7.4 GBq per cycle. The mean administered activity was 7.47±0.17 GBq for 15 patients, while two patients received reduced doses of 5.8 GBq and 3.8 GBq, respectively. Antiemetics, including serotonin receptor antagonists, were administered prophylactically to mitigate radiation-induced nausea and vomiting. Subsequently, an amino acid solution (LysaKare, Novartis Pharma K.K, Tokyo, Japan) was administered to competitively inhibit reabsorption of the radiopharmaceutical in the renal proximal tubules, thereby reducing the renal radiation dose. ^{177}Lu-DOTATATE was administered intravenously after the LysaKare infusion.

The study Ethics Committee of Kanazawa University School of Medicine was approved by the institutional review board (approval no: 114507-1, date: 13.03.2024), and the requirement for written informed consent was waived. Clinical data were collected from 17 NEN patients who underwent four SPECT/CT scans during their first cycle of PRRT at our institution. A total of 33 kidneys were evaluated: 32 were obtained from 16 patients with bilateral kidneys, and 1 was obtained from a patient with a single kidney. However, 5 kidneys were excluded from the analysis due to severe difficulties in accurately delineating the volume of interest (VOI) and subsequently generating TACs. The specific reasons included: massive spill-in from intense physiological liver uptake compressing the right kidney, with an unclear boundary (n=1); massive spill-in from a liver tumor to the right kidney (n=1); splenic contact causing left kidney deformation and massive spill-in, complicated by a renal cyst (n=1); a right renal tumor obscuring the organ boundary (n=1); and a giant right renal tumor combined with intense liver uptake (n=1). Furthermore, because of the curve-fitting characteristics of IDAC-Dose, fluctuating activity plots caused by such spill-in or poorly defined boundaries result in variable and unreliable calculations of the time-integrated activity coefficient (TIAC). Therefore, these kidneys were excluded to ensure overall dosimetric accuracy. Consequently, twenty-eight kidneys (6 of 17 patients had only a single evaluable kidney) were included in the final analysis. Because a substantial proportion of evaluations involved a single kidney, individual kidneys were analyzed as independent samples in the statistical analysis. The baseline characteristics of the patients were as follows: the mean age was 61 years (range, 34-82 years); there were 10 male and 7 female patients. According to the World Health Organization classification (25), tumor grades were G1 in one patient, G2 in eleven patients, G3 in two patients, and unknown in three patients. The baseline estimated glomerular filtration rate was 70.8±21.8 mL/min (range: 28.4-108.0 mL/min). Diabetes mellitus and hypertension were each present in seven patients.

SPECT/CT Imaging and Image Reconstruction

SPECT/CT imaging was performed at four time points: approximately 4-, 24-, 72-, and 120-hours post-administration of ^{177}Lu-DOTATATE. The equipment used was either a Symbia Intevo 16 or a Symbia Intevo Bold (Siemens Healthineers, Erlangen, Germany), each fitted with a medium-energy, low-penetration collimator. The acquisition parameters were a matrix size of 128, a pixel size of 4.8 mm, a zoom of 1.0, and 60 views. The time per view was 10 seconds for early post-administration scans and was appropriately extended, up to a maximum of 40 seconds, for later time points as counts decreased. The energy peak was set at 208 keV with a 20% main energy window. For the triple energy window (TEW) method, two adjacent 10% scatter windows (lower and upper) were also set.

Image reconstruction was performed using xSPECT Quant (Siemens Healthineers, Erlangen, Germany) (26), employing an algorithm based on the ordered subsets

conjugate gradient minimization method. Reconstruction parameters were set as follows: iterations: 24-60; subsets: 1; Gaussian filter full width at half maximum: 16 mm. Corrections for attenuation and scatter were applied using CT-based attenuation correction and the TEW method, respectively.

Imaging Point Combinations

The various imaging point combinations evaluated in this study are illustrated in Figure 1. A total of ten simplified protocols were assessed against the 4TP reference standard: six 2TP combinations and four 3TP combinations.

TAC Generation and Absorbed Dose Calculation

Kidney VOIs was defined on the CT images of the SPECT/CT datasets. To strictly account for potential organ motion, deformation, and positional shifts between scans, VOIs were manually delineated at each imaging time point (4, 24, 72, and 120 hours), rather than propagating a single VOI from the baseline scan. Using the co-registered CT images (3-mm slice thickness) as an anatomical reference, the VOIs were drawn slice-by-slice to encompass the entire renal parenchyma while excluding the renal pelvis and cysts. To ensure consistency and minimize intra-operator variability, all delineations were performed by a single experienced operator. From these time-point-specific VOIs, activity concentration values were extracted for each time point and decay-corrected to generate a TAC. To calculate the TIAC, the TAC data was input into the integrated curve-fitting module of IDAC-Dose 2.1 (Lund University, Sweden), a publicly available internal dosimetry program (24). To formally assess intra-observer variability, a repeatability analysis was conducted. A subset of 10 kidneys, selected via computer-generated random sampling, was re-segmented at all four time points by the same operator after an interval of more than one year to eliminate recall bias. The intraclass correlation coefficient (ICC) was calculated to assess the reliability of the quantified renal radioactivity, which is the most critical determinant of dosimetric accuracy. To generate TACs and subsequently calculate TIACs, we used the software's internal compartmental system. A standard "1 uptake, 2 retention" phase model was selected to fit the data points accurately and extrapolate the terminal clearance.

The final renal absorbed dose was calculated using the IDAC-Dose software (version 2.1) based on the methods and reference phantoms described by the ICRP (27). The software settings were specifically configured for the ^{177}Lu isotope. To ensure anatomically accurate dosimetry, the ICRP Publication 110 adult male or adult female reference voxel phantom was selected according to each patient's sex. The resulting TIAC was used by the software to calculate the absorbed dose by multiplying it by the ICRP Publication 133-compliant S-values for ^{177}Lu and the administered activity for the kidneys based on the adult model described in ICRP Publication 133.

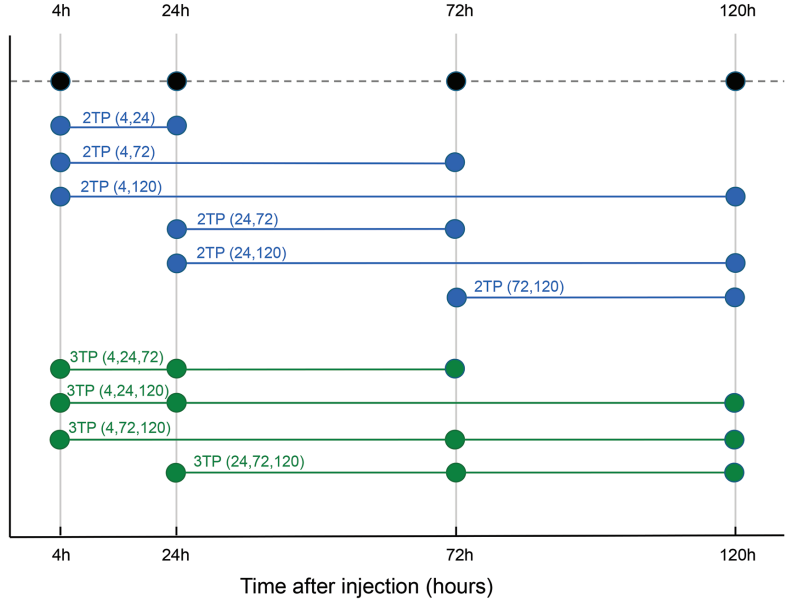

Figure 1. Schematic of the evaluated dosimetry protocols, comparing the reference 4TP schedule with six 2TP and four 3TP combinations
4TP: Four-time-point, 2TP: Two-time-point, 3TP: Three-time-point

Statistical Analysis

The accuracy of the 2TP and 3TP methods was evaluated by comparing their estimated renal absorbed doses with the reference values calculated using the 4TP method (imaging at 4, 24, 72, and 120 hours). In addition to identifying the optimal combination for each reduced-time-point method, we compared the accuracy across methods with varying numbers of imaging points. Specifically, by comparing the results of the most accurate 2TP combination with those of the least accurate 3TP combination, we assessed the importance of selecting appropriate imaging time points rather than simply increasing the number of imaging points for the accuracy of renal absorbed dose estimation. The accuracy of absorbed dose estimation for each combination of imaging points was assessed using the mean percent error (MPE), the mean absolute percent error (MAPE), and the root mean square error (RMSE). These metrics were calculated using the following equations:

Where pred is the absorbed dose calculated by each reduced-time-point method such as 2TP and 3TP methods, ref is the reference value from the 4TP method, and N is the total number of kidneys evaluated.

Additionally, Bland-Altman analysis was performed to assess agreement between each reduced-time-point method and the 4TP method by calculating the mean difference (fixed bias) with its 95% confidence interval (CI) and the limits of agreement (LoA), thereby statistically evaluating differences between the protocols. Furthermore, to formally test the differences in absolute absorbed doses among the protocols, a non-parametric Friedman test was conducted because the data consisted of repeated measurements on the same kidneys. Because the Friedman test indicated a significant overall difference, pairwise comparisons between the reference 4TP protocol and the simplified protocols were performed using the Wilcoxon signed-rank test with Holm's adjustment. An adjusted p-value of <0.05 was considered statistically significant. An acceptable accuracy threshold was predefined for the objective evaluation of the clinical viability of the simplified methods. In clinical internal dosimetry, absolute absorbed dose calculations inherently encompass various sources of methodological uncertainties, including camera calibration, image segmentation, and partial volume effects, which are generally estimated at 10% to 20% even with MTP imaging (21). Given this inherent noise floor, a predefined MAPE threshold of <10% was established as a conservative criterion for acceptable clinical equivalence. This threshold ensures that the simplification does not substantially degrade dosimetric reliability and is consistent with the optimal MAPE values reported in recent simplified PRRT dosimetry studies (22).

Results

The mean renal volume for the 28 kidneys included in the analysis was 163.2±42.4 cm³ (range: 101-279 cm³). The mean reference absorbed dose, calculated using the 4TP method, was 3222.5±1173.4 mGy (range: 1490-6040 mGy). The repeatability analysis of a randomly sampled subset of 10 kidneys demonstrated excellent intra-observer reliability for quantification of radioactivity, yielding an ICC of 0.998 (95% CI: 0.996 to 0.999). A summary of the absolute absorbed dose estimations [mean, standard deviation (SD), and range] for the reference (4TP) protocol and all ten simplified (2TP and 3TP) protocols is presented in Table 1.

Table 1. Renal volumes and absolute absorbed dose estimations for the 4TP reference and simplified 2TP and 3TP protocols

Parameter	Mean ± SD	Range (min-max)
Renal volume (cm³)	163.2±42.4	101-279
Absorbed dose (mGy)		
Reference (4TP)	3162.5±1090.3	1490-5690
2TP (4, 24)	2713.0±1313.1	955-5910
2TP (4, 72)	3309.6±1269.8	1290-6590
2TP (4, 120)	3196.4±988.6	1620-5610
2TP (24, 72)	3335.0±1274.5	1280-6400
2TP (24, 120)	3156.8±1040.2	1620-5630
2TP (72, 120)	3292.1±1203.9	1710-5790
3TP (4, 24, 72)	3219.6±1256.4	1260-6290
3TP (4, 24, 120)	3146.8±1071.1	1610-5510
3TP (4, 72, 120)	3205.4±1057.1	1490-5590
3TP (24, 72, 120)	3204.3±1118.9	1500-5820

SD: Standard deviation, 4TP: Four-time-point, 2TP: Two-time-point, 3TP: Three-time-point

Evaluation by 2TP Method

To formally evaluate the absolute absorbed doses, a Friedman test was performed. For the 2TP methods, a statistically significant overall difference was observed among the protocols (p=0.0047). However, the post hoc pairwise comparison with Holm's adjustment demonstrated no significant difference between the reference 4TP and the recommended 2TP (24, 120) protocols (adjusted p=1.000) (Figure 2).

As detailed in Figures 3 and 4, the 2TP (4, 24) protocol, which omits late-phase imaging, performed the worst across all error metrics. It exhibited a large negative bias (MPE: -14.3±30.5%) alongside the highest MAPE (29.6%) and RMSE (1271.9 mGy). Its MPE distribution was skewed towards negative values with a wide interquartile range. In stark contrast, protocols incorporating the 120-hour time point demonstrated significantly improved accuracy. Specifically, the 2TP (24, 120) combination yielded the highest precision, displaying the smallest MPE (0.57±5.8%) and a remarkably low MAPE (5.5%). Both 2TP (24, 120) and 2TP (4, 120) maintained MAPE values well below our predefined 10% clinical threshold and RMSE values below 400 mGy.

The Bland-Altman analysis of the 2TP methods is shown in Figure 5. The 2TP (4, 24) protocol showed a large, statistically significant negative fixed bias (mean difference: -603.2 mGy, 95% CI: -991.2 to -273.1 mGy) and wide LoA. For these two protocols, 2TP (4, 120) and 2TP (24, 120), the 95% CIs for the mean difference included zero (95% CI: -33.4 to 125.9 mGy and -161.2 to 44.6 mGy, respectively), indicating no statistically significant systematic bias. The 95% CIs for the other 2TP protocols were: 2TP (4, 72) (-5.4 to 227.8 mGy), 2TP (24, 72) (59.7 to 354.6 mGy), and 2TP (72, 120) (19.1 to 234.4 mGy) (Figure 5).

Evaluation by 3TP Method

For the 3TP methods, the Friedman test also revealed a significant overall difference in absolute absorbed doses (p=0.019) (Figure 6). The post-hoc analysis indicated that the high-precision 3TP (24, 72, 120) protocol showed a statistically significant difference compared with the 4TP reference (adjusted p=0.0057), whereas the 3TP (4, 24, 72) and 3TP (4, 24, 120) protocols did not show significant differences (adjusted p=1.000 for both).

The MPE, MAPE, and RMSE for the 3TP combinations are summarized in Figures 7 and 8. While all 3TP methods demonstrated clinically acceptable error margins based on our predefined threshold (MAPE ≤10%), the 3TP combination (24, 72, 120) outperformed the other combinations. It achieved the smallest bias (MPE: 1.24±2.2%) with the narrowest interquartile range, the lowest MAPE (1.97%), and an exceptionally low RMSE (58.1 mGy).

The Bland-Altman analysis of the 3TP methods is shown in Figure 9. The 3TP (4, 24, 72) protocol, which omits imaging beyond 72 hours, exhibited a large SD of differences (340.3 mGy) and wide LoA, ranging from -632.7 to 701.2 mGy.

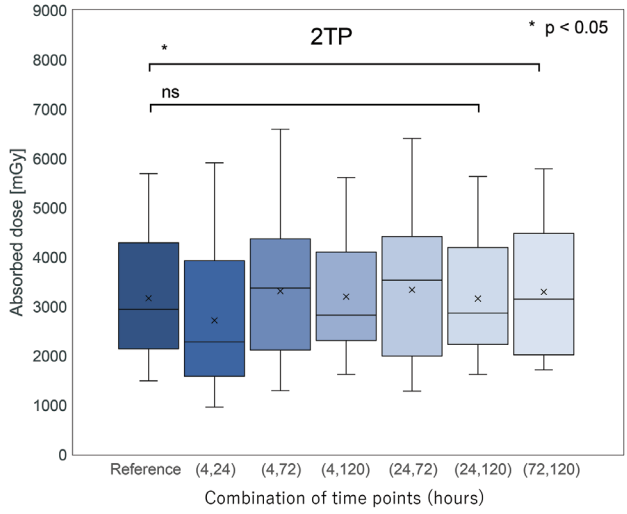

Figure 2. Absolute renal absorbed doses for the reference 4TP and simplified 2TP protocols. Boxes show the interquartile range, the median (line), and the mean ("x"); whiskers indicate the minimum and maximum values. *adjusted p<0.05 vs. 4TP (Friedman test followed by Wilcoxon signed-rank test with Holm's adjustment); not significant
4TP: Four-time-point, 2TP: Two-time-point

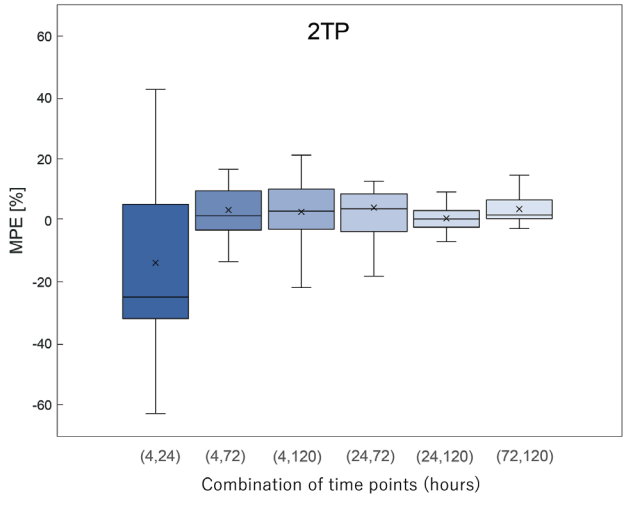

Figure 3. Mean percent error of each 2TP protocol relative to the 4TP reference. Box plot elements as in Figure 2
4TP: Four-time-point, 2TP: Two-time-point

In contrast, replacing the 72-hour time point with the 120-hour time point in the 3TP (4, 24, 120) protocol reduced the SD of the differences to 189.3 mGy. The smallest SDs of the differences were observed for 3TP (4, 72, 120) and 3TP (24, 72, 120), with values of 63.6 mGy and 78.0 mGy, respectively; these yielded the narrowest LoAs. For these two high-precision protocols, the 95% CIs for the mean differences did not include zero. The 95% CIs for the mean differences in the 3TP combinations were as follows: 3TP (4, 24, 72) (-81.9 to 132.9 mGy), 3TP (4, 24, 120) (-75.8 to 43.7 mGy), 3TP (4, 72, 120) (21.6 to 61.8 mGy), and 3TP (24, 72, 120) (19.8 to 68.9 mGy) (Figure 9).

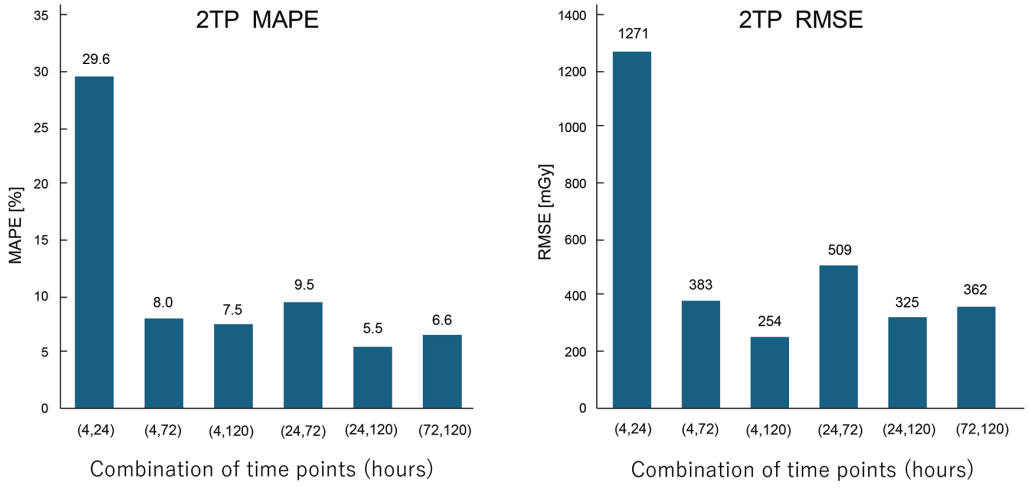

Figure 4. MAPE and RMSE for each 2TP protocol
MAPE: Mean absolute percent error, RMSE: Root mean square error, 2TP: Two-time-point

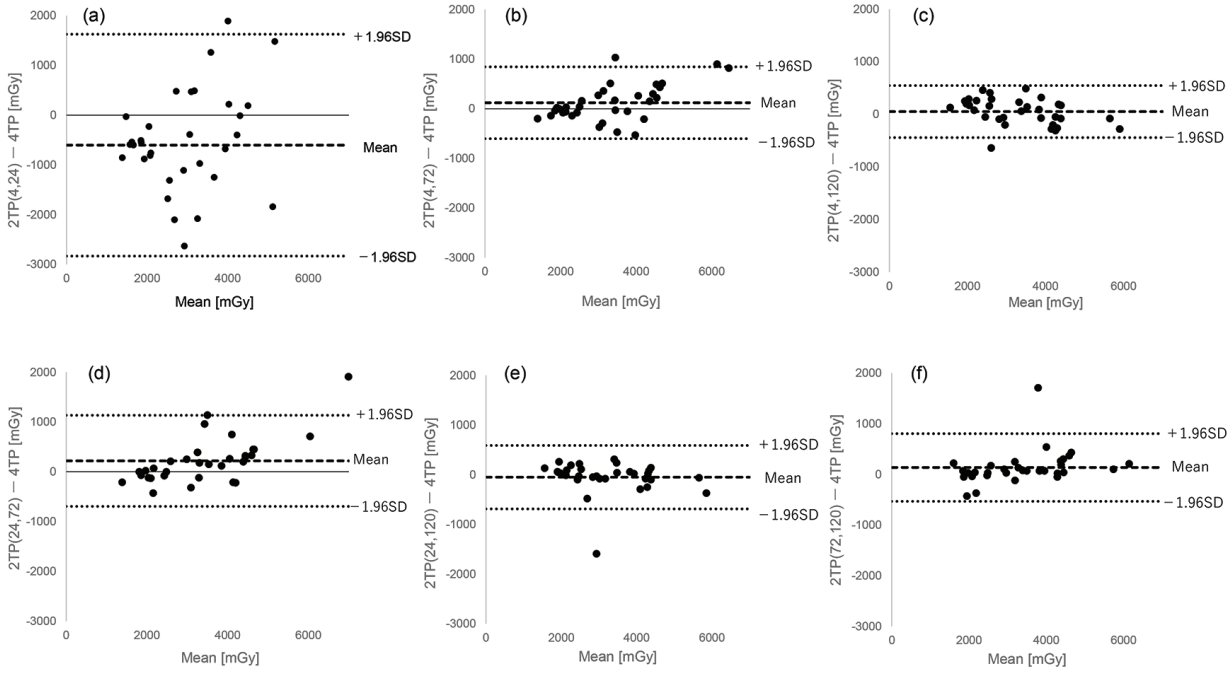

Figure 5. Bland-Altman plots comparing absorbed doses from 2TP protocols with the 4TP reference. Solid lines indicate the mean difference (bias); dashed lines indicate the 95% limits of agreement
4TP: Four-time-point, 2TP: Two-time-point, SD: Standard deviation

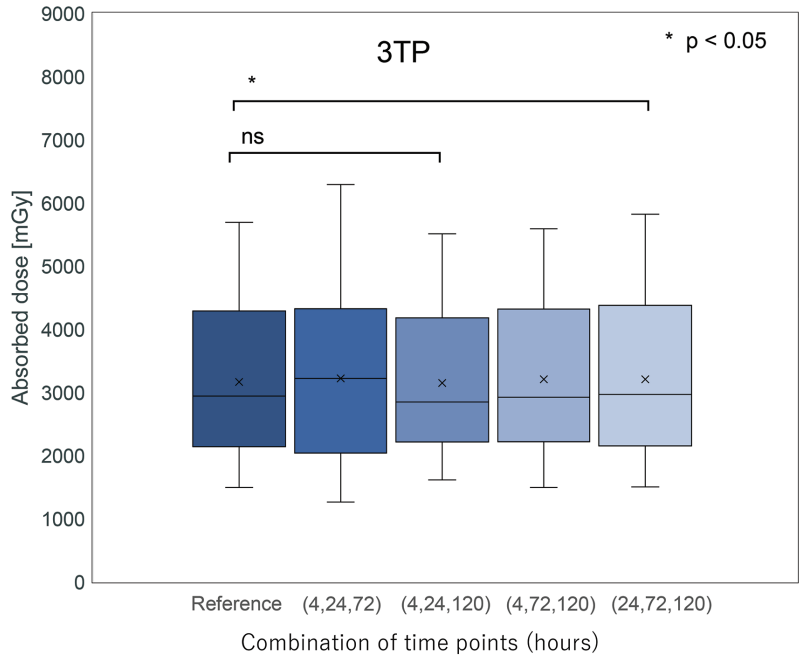

Figure 6. Absolute renal absorbed doses for the 4TP and simplified 3TP protocols. Box plot elements and statistical tests as in Figure 2. *adjusted p<0.05, **adjusted p<0.01 vs. 4TP; not significant
3TP: Three-time-point, 4TP: Four-time-point

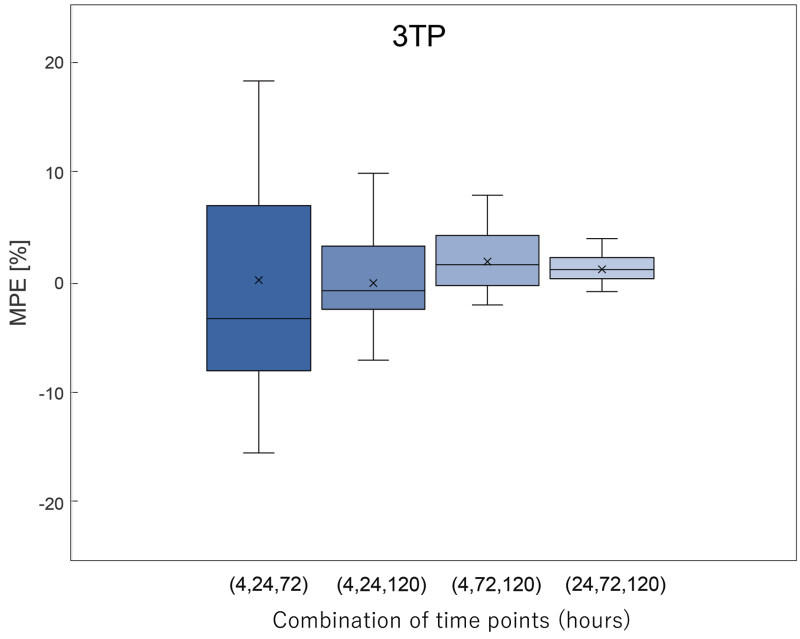

Figure 7. MPE of each 3TP protocol relative to the 4TP reference. Box plot elements as in Figure 2
MPE: Mean percent error, 3TP: Three-time-point, 4TP: Four-time-point

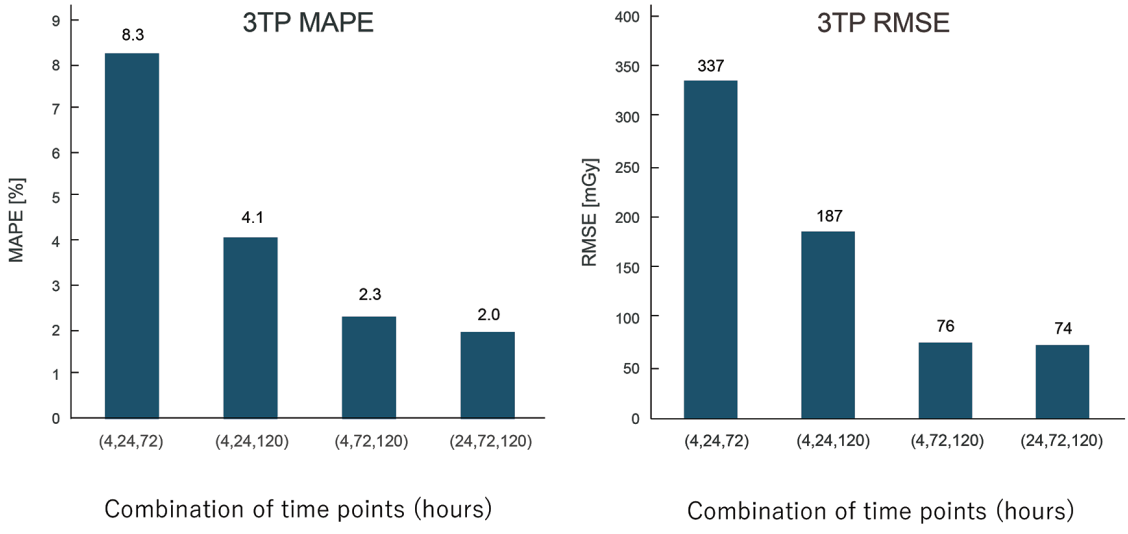

Figure 8. MAPE and RMSE for each 3TP protocol
MAPE: Mean absolute percent error, 3TP: Three-time-point, RMSE: Root mean square error

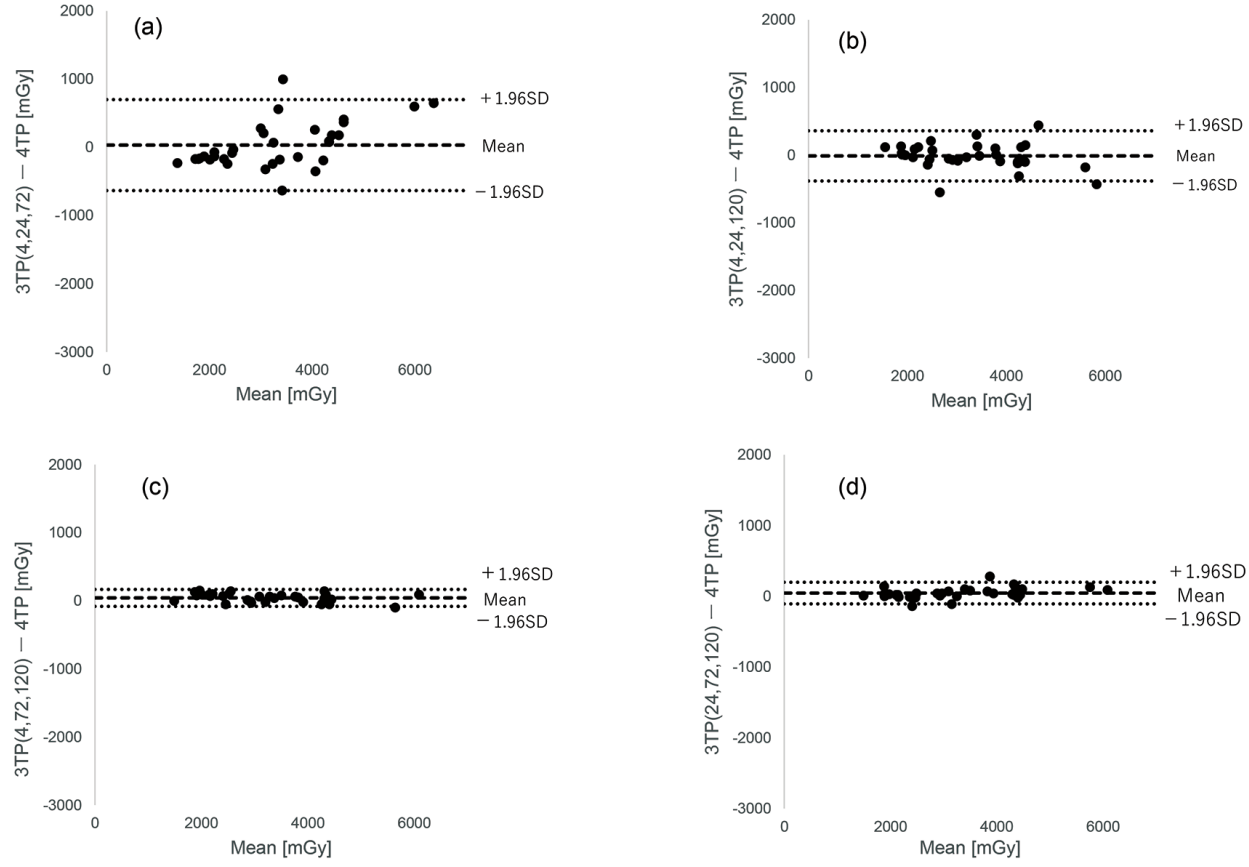

Figure 9. Bland-Altman plots comparing absorbed doses from 3TP protocols with the 4TP reference. Lines are defined as in Figure 5
3TP: Three-time-point, 4TP: Four-time-point, SD: Standard deviation

Discussion

The optimization of ^{177}Lu-DOTATATE therapy depends on patient-specific dosimetry to balance tumor control against toxicity to organs such as the kidneys and bone marrow. Conventional MTP protocols are accurate but clinically burdensome, motivating research into simplified approaches. The primary determinant of accuracy is not the number of acquisitions but the choice of imaging times (22,28,29,30).

This study shows that accurate renal dosimetry can be achieved with simplified protocols if they include a late-phase acquisition. Our results highlight the necessity of an imaging point around 120 hours post-injection to capture terminal renal clearance. For example, the 2TP (4, 24) protocol substantially underestimated the dose (RMSE: 1271 mGy) because it relied solely on early distribution data, thereby overestimating washout and underestimating the absorbed dose. In contrast, protocols incorporating a late point—2TP (24, 120) and 2TP (4, 120)— successfully met our predefined acceptable threshold of MAPE <10% (RMSE: 325 mGy and 254 mGy). The combination of a 24-hour baseline and a 120-hour terminal point enabled robust estimation of the effective half-life using the selected compartmental model. Notably, the 2TP (24, 120) protocol outperformed the 3TP (4, 24, 72) (RMSE: 325 mGy vs. 337 mGy), underscoring that late data are more valuable than additional early points. Since ~70% of renal time-integrated activity occurs after 24 hours (29), omission of late acquisitions critically undermines reliability.

The Bland-Altman analysis provided further critical insights beyond average error metrics. It confirmed that the poor performance of protocols lacking late data, such as 2TP (4, 24), was not due to random error but to a significant systematic bias that consistently underestimated the absorbed dose. Similarly, the 3TP (4, 24, 72) protocol, despite a modest mean error, exhibited wide LoA, indicating poor precision and making it unreliable for individual patient dosimetry. In stark contrast, the 2TP (24, 120) protocol showed no significant systematic bias and had narrow LoA, demonstrating good agreement with the 4TP reference standard in this cohort. The high-precision 3TP protocols further narrowed these limits, confirming their robustness for providing reliable, patient-specific dose estimates.

The statistical testing of the 3TP methods highlighted an important distinction between statistical significance and clinical relevance. The 3TP (24, 72, 120) protocol, despite yielding the lowest error metrics (MAPE of 1.97% and RMSE of 58.1 mGy), demonstrated a statistically significant difference from the reference standard (adjusted p=0.0057) with a narrow 95% CI (19.8 to 68.9 mGy) that did not cross zero. This statistical significance is observed because the protocol is exceptionally precise; the systematic bias is so consistently small across all kidneys that it is detected by the paired test. However, considering our predefined clinically acceptable threshold of <10% MAPE, this minimal absolute difference (~50 mGy on average) is negligible in the context of clinical dosimetry. Therefore, the 3TP (24, 72, 120) method remains a highly robust and clinically reliable alternative despite minor statistical variation.

From practical and logistical perspectives, the 2TP (24, 120) schedule is highly feasible and patient-centered. The 24-hour acquisition conveniently aligns with the typical time of hospital discharge following the administration of the radiopharmaceutical. The 120-hour acquisition requires only a single outpatient follow-up visit a few days later. Compared with the standard 4TP schedule, eliminating two intermediate SPECT/CT sessions significantly reduces the physical, logistical, and financial burdens for patients. Simultaneously, it frees valuable gamma camera time and reduces workload for clinical staff. Furthermore, while our study validated the 120-hour point, this specific timing may not be a strict, universal optimum for every institution. Depending on specific facility workflows and scheduling constraints—such as avoiding weekend imaging—other late-phase acquisitions (e.g., 144- or 168-hours post-injection), when combined with the 24-hour baseline, may offer similar dosimetric utility. These alternative late-point combinations represent viable and flexible options that should be explored in future studies to further accommodate diverse institutional needs.

Our focus on simplifying the imaging schedule aligns with the contemporary trend toward favoring routine clinical use of PRRT dosimetry. For example, a recent study by Pirozzi Palmese et al. (31) demonstrated that simplified longitudinal protocols—specifically, performing dosimetry only at the first and fourth cycles—provide cumulative absorbed dose estimates in excellent agreement with full four-cycle dosimetry, thereby significantly improving the cost-benefit ratio. While their work successfully optimized the number of evaluated treatment cycles, our study complements this effort by optimizing the number of imaging time points per cycle. Together, such streamlined strategies offer an optimal balance between clinical feasibility and quantitative accuracy, reducing the burden on both patients and hospital resources.

Validating simplified renal dosimetry protocols within the modern ICRP-based framework represents a primary focus of this work and provides additional evidence to the field. IDAC-Dose 2.1 (24) incorporates the ICRP Publication

110 adult reference voxel phantoms, thereby enabling anatomically accurate dose assessment from real patient CT data. This approach provides a distinct advantage over legacy MIRD-based systems, such as OLINDA/EXM version 1.0 (10, 15, 22), which were based on stylized mathematical phantoms defined by analytical equations and possessed inherent limitations in representing realistic human anatomy.

Software accessibility is a critical factor for broad clinical implementation and multi-center standardization. IDAC-Dose eliminates economic and administrative hurdles as an open-source and freely available platform (24). Commercial platforms such as OLINDA/EXM often impose significant financial and licensing barriers to initial implementation and subsequent upgrades, potentially hindering the widespread adoption and inter-institutional harmonization of dosimetry protocols.

Dosimetric results obtained using IDAC-Dose 2.1 for the adult cohort in this study are methodologically equivalent to those of the latest version. The primary advancement of the recently released IDAC-Dose 2.2 is the inclusion of pediatric reference phantoms. The computational methodology for adult phantoms remains consistent between versions 2.1 and 2.2, ensuring the continued validity of the findings presented here. Software choice is known to affect dose estimates due to differences in phantoms, S-values, and curve fitting (32,33,34). A key question was whether principles derived from MIRD-based systems remain valid in an ICRP-compliant setting. Our results confirm that the fundamental requirement for late acquisition also holds for IDAC-Dose. This reflects the sensitivity of its compartmental fitting model to accurate characterization of the terminal clearance phase (19).

The dosimetry accuracy depends on the entire workflow, including imaging, reconstruction, VOI delineation, and dose calculation (29,35). This study should therefore be considered a pilot study establishing proof of concept. Nonetheless, by demonstrating a simplified, efficient, and accurate protocol within an ICRP-compliant framework, our work provides the foundation for large, multicenter studies needed to establish standardized protocols and to promote broader clinical adoption of individualized dosimetry in PRRT.

Study Limitations

This study has several limitations. First, VOIs were delineated manually at each time point. While this approach ensures anatomical precision for each specific scan, it is labor-intensive and may introduce operator-dependent variability compared to automated segmentation methods. Although our intra-observer repeatability analysis, performed by a single experienced operator, demonstrated excellent consistency in radioactivity quantification (ICC =0.998), the absence of an inter-observer variability assessment remains a limitation. Furthermore, our findings are based on a uniform workflow using a single scanner type, specific reconstruction algorithms, and a standard amino acid protocol. Because variations in these technical factors can influence absolute dosimetric quantification, future multicenter studies evaluating diverse clinical setups are necessary to fully establish the generalizability of these simplified methods. Second, this study should be considered a proof-of-concept pilot, and larger cohorts are needed for further validation. Third, we acknowledge a unit-of-analysis limitation regarding statistical independence. Because 6 patients had only one evaluable kidney, we treated each kidney as independent samples to maximize the use of available data. However, for patients with bilateral evaluations, the pharmacokinetics in the two kidneys of the same individual are likely to be correlated. A more robust statistical approach in larger future studies would be to apply a mixed-effects model treating patients as random effects.

Finally, because this was a retrospective pilot study establishing proof-of-concept for the IDAC-Dose 2.1 framework, a formal a priori sample-size calculation was not performed. The cohort size was determined by the available clinical data that met our strict inclusion and segmentation criteria during the study period. We acknowledge this lack of a formal justification of power as a limitation. Nevertheless, the quantitative data, variances, and effect sizes generated in this study will serve as an essential and reliable foundation for accurate power calculations in future, larger-scale prospective multicenter trials designed to standardize these simplified protocols.

Conclusion

This study demonstrates that accurate renal dosimetry in ^{177}Lu-DOTATATE therapy can be achieved with simplified protocols. Incorporating a late-phase time point (specifically the 120-hour time point used in our study) is essential to improve the accuracy of bi-exponential curve fitting and to reduce dose-estimation errors. Our findings, which, to our knowledge, are among the first to be evaluated in an ICRP-compliant framework, identify the 2-time-point (24, 120 h) and 3-time-point (24, 72, 120 h) combinations as robust and practical alternatives. Adopting these pharmacokinetic-driven schedules provides a clear pathway for reducing patient and institutional burdens while maintaining high-quality, personalized dosimetry for PRRT.

Ethics

Ethics Committee Approval: The study Ethics Committee of Kanazawa University School of Medicine was approved by the institutional review board (approval no: 114507-1, date: 13.03.2024).

Informed Consent: This is retrospective study.

Acknowledgments

We wish to express our sincere gratitude to all the physicians, radiological technologists, and medical physicists in the Department of Nuclear Medicine at the hospital for their invaluable support in patient care and data acquisition for this study. We also thank th e developers at Lund University for making the IDAC-Dose 2.1 software publicly available.

Footnotes

Authorship Contributions

Surgical and Medical Practices: A.Y., T.K., H.Y., H.W., Concept: A.Y., T.S., T.K., H.W., Design: A.Y., T.S., T.K., H.I., Data Collection or Processing: A.Y., Analysis or Interpretation: A.Y., T.S., T.K., H.Y., H.I., H.W., Literature Search: A.Y., T.S., T.K., Writing: A.Y.

Conflict of Interest: No conflict of interest was declared by the authors.

Financial Disclosure: The authors declared that this study has received no financial support.

Availability of Data

The datasets generated and/or analyzed during the current study are available from the corresponding author on reasonable request.

Refereneces

1. Strosberg J, El-Haddad G, Wolin E, Hendifar A, Yao J, Chasen B, Mittra E, Kunz PL, Kulke MH, Jacene H, Bushnell D, O'Dorisio TM, Baum RP, Kulkarni HR, Caplin M, Lebtahi R, Hobday T, Delpassand E, Van Cutsem E, Benson A, Srirajaskanthan R, Pavel M, Mora J, Berlin J, Grande E, Reed N, Seregni E, Öberg K, Lopera Sierra M, Santoro P, Thevenet T, Erion JL, Ruszniewski P, Kwekkeboom D, Krenning E. Phase 3 trial of ^{177}Lu-Dotatate for midgut neuroendocrine tumors. N Engl J Med. 2017;376:125-135.
2. Strosberg JR, Caplin ME, Kunz PL, Ruszniewski PB, Bodei L, Hendifar A, Mittra E, Wolin EM, Yao JC, Pavel ME, Grande E, Van Cutsem E, Seregni E, Duarte H, Gericke G, Bartalotta A, Mariani MF, Demange A, Mutevelic S, Krenning EP. ^{177}Lu-Dotatate plus long-acting octreotide versus high-dose long-acting octreotide in patients with midgut neuroendocrine tumours (NETTER-1): final overall survival and long-term safety results from an open-label, randomised, controlled, phase 3 trial. Lancet Oncol. 2021;22:1752-1763.
3. Kennedy KR, Claringbold P, Macdonald W, Boardman G, Ransom DT, Turner H. Long-term survival and toxicity in patients with progressive advanced neuroendocrine tumors treated with lutetium peptide radiolabelled radiotherapy: a Western Australian long-term follow-up study. J Clin Oncol. 2021;39:e16202.
4. Bodei L, Cremonesi M, Ferrari M, Pacifici M, Grana CM, Bartolomei M, Baio SM, Sansovini M, Paganelli G. Long-term evaluation of renal toxicity after peptide receptor radionuclide therapy with ^{90}Y-DOTATOC and ^{177}Lu-DOTATATE: the role of associated risk factors. Eur J Nucl Med Mol Imaging. 2008;35:1847-1856.
5. Valkema R, Pauwels SA, Kvols LK, Kwekkeboom DJ, Jamar F, de Jong M, Barone R, Walrand S, Kooij PPM, Bakker WH, Lasher J, Krenning EP. Long-term follow-up of renal function after peptide receptor radiation therapy with ^{90}Y-DOTA^{0},Tyr^{3}-octreotide and ^{177}Lu-DOTA^{0},Tyr^{3}-octreotate. J Nucl Med. 2005;46 Suppl 1:83S-91S.
6. Bodei L, Cremonesi M, Grana C, Rocca P, Bartolomei M, Chinol M, Paganelli G. Receptor radionuclide therapy with ^{90}Y-[DOTA]^{0}-Tyr^{3}-octreotide (^{90}Y-DOTATOC) in neuroendocrine tumours. Eur J Nucl Med Mol Imaging. 2004;31:1038-1046.
7. Moll S, Nickeleit V, Mueller-Brand J, Brunner FP, Maecke HR, Mihatsch MJ. A new cause of renal thrombotic microangiopathy: yttrium 90-DOTATOC internal radiotherapy. Am J Kidney Dis. 2001;37:847-851.
8. Hope TA, Allen-Auerbach M, Bodei L, Calais J, Dahlbom M, Dunnwald LK, Graham MM, Jacene HA, Lawhn Heath C, Mittra ES, Wright CL, Fendler WP, Herrmann K, Taïeb D, Kjaer A. SNMMI procedure standard/EANM practice guideline for SSTR PET: imaging neuroendocrine tumors. J Nucl Med. 2023;64:204-210.
9. Sundlöv A, Gustafsson J, Brolin G, Mortensen N, Hermann R, Bernhardt P, Svensson J, Ljungberg M, Tennvall J, Sjögreen Gleisner K. Feasibility of simplifying renal dosimetry in ^{177}Lu peptide receptor radionuclide therapy. EJNMMI Phys. 2018;5:12.
10. Chicheportiche A, Ben-Haim S, Grozinsky-Glasberg S, Oleinikov K, Meirovitz A, Gross DJ, Godefroy J. Dosimetry after peptide receptor radionuclide therapy: impact of reduced number of post-treatment studies on absorbed dose calculation and on patient management. EJNMMI Phys. 2020;7:5.
11. Siegel JA, Thomas SR, Stubbs JB, Stabin MG, Hays MT, Koral KF, Robertson JS, Howell RW, Wessels BW, Fisher DR, Weber DA, Brill AB. MIRD pamphlet no. 16: techniques for quantitative radiopharmaceutical biodistribution data acquisition and analysis for use in human radiation dose estimates. J Nucl Med. 1999;40:37S-61S.
12. Hope TA, et al. SNMMI consensus statement on patient selection and appropriate use of ^{177}Lu-DOTATATE peptide receptor radionuclide therapy. J Nucl Med. 2023;64:1417-1423.
13. Hänscheid H, Lapa C, Buck AK, Lassmann M, Werner RA. Dose mapping after endoradiotherapy with ^{177}Lu-DOTATATE/DOTATOC by a single measurement after 4 days. J Nucl Med. 2018;59:75-81.
14. Madsen MT, Menda Y, O'Dorisio TM, O'Dorisio MS. Technical note: single time point dose estimate for exponential clearance. Med Phys. 2018;45:2318-2324.
15. Del Prete M, Arsenault F, Saighi N, Zhao W, Buteau FA, Celler A, Beauregard JM. Accuracy and reproducibility of simplified QSPECT dosimetry for personalized ^{177}Lu-octreotate PRRT. EJNMMI Phys. 2018;5:25.
16. Larsson M, Bernhardt P, Svensson JB, Wängberg B, Ahlman H, Forssell-Aronsson E. Estimation of absorbed dose to the kidneys in patients after treatment with ^{177}Lu-octreotate: comparison between methods based on planar scintigraphy. EJNMMI Res. 2012;2:49.
17. Sandström M, Garske-Román U, Johansson S, Granberg D, Sundin A, Freedman N. Kidney dosimetry during ^{177}Lu-DOTATATE therapy in patients with neuroendocrine tumors: aspects on calculation and tolerance. Acta Oncol. 2018;57:516-521.
18. Sandström M, Freedman N, Fröss-Baron K, Kahn T, Sundin A. Kidney dosimetry in 777 patients during ^{177}Lu-DOTATATE therapy: aspects on extrapolations and measurement time points. EJNMMI Phys. 2020;7:73.

19. Gustafsson J, Taprogge J. Theoretical aspects on the use of single-time-point dosimetry for radionuclide therapy. Phys Med Biol. 2022;67:135006.
20. Guerriero F, Ferrari ME, Botta F, Fioroni F, Grassi E, Versari A, Sarnelli A, Pacilio M, Amato E, Strigari L, Bodei L, Paganelli G, Iori M, Pedroli G, Cremonesi M. Kidney dosimetry in ^{177}Lu and ^{90}Y peptide receptor radionuclide therapy: influence of image timing, time-activity integration method, and risk factors. Biomed Res Int. 2013;2013:935351.
21. Ljungberg M, Celler A, Konijnenberg MW, Eckerman KF, Dewaraja YK, Sjögreen-Gleisner K, Bolch WE, Brill AB, Fahey F, Fisher DR, Hobbs R, Howell RW, Meredith RF, Sgouros G, Zanzonico P, Bacher K, Chiesa C, Flux G, Michael Lassmann, Strigari L, Walrand S. MIRD Pamphlet No. 26: Joint EANM/MIRD guidelines for quantitative ^{177}Lu SPECT applied for dosimetry of radiopharmaceutical therapy. J Nucl Med. 2016;57:151-62.
22. Peterson AB, Mirando DM, Dewaraja YK. Accuracy and uncertainty analysis of reduced time point imaging effect on time-integrated activity for ^{177}Lu-DOTATATE PRRT in patients and clinically realistic simulations. EJNMMI Res. 2023;13:57.
23. Marin G, Vanderlinden B, Karfis I, Guiot T, Wimana Z, Reynaert N, Vandenberghe S, Flamen P. A dosimetry procedure for organs-at-risk in ^{177}Lu peptide receptor radionuclide therapy of patients with neuroendocrine tumours. Phys Med. 2018;56:41-49.
24. Andersson M, Johansson L, Eckerman K, Mattsson S. IDAC-Dose 2.1, an internal dosimetry program for diagnostic nuclear medicine based on the ICRP adult reference voxel phantoms. EJNMMI Res. 2017;7:88.
25. Rindi G, Mete O, Uccella S, Basturk O, La Rosa S, Brosens LAA, Ezzat S, de Herder WW, Klimstra DS, Papotti M, Asa SL. Overview of the 2022 WHO Classification of Neuroendocrine Neoplasms. Endocr Pathol. 2022;33:115-154.
26. Vija H. Introduction to xSPECT* technology: evolving multi-modal SPECT to become context-based and quantitative. Erlangen, Siemens Medical Solutions Inc. 2013.
27. Bolch WE, Jokisch D, Zankl M, Eckerman KF, Fell T, Manger R, Endo A, Hunt J, Kim KP, Petoussi-Henss N. ICRP publication 133: the ICRP computational framework for internal dose assessment for reference adults: specific absorbed fractions. Ann ICRP. 2016;45:5-73.
28. Chicheportiche A, Sason M, Zidan M, Godefroy J, Krausz Y, Gross DJ, Grozinsky-Glasberg S, Ben-Haim S. Impact of single-time-point estimates of ^{177}Lu-PRRT absorbed doses on patient management: validation of a trained multiple-linear-regression model in 159 patients and 477 therapy cycles. J Nucl Med. 2023;64:1610-1616.
29. Peters SMB, Mink MCT, Privé BM, de Bakker M, de Lange F, Muselaers CHJ, Mehra N, Witjes JA, Gotthardt M, Nagarajah J, Konijnenberg MW. Optimization of the radiation dosimetry protocol in lutetium-177-PSMA therapy: toward clinical implementation. EJNMMI Res. 2023;13:6.
30. Danieli R, Mileva M, Marin G, Kristanto P, Delbart W, Vanderlinden B, Wimana Z, Hendlisz A, Levillain H, Reynaert N, Flamen P, Karfis I. Evolution of dosimetric parameters through PRRT and potential impact on clinical practice: data from the prospective phase II LUMEN study. EJNMMI Res. 2024;14:110.
31. Pirozzi Palmese V, D'Ambrosio L, Di Gennaro F, et al. A comparison of simplified protocols of personalized dosimetry in NEN patients treated by radioligand therapy (RLT) with [^{177}Lu]Lu-DOTATATE to favor its use in clinical practice. Eur J Nucl Med Mol Imaging. 2023;50:1753-1764.
32. Mora-Ramirez E, Santoro L, Cassol E, Ocampo-Ramos JC, Clayton N, Kayal G, Chouaf S, Trauchessec D, Pouget JP, Kotzki PO, Deshayes E, Bardiès M. Comparison of commercial dosimetric software platforms in patients treated with ^{177}Lu-DOTATATE for peptide receptor radionuclide therapy. Med Phys. 2020;47:4602-4615.
33. Maroufpour S, Aryana K, Nasseri S, Fazeli Z, Arabi H, Momennezhad M. Validation of dosimetry programs (Olinda & IDAC) for evaluation of absorbed dose in ^{177}Lu-PSMA therapy of metastatic castration-resistant prostate cancer (mCRPC) using Monte Carlo simulation. EJNMMI Phys. 2024;11:102.
34. Tran-Gia J, Denis-Bacelar AM, Ferreira KM, Robinson AP, Calvert N, Fenwick AJ, Finocchiaro D, Fioroni F, Grassi E, Heetun W, Jewitt SJ, Kotzassarlidou M, Ljungberg M, McGowan DR, Scott N, Scuffham J, Sjögreen Gleisner K, Tipping J, Wevrett J, Lassmann M. A multicentre and multi-national evaluation of the accuracy of quantitative ^{177}Lu SPECT/CT imaging performed within the MRTDosimetry project. EJNMMI Phys. 2021;8:55.
35. Lechner W, Palmans H. Uncertainty estimation for dosimetry in radiation oncology. Phys Imaging Radiat Oncol. 2025;34:100773.

Original Article

Mol Imaging Radionucl Ther 2026;35(2):105-113 **DOI:***10.4274/mirt.galenos.2026.48108*

Potential of Lean Body Mass ^{18}F-FDG PET/CT Parameters to Predict Pathologic Findings in Overweight Endometrial Cancer Cases

Aşırı Kilolu Endometriyal Kanser Olgularında Patolojik Bulguları Tahmin Etmede Yağsız Vücut Kütlesi ^{18}F-FDG PET/BT Parametrelerinin Potansiyeli

Furkan Avcı[1], Alpay Tunç[1], Burçin Karaşah Erkek[2], Ahmet Aydın Özsaran[3], Gürdeniz Serin[4], Osman Zekioğlu[4], Zeynep Burak[1]

[1]*Ege University Faculty of Medicine, Department of Nuclear Medicine, İzmir, Türkiye*
[2]*Ağrı Training and Research Hospital, Clinic of Nuclear Medicine, Ağrı, Türkiye*
[3]*Ege University Faculty of Medicine, Department of Obstetrics and Gynecology, İzmir, Türkiye*
[4]*Ege University Faculty of Medicine, Department of Pathology, İzmir, Türkiye*

Abstract

Objectives: Endometrial cancer is the second most common gynaecologic cancer in women worldwide. Due to the biology of endometrial cancer, most patients are overweight. Standard uptake value (SUV) measurements are known to vary depending on the patient's body weight. We aimed to evaluate whether lean body mass-adjusted ^{18}F-fluorodeoxyglucose positron emission tomography/computed tomography (^{18}F-FDG PET/CT) parameters [lean body mass-corrected standardized uptake value (SUL)-based metrics] are superior to conventional SUV-based parameters for predicting adverse histopathologic features in overweight patients with endometrial cancer, and to explore their association with progression-free survival (PFS).

Methods: In this retrospective single-center study, 73 overweight patients with endometrial cancer who underwent preoperative ^{18}F-FDG PET/CT followed by primary surgery were included. SUV- and SUL-based metabolic parameters were compared with histopathologic risk factors. ROC analyses were performed to determine discriminatory performance and optimal cut-off values. PFS was assessed using Kaplan-Meier analysis.

Results: SUV_{mean} (SUL_{mean}) demonstrated significant associations with deep myometrial invasion, lymphovascular space invasion, lymph node involvement, and higher tumor grade. In ROC analysis, SUL_{mean} showed moderate discriminatory ability for lymph node involvement (area under the curve: 0.78). However, PFS did not differ significantly between groups stratified by the ROC-derived SUL_{mean} cut-off (log-rank p=0.46).

Conclusion: Lean body mass-adjusted PET parameters, particularly SUL_{mean}, were more strongly associated with adverse histopathologic features than conventional SUV metrics in overweight patients with endometrial cancer. Although SUL-based parameters may contribute to preoperative risk assessment, their prognostic value for survival remains uncertain.

Keywords: Endometrial cancer, lean-body-mass, ^{18}F-FDG PET/CT, SUV, SUL

Address for Correspondence: Zeynep Burak, Ege University Faculty of Medicine, Department of Nuclear Medicine, İzmir, Türkiye
E-mail: profdrzeynep@gmail.com **ORCID ID:** orcid.org/0000-0002-3187-9447
Received: 27.07.2025 **Accepted:** 03.05.2026 **Publication Date:** 04.06.2026

Cite this article as: Avcı F, Tunç A, Karaşah Erkek B, Özsaran AA, Serin G, Zekioğlu O, Burak Z. Potential of lean body mass ^{18}F-FDG PET/CT parameters to predict pathologic findings in overweight endometrial cancer cases. Mol Imaging Radionucl Ther. 2026;35(2):105-113.

Öz

Amaç: Endometriyal kanser, dünyada kadınlar arasında en yaygın ikinci jinekolojik kanserdir. Endometriyal kanserin biyolojisi nedeniyle, çoğu hasta aşırı kiloludur. Standart alım değeri (SUV) ölçümlerinin, hastanın vücut ağırlığına bağlı olarak değişebileceği bilinmektedir. Bu çalışmanın amacı, aşırı kilolu endometriyal kanserli hastalarda vücut yağsız kütlesine göre ayarlanmış ^{18}F-fluorodeoksiglukoz pozitron emisyon tomografi/bilgisayarlı tomografi (^{18}F-FDG PET/CT) parametrelerinin [yağsız vücut kütlesine göre düzeltme yapılmış standartlaştırılmış alım değeri (SUL) tabanlı ölçütler] konvansiyonel SUV tabanlı parametrelerden daha üstün olup olmadığını araştırmak ve bu parametrelerin progresyon-free survival (PFS) ile ilişkisini incelemektir.

Yöntem: Bu retrospektif tek merkezli çalışmada, preoperatif ^{18}F-FDG PET/CT çekimi yapılan ve ardından primer cerrahi uygulanan 73 aşırı kilolu endometriyal kanser hastası dahil edilmiştir. SUV- ve SUL tabanlı metabolik parametreler, histopatolojik risk faktörleriyle karşılaştırılmıştır. ROC analizleri, ayırıcı performansı ve optimal kesme değerlerini belirlemek için yapılmıştır. PFS, Kaplan-Meier analizi ile değerlendirilmiştir.

Bulgular: SUL_{mean} (SUL_{mean}), derin miyometrial invazyon, lenfovasküler alan invazyonu, lenf nodu tutulumu ve yüksek tümör derecesi ile anlamlı ilişkiler göstermiştir. ROC analizinde, SUL_{mean}, lenf nodu tutulumu için orta derecede ayırt edici bir yetenek göstermiştir (eğri altında alan: 0.78). Ancak, ROC tabanlı SUL_{mean} kesme değeri ile gruplar arasındaki PFS, anlamlı şekilde farklılık göstermemiştir (log-rank p=0.46).

Sonuç: Yağsız vücut kütlesine göre ayarlanmış PET parametreleri, özellikle SUL_{mean}, aşırı kilolu endometriyal kanserli hastalarda konvansiyonel SUV ölçütlerinden daha güçlü bir şekilde olumsuz histopatolojik özelliklerle ilişkilidir. SUL tabanlı parametreler, preoperatif risk değerlendirmesine katkı sağlasa da, hayatta kalma üzerindeki prognostik değerleri belirsizdir.

Anahtar Kelimeler: Endometriyal kanser, yağsız vücut kütlesi, ^{18}F-FDG PET/BT, SUV, SUL

Introduction

Endometrial cancer is the second most common gynecological malignancy among women worldwide (1,2). However, in terms of mortality, it ranks lower, which can largely be attributed to the fact that endometrial cancer is typically diagnosed at an early stage (3). Obesity is a well-established risk factor for endometrial cancer (1,4). With increasing obesity rates worldwide, the incidence of endometrial cancer has been rising steadily, posing a growing public health challenge. Importantly, obesity not only increases the risk of developing endometrial cancer but may also influence tumor biology, imaging characteristics, and perioperative risk assessment, thereby complicating preoperative evaluation (5).

Histopathological features are essential for prognostication and clinical management in endometrial cancer. Histologic grade and myometrial invasion depth are key determinants of tumor aggressiveness and recurrence risk. Lymphovascular space invasion (LVSI), and lymph node involvement are strong predictors of extrauterine spread and poor survival. Cervical involvement contributes to FIGO staging and surgical planning. p53 mutations reflect tumor proliferation and molecular subtype, particularly in high-grade lesions. Additionally, estrogen receptor/progesterone receptor (ER/PR) receptor expression is often associated with hormone responsiveness and favorable prognosis. Evaluating these parameters provides critical insight into disease behavior and supports individualized treatment strategies. Accurate preoperative identification of these adverse pathological features remains clinically relevant, as it may influence the extent of surgical staging, lymph node assessment, and adjuvant treatment decisions (6).

In the diagnostic and staging process of endometrial cancer, ^{18}F-fluorodeoxyglucose positron emission tomography/computed tomography (^{18}F-FDG PET/CT) imaging is widely used to assess tumor metabolism and disease burden. Traditional parameters such as the standardized uptake value (SUV) have long played a critical role in evaluating tumor metabolic activity. The metabolic data obtained from ^{18}F-FDG PET/CT can help guide more accurate and personalized treatment decisions, ultimately supporting cancer management and improving patient outcomes (7). Although SUV-based metrics provide a convenient and reproducible assessment of tumor metabolism, their accuracy can be compromised in populations with altered body composition, such as obese patients.

SUV measurements are known to vary depending on the patient's body weight. As body weight and body mass index (BMI) increase, SUV values in tumor tissues and normal tissues also tend to rise (8), potentially leading to inconsistent results across patients, and predicting therapy response within a patient (9). To overcome these limitations, lean body mass-corrected standardized uptake value (SUL) have emerged as a promising alternative, offering superior reproducibility across individuals with varying body compositions (10). Recent studies have shown that parameters like SUL maximum (SUL_{max}) provide more stable measurements than SUV, especially in patients with high BMI (11,12,13). However, data specifically addressing the clinical utility of lean body mass-adjusted (LBM) PET parameters in overweight or obese patients with endometrial cancer remain limited.

In this study, we aimed to evaluate whether metabolic and volumetric PET/CT parameters corrected for lean body mass are more effective in predicting pathological features in

overweight patients diagnosed with endometrial cancer. In addition, we explored the potential prognostic implications of LBM PET parameters by performing progression-free survival (PFS) analyses based on ROC derived cut-off values. Our goal was to determine whether SUL-based imaging metrics can enhance the accuracy of preoperative risk stratification and support more personalized treatment planning.

Materials and Methods

Study Population

This single-center retrospective study included consecutive patients diagnosed with endometrial cancer between January 2021 and December 2024. A total of 412 patients were initially screened. After applying predefined inclusion and exclusion criteria, 73 patients were included in the final analysis. The patient selection process is summarized in Figure 1. Surgical treatment, consisting of total abdominal hysterectomy with bilateral salpingo-oophorectomy and pelvic lymph node dissection, was performed within two weeks following PET/CT imaging in all cases.

Demographic characteristics, clinicopathological variables, and postoperative histopathological findings were retrieved from the institutional electronic medical records system. Histopathological evaluation included tumor grade, depth of myometrial invasion, LVSI, cervical stromal involvement, and lymph node status, when available. The approval has been granted by the Ethics Committee of Ege University Medical Research with (decision no: 25-3.1T/87, date: 20.03.2025).

PET/CT Acquisition and Image Analysis

All PET/CT scans were performed using the same PET/CT scanner (Biograph True Point 16; Siemens Healthcare, Henkester, Germany) in accordance with the Uniform Protocols for Imaging in Clinical Trials (UPICT) guidelines (14). PET/CT imaging was performed from the vertex to the mid-thigh following at least 6 hours of fasting, and blood glucose levels were confirmed to be below 150 mg/dL prior to tracer injection. The PET/CT images were independently analyzed by two experienced nuclear medicine physicians who were blinded to the patients' clinical information. Any discrepancies were resolved by consensus. PET/CT data were evaluated both visually and semi-quantitatively. Semi-quantitative parameters, including maximum SUV (SUV_{max}), SUV mean (SUV_{mean}), and peak (SUV_{peak}), were calculated for each lesion. Additionally, [maximum SUL (SUL_{max}), SUL mean (SUL_{mean}) and peak (SUL_{peak}] were derived using the James formula, implemented within the PET/CT workstation software. Volumetric parameters such as metabolic tumor volume (MTV) and total lesion glycolysis (TLG) were also obtained, along with TLG-LBM to assess overall metabolic burden.

Follow-up and Outcome Assessment

Patients were followed through review of electronic medical records. Recurrence status was assessed based on radiologic and/or histopathologic confirmation during follow-up. Recurrent disease was defined morphologically as radiologic evidence of locoregional or distant tumor reappearance after primary surgical treatment. PFS was calculated from the date of surgery to the date of documented recurrence or last clinical follow-up.

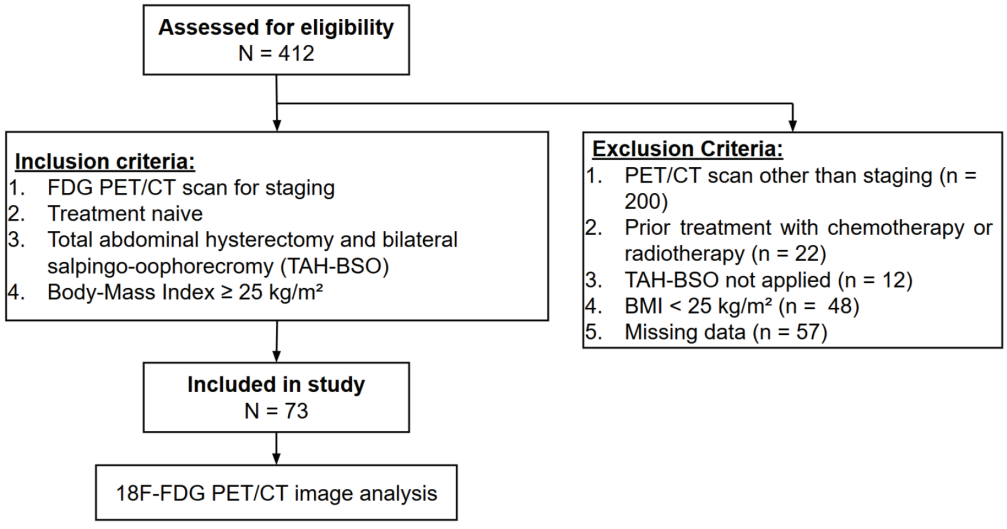

Figure 1. Flow diagram of patient selection
^{18}F-FDG PET/CT: ^{18}F-fluorodeoxyglucose positron emission tomography/computed tomography, TAH-BSO: Total abdominal hysterectomy and bilateral salpingo-oophorectomy, BMI: Body mass index

Patients without recurrence were censored at the time of last follow-up.

Statistical Analysis

For statistical analysis, we compared PET/CT-derived metabolic and volumetric parameters—including SUV_{max}, SUV_{mean}, SUV_{peak}, SUL_{max}, SUL_{mean}, SUL_{peak}, MTV, TLG, and SUL-TLG—with key clinicopathological features. These included histological grade, depth of myometrial invasion, LVSI, lymph node involvement, cervical stromal invasion, hormone receptor status (ER/PR), p53 mutation status, age at diagnosis, and tumor size. Continuous variables were assessed for correlations using Spearman's rank correlation coefficient. Group comparisons were performed using non-parametric tests (Mann-Whitney U or Kruskal-Wallis) as appropriate. ROC curve analyses were conducted to evaluate the discriminative ability of PET/CT parameters for relevant binary outcomes, and optimal cut-off values were determined using the Youden J index. All tests were two-tailed, and a p-value of <0.05 was considered statistically significant. All statistical analyses were conducted using SPSS version 25 (IBM Corp., Armonk, NY, USA).

Results

A total of 73 patients with endometrial cancer who underwent preoperative ^{18}F-FDG PET/CT followed by primary surgical treatment were included. Baseline clinical characteristics, histopathologic features, and follow-up data are summarized in Table 1. The study population predominantly consisted of patients with early-stage disease, while individual histopathologic risk factors—including deep myometrial invasion, LVSI, cervical stromal involvement, and lymph node metastasis—were variably present.

The distribution of PET-derived metabolic and volumetric parameters, including SUV-based, SUL-based, and volumetric measurements, is presented in Table 2. All PET parameters demonstrated non-normal distributions and were therefore summarized using median and interquartile range values.

Comparisons of PET-derived metabolic parameters according to adverse histopathologic features are detailed in Table 3. Among evaluated parameters, SUL-based measurements demonstrated significant differences across several adverse pathologic characteristics, including LVSI and lymph node involvement. Representative PET/CT images illustrating differences in primary tumor FDG uptake according to LVSI status are shown in Figure 2. Both SUV_{mean} and SUL_{mean} differed significantly according to the depth of myometrial invasion.

Table 1. Baseline clinical and histopathologic characteristics of the study population

Total patient	**n**	**73**
Recurrent malignancy	n (%)	5 (6.8)
Continuous variables		
Age (years)	Median [IQR]	61 (53-66)
BMI (kg/m²)	Median [IQR]	32.4 (29.3-38.6)
Pre-operative CA-125 (U/mL)	Median [IQR]	14 (10-23.5)
Tumor size (cm)	Median [IQR]	3.5 (2.5-5)
Follow-up duration (months)	Median [IQR]	28 (15-41)
Categorical variables		
FIGO stage, n (%)	Stage 1	58 (79.5)
	Stage 2	6 (8.2)
	Stage 3	9 (12.3)
Histologic type, n (%)	Endometroid	63 (86.3)
	Non-endometroid	10 (13.7)
Histologic tumor grade, n (%)	Grade 1	10 (13.7)
	Grade 2	52 (71.2)
	Grade 3	11 (15.1)
Myometrial invasion status, n (%)	Inner half (<1/2)	47 (64.4)
	Outer half (≥1/2)	26 (35.6)
Lymphovascular space invasion, n (%)	Absent	53 (72.6)
	Present	20 (27.4)
Cervix involvement, n (%)	Absent	64 (87.7)
	Present	9 (12.3)
Lymph node involvement, n (%)	No dissection	16 (21.9)
	Negative	52 (71.2)
	Positive	5 (6.8)
Microsatellite instability mutation, n (%)	Unexamined	17 (23.3)
	Negative	38 (52.1)
	Positive	18 (24.7)
p53 mutation, n (%)	Wild-type	57 (78.1)
	Aberrant-type	16 (21.9)
Estrogen receptor expression, n (%)	Negative	4 (5.5)
	Positive	69 (94.5)
Progesterone receptor expression, n (%)	Negative	10 (13.7)
	Positive	63 (86.3)

Continuous variables are presented as mean ± standard deviation or median (interquartile range) according to distribution. Categorical variables are presented as number (percentage). BMI:Body mass index, LVSI: Lymphovascular space invasion, MSI: Microsatellite instability, FIGO: International Federation of Gynecology and Obstetrics, IQR: Interquartile range, CA-125: Cancer antigen 125

Table 2. Distribution of ^{18}F-FDG PET/CT derived metabolic and volumetric parameters	
Parameter	**Median [IQR]**
SUV_{max}	19.81 [14.88-29.05]
SUV_{mean}	9.1 [7.23-11.52]
SUV_{peak}	13.71 [9.15-20.76]
SUL_{max}	11.37 [8.07-15.54]
SUL_{mean}	4.91 [3.94-6.28]
SUL_{peak}	7.50 [5.05-10.50]
MTV	8.71 [4.30-20.37]
TLG	72.06 [32.23-197.87]
SUL-TLG	39.42 [17.01-117.41]

Data are presented as median (interquartile range) due to non-normal distribution. SUV: Standardized uptake value, SUL: Lean body mass-corrected standardized uptake value, MTV: Metabolic tumor volume, TLG: Total lesion glycolysis, IQR: Interquartile range, ^{18}F-FDG PET/CT: ^{18}F-fluorodeoxyglucose positron emission tomography/computed tomography

PET-derived metabolic parameters also differed significantly across histologic tumor grades, as shown in Table 4. Global differences were observed for multiple SUV- and SUL-based parameters, including SUL_{mean}. Pairwise post-hoc analyses revealed significant differences primarily between low-grade and higher-grade tumors, whereas no significant differences were observed between intermediate- and high-grade tumors.

Spearman correlation analyses demonstrated moderate to strong positive correlations between tumor size and volumetric PET parameters, particularly MTV and TLG (r values ranging from approximately 0.68 to 0.73, p<0.001). SUV_{mean} and SUL_{mean} also showed significant positive correlations with tumor size, although with lower correlation coefficients (r=0.38-0.50, p<0.001).

Table 3. Comparison of PET-derived metabolic parameters according to adverse pathologic features			
Myometrial invasion status	**Inner half (< 1/2), median [IQR]**	**Outer half (≥ 1/2), median [IQR]**	**p-value**
SUV_{mean}	8.16 [7.13-10.31]	10.81 [7.84-12.71]	0.024
SUL_{mean}	4.73 [3.76-5.43]	5.64 [4.22-7.57]	0.022
Lymphovascular space invasion	**Absent, median [IQR]**	**Present, median [IQR]**	**p-value**
SUL_{mean}	4.57 [3.73-5.76]	5.70 [4.65-7.01]	0.015
Lymph node involvement	**Negative, median [IQR]**	**Positive, median [IQR]**	**p-value**
SUL_{mean}	5.01 [4.05-6.44]	6.56 [5.54-12.70]	0.037

Data are presented as median (interquartile range). Comparisons between two groups were performed using the Mann-Whitney U test. A two-tailed p-value<0.05 was considered statistically significant
IQR: Interquartile range, SUV: Standardized uptake value, SUL: Lean body mass-corrected standardized uptake value, PET: Positron emission tomography

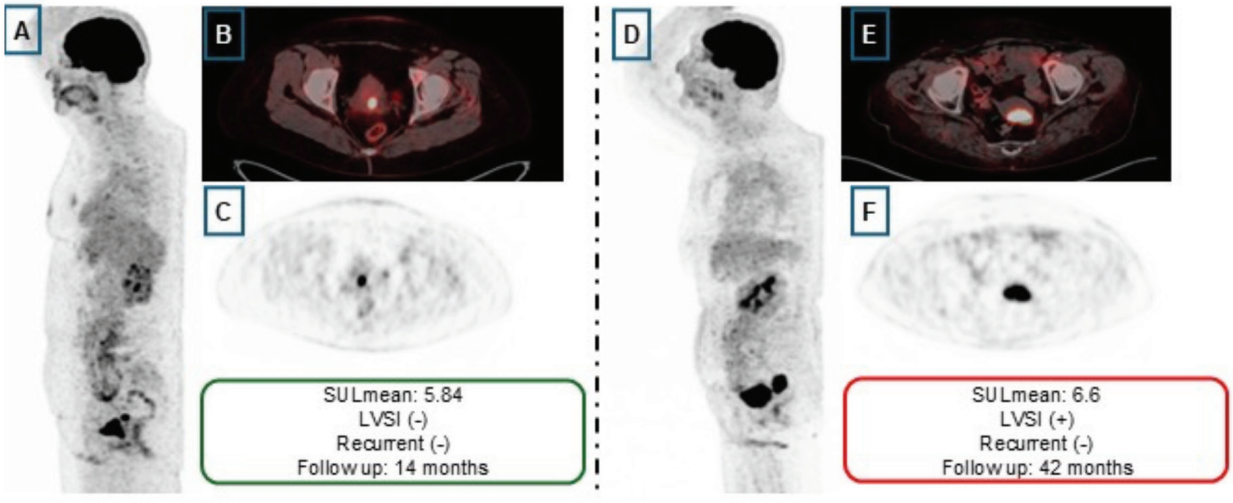

Figure 2. Representative ^{18}F-FDG PET/CT images of primary endometrial tumors according to LVSI status. (A-C) LVSI-negative case, (D-F) LVSI-positive case. (A, D) MIP images; (B, E) axial fused PET/CT; (C, F) axial PET images. Both patients were non-recurrent during follow-up
^{18}F-FDG PET/CT: ^{18}F-fluorodeoxyglucose positron emission tomography/computed tomography, LVSI: Lymphovascular space invasion. MIP: Maximum intensity projection, SUL: Lean body mass-corrected standardized uptake value

Preoperative cancer antigen 125 levels demonstrated weak to moderate correlations with tumor size and volumetric PET-derived parameters (r=0.30-0.40, p<0.05).

The diagnostic performance of PET-derived parameters for predicting individual histopathologic risk factors was evaluated using receiver operating characteristic analysis, with results summarized in Table 5. SUL_{mean} demonstrated higher discriminative ability compared with SUV-based parameters for the prediction of LVSI and lymph node involvement.

ROC analysis was performed to evaluate the diagnostic performance of PET-derived parameters for predicting individual histopathologic risk factors (Table 5). Among the evaluated parameters, SUL_{mean} demonstrated the highest discriminative ability for lymph node involvement. An optimal SUL_{mean} cut-off value of 6.04 was identified based on the Youden index (Youden J =0.55), yielding a sensitivity of 80%, specificity of 75%, positive predictive value of 76%, and negative predictive value of 78% for the prediction of lymph node involvement.

Because lymph node involvement represents a clinically relevant adverse prognostic factor and SUL_{mean} demonstrated the strongest diagnostic performance for this endpoint, the ROC-derived cut-off value of 6.04 was selected for subsequent survival analyses. Patients were dichotomized into low (≤6.04) and high (>6.04) SUL_{mean} groups according to this threshold. Kaplan-Meier analysis was performed to assess PFS. During follow-up, recurrence events occurred in a limited number of patients. Survival distributions did not differ significantly between the two groups (log-rank p=0.46; Figure 3). Median PFS was not reached in either group due to the low event rate. Given the limited number of events, further survival modeling was not conducted.

Discussion

In this retrospective cohort of overweight patients with endometrial cancer, lean body mass-adjusted PET/CT parameters—particularly SUL_{mean}—demonstrated

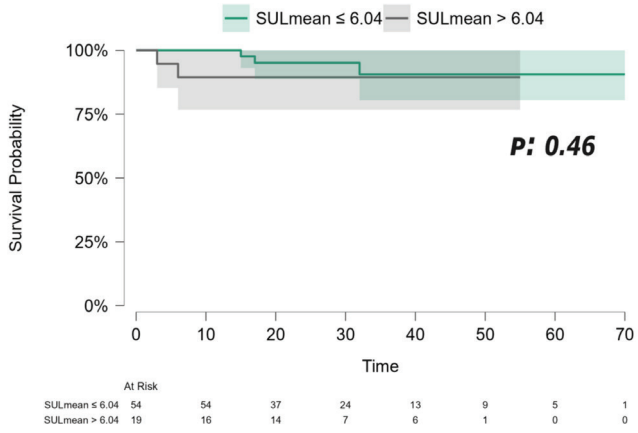

Figure 3. Kaplan-Meier curves for progression-free survival stratified by SUL_{mean} cut-off (6.04). Survival distributions were compared using the log-rank test
SUL: Lean body mass-corrected standardized uptake value

Table 4. Comparison of PET-derived metabolic parameters across histologic tumor

PET parameters	Grade 1, median [IQR]	Grade 2, median [IQR]	Grade 3, median [IQR]	p-value
SUV_{mean}	6.58 [5.38-9.42]	9.03 [7.29-11.62]	9.96 [7.79-13.56]	0.050
SUL_{max}	7.67 [6.45-11.29]	11.55 [9.07-15.02]	16.30 [8.89-19.76]	0.041
SUL_{peak}	4.79 [3.94-7.05]	7.65 [5.72-10.05]	10.5 [5.63-14.44]	0.037
SUL_{mean}	3.90 [2.88-5.20]	4.93 [4.12-5.82]	6.56 [4.57-8.68]	0.025

Data are presented as median (interquartile range). Differences among groups were assessed using the Kruskal-Wallis test. A two-tailed p-value<0.05 was considered statistically significant
IQR: Interquartile range, SUV: Standardized uptake value, SUL: Lean body mass-corrected standardized uptake value, PET: Positron emission tomography

Tablo 5. ROC analysis of PET-derived parameters for prediction of histopathologic risk factors

Outcome	Parameter	AUC (95% CI)	Cut-off	Sensitivity (%)	Specificity (%)	PPV (%)	NPV (%)
Myometrial invasion status	SUV_{mean}	0.34 (0.20-0.47)	9.56	29	34	31	33
Myometrial invasion status	SUL_{mean}	0.33 (0.20-0.47)	5.83	17	50	25	37
Lymphovascular space invasion	SUL_{mean}	0.68 (0.55-0.81)	5.9	50	81	72	61
Lymph node involvement	SUL_{mean}	0.78 (0.58-0.98)	6.04	80	75	76	78

Optimal cut-off values were determined using the Youden index. Sensitivity and specificity are reported for the corresponding cut-off values
AUC: Area under the curve, CI: Confidence interval, SUV: Standardized uptake value, SUL: Lean body mass-corrected standardized uptake value, PPV: Positive predictive value, NPV: Negative predictive value

stronger and more consistent associations with adverse histopathologic features than conventional SUV-based metrics. Specifically, SUL_{mean} was significantly higher in tumors with deep myometrial invasion, LVSI, lymph node involvement, and higher histologic grade. In ROC analyses, SUL_{mean} showed moderate discriminative ability for LVSI and the highest performance for lymph node involvement, whereas SUV-based parameters were less consistent across these endpoints.

From a biological and methodological perspective, these findings suggest that lean body mass correction may reduce variability introduced by excess adipose tissue and provide a metabolically more stable estimate of tumor glycolytic activity in overweight individuals. SUV measurements are known to be influenced by total body weight and adiposity, potentially leading to overestimation of uptake in obese patients. In contrast, lean body SUL reduce this dependency and improve inter-patient comparability (12,13,15).

While both SUV_{mean} and SUL_{mean} were associated with depth of myometrial invasion, SUL_{mean} demonstrated additional discriminatory value for LVSI and nodal metastasis, two features closely linked to extrauterine spread and the need for comprehensive surgical staging in accordance with current guidelines (6,16). Notably, SUL_{mean} values increased stepwise across tumor grades, with the most pronounced differences observed between low-grade and higher-grade tumors, supporting its potential role as a marker of tumor aggressiveness.

Importantly, although a ROC-derived SUL_{mean} cut-off of 6.04 demonstrated reasonable sensitivity and specificity for lymph node involvement, Kaplan-Meier analysis did not reveal a statistically significant difference in PFS between low and high SUL_{mean} groups (log-rank p=0.46). This negative survival result must be explicitly acknowledged. Several factors likely contributed to the absence of a significant PFS difference: the predominance of early-stage disease, the very low number of recurrence events (n=5), and a follow-up duration that may be insufficient to capture late recurrences in this generally favorable-risk population (1,2,3). In addition, although SUL_{peak} is emphasized in PERCIST criteria for treatment response assessment (7), the prognostic role of baseline SUL-based parameters in endometrial cancer—particularly in relation to PFS—remains insufficiently studied. Therefore, our findings do not support the use of SUL_{mean} as an independent survival predictor and should be interpreted cautiously.

The present results are partially consistent with prior studies reporting associations between FDG uptake and adverse pathologic features in endometrial cancer. According to Yao et al. (17), no significant correlation was observed between estrogen receptor (ER) expression and FDG uptake on PET/CT. Takagi et al. (18) demonstrated a significant association between SUV_{max} and histological grade, while Vural Topuz et al. (19) reported correlations between SUV_{max}, MTV, TLG, and several adverse pathologic features, including nodal involvement. However, these analyses were based on weight-normalized SUV metrics and did not incorporate lean body mass correction. Studies focusing on SUL in gynecologic malignancies have suggested potential advantages in reflecting tumor differentiation (11), yet direct comparisons between SUV- and SUL-based parameters in overweight endometrial cancer populations remain limited. Sürer Budak et al. (20) reported that SUV_{max} and apparent diffusion coefficient minimum were independently associated only with deep myometrial invasion, with moderate predictive performance. In contrast, our findings suggest that lean body mass-adjusted PET parameters were associated with a broader spectrum of adverse histopathologic features, including LVSI and nodal involvement. Although magnetic resonance imaging was not evaluated in our study, the incorporation of SUL-based metrics may provide complementary metabolic information beyond myometrial invasion assessment.

The theoretical advantage of SUL is particularly relevant in endometrial cancer, a malignancy strongly associated with obesity (4,5). Because SUV is normalized to total body weight, excess adipose tissue—which exhibits relatively low FDG uptake—may artificially inflate calculated tumor uptake values (8). Lean body mass correction addresses this limitation and has been shown to reduce variability related to body composition (12,13,15). Our findings support this methodological rationale by demonstrating stronger associations between SUL_{mean} and adverse histopathologic characteristics in an overweight cohort.

Nevertheless, not all evaluated parameters performed equally. Volumetric metrics such as MTV and TLG correlated strongly with tumor size, which is expected given their volumetric nature, but they did not consistently outperform SUL-based indices for specific adverse features. Furthermore, metabolic parameters did not show significant associations with certain molecular markers, including p53 status, despite its recognized biological relevance in endometrial carcinoma (21). This lack of association may reflect limited statistical power, early-stage predominance, or the fact that FDG uptake captures glucose metabolism rather than the full spectrum of molecular alterations.

This study has several strengths. The exclusive inclusion of overweight patients addresses a clinically relevant population in which SUV variability is most problematic.

PET/CT imaging was performed within a short preoperative interval using a standardized protocol consistent with UPICT recommendations (14). Image interpretation was conducted by experienced nuclear medicine physicians blinded to clinical data, minimizing observer bias. Comprehensive histopathologic correlation and ROC-based cut-off analyses further enhance the interpretability of the findings, although these thresholds require external validation.

Study Limitations

However, important limitations must be acknowledged. The retrospective, single-center design introduces potential selection bias. The sample size was modest, and the number of lymph nodes–positive cases and recurrences was low, limiting statistical power. Multivariable survival analysis could not be performed due to the small number of PFS events. External validation in an independent cohort was not undertaken. Moreover, the predominance of early-stage disease restricts extrapolation to advanced-stage or high-risk populations.

Conclusion

Lean body mass–adjusted PET/CT parameters, particularly SUL_{mean}, demonstrated stronger associations with adverse histopathologic features than conventional SUV-based metrics in overweight patients with endometrial cancer. SUL_{mean} showed moderate discriminatory performance for LVSI and lymph node involvement, suggesting that lean body mass correction may enhance metabolic characterization in populations with elevated BMI. However, SUL_{mean} did not predict PFS in this predominantly early-stage cohort. These findings indicate that SUL-based parameters may contribute to preoperative risk assessment in overweight patients, but their prognostic significance remains uncertain. Prospective, multicenter studies with larger event numbers are required to validate these observations and to clarify the role of SUL metrics in clinical decision-making.

Ethics

Ethics Committee Approval: The approval has been granted by the Ethics Committee of Ege University Medical Research with (decision no: 25-3.1T/87, date: 20.03.2025).

Informed Consent: This single-center retrospective study.

Footnotes

Authorship Contributions

Surgical and Medical Practices: A.A.Ö., G.S., O.Z., Concept: F.A., Z.B., Design: F.A., Z.B., Data Collection or Processing: F.A., A.T., Analysis or Interpretation: F.A., B.K.E., Literature Search: F.A., A.T., Writing: F.A., B.K.E., Z.B.

Conflict of Interest: No conflict of interest was declared by the authors.

Financial Disclosure: The authors declared that this study has received no financial support.

Refereneces

1. Crosbie EJ, Kitson SJ, McAlpine JN, Mukhopadhyay A, Powell ME, Singh N. Endometrial cancer. Lancet. 2022;399:1412-1428.
2. International Agency for Research on Cancer. Global Cancer Observatory. Cancer Today. https://gco.iarc.fr/today/en/dataviz/bars?mode=cancer&group_populations=1&sexes=2 (2024, accessed January 19, 2025).
3. Turkish Society of Gynecologic Oncology. Endometrial Cancer Management Guidelines. https://trsgo.org/files/yonetim-kilavuzlari/Endometrium-Kanseri.pdf (2023, accessed January 19, 2025).
4. McDonald ME, Bender DP. Endometrial cancer: obesity, genetics, and targeted agents. Obstet gynecol Clin North Am. 2019;46:89-105.
5. Fasmer KE, Sæterstøl J, Ljunggren MBS, Brun AMK, Pijnenborg JMA, Woie K, Krakstad C, Haldorsen I. S. Abdominal fat distribution in endometrial cancer: from diagnosis to follow-up. BMC Cancer 2025;25:879.
6. Concin N, Matias-Guiu X, Cibula D, Colombo N, Creutzberg CL, Ledermann J, Mirza M. R., Vergote I., Abu-Rustum NR, Bosse T, Chargari C, Espenel S, Fagotti A, Fotopoulou C, Gatius S, González-Martin A, Lax S, Levy B, Lorusso D, Macchia G, Nout R. A. ESGO-ESTRO-ESP guidelines for the management of patients with endometrial carcinoma: update 2025. Lancet Oncol. 2025;26:e423-e435.
7. Wahl RL, Jacene H, Kasamon Y, Lodge MA. From RECIST to PERCIST: Evolving considerations for PET response criteria in solid tumors. J Nucl Med. 2009;50Suppl 1:122S-150S.
8. Thie JA. Understanding the standardized uptake value, its methods, and implications for usage. J Nucl Med. 2004;45:1431-1434.
9. Ziai P, Hayeri MR, Salei A, Salavati A, Houshmand S, Alavi A, Teytelboym OM. Role of optimal quantification of FDG PET imaging in the clinical practice of radiology. Radiographics 2016;36:481-496.
10. Aroldi F, Lord SR. Window of opportunity clinical trial designs to study cancer metabolism. Br J Cancer. 2020;122:45-51.
11. Mititelu R, Sîrbu C, Cuzino D, Jinga M, Radu F, Mazilu C, Spiridon PM. PET-CT with ^{18}F-FDG in gynecological malignancies. Prognostic significance of the standardized uptake value. Romanian J Mil Med. 2024;127:162-167.
12. Gafita A, Calais J, Franz C, Rauscher I, Wang H, Robertson A, Czernin J, Weber WA, Eiber M. Evaluation of SUV normalized by lean body mass (SUL) in ^{68}Ga-PSMA11 PET/CT: a bi-centric analysis. EJNMMI Res. 2019;9:103.
13. Sarikaya I, Albatineh AN, Sarikaya A. Revisiting weight-normalized SUV and lean-body-mass-normalized SUV in PET Studies. J Nucl Med Technol. 2020;48:163-167.
14. Graham MM, Wahl RL, Hoffman JM, Yap JT, Sunderland JJ, Boellaard R, Linden HM, Kinahan PE. Summary of the UPICT protocol for ^{18}F-FDG PET/CT imaging in oncology clinical trials. J Nucl Med. 2015;56:955-961.
15. Jochimsen TH, Zeisig V, Schulz J, Butz M, Barthel H, Sabri O, Sattler B. Lean body mass correction of standardized uptake value in simultaneous whole-body positron emission tomography and magnetic resonance imaging. Phys Med Biol. 2015;60:4651-4664.
16. Altindag SD, Yiğit S, Şen S. Is microcystic, elongated, and fragmented pattern of myometrial invasion in endometrioid endometrial carcinoma associated with survival? Turk J Med Sci. 2022;52:1569-1579.

17. Yao X, Tan X, Zhang H, Yuan H, Zeng B, He L, Jiang L. Relationship between ^{18}F-fluorodeoxyglucose PET/computed tomography metabolic parameters and clinicopathology in endometrial cancer. Nucl Med Commun. 2022;43:1233-1238.
18. Takagi H, Sasagawa T, Shibata T, Minato H, Takahashi T. Association between ^{18}F-fluorodeoxyglucose-PET/CT and histological grade of uterine endometrial carcinoma. Taiwan J Obstet Gynecol. 2018;57:283-288.
19. Vural Topuz Ö, Aksu A, Erinç SR, Tokgözoğlu N, Tamam MÖ. The evaluation of preoperative ^{18}F-FDG PET/CT in patients with endometrial cancer and the correlation between PET parameters and postoperative pathology results. Mol Imaging Radionucl Ther. 2022;31:16-22.
20. Sürer Budak E, Toptaş T, Aydın F, Öner AO, Çevikol C, Şimşek T. Correlation of minimum apparent diffusion coefficient and maximum standardized uptake value of the primary tumor with clinicopathologic characteristics in endometrial cancer. Mol Imaging Radionucl Ther. 2017;26:24-32.
21. Morice P, Leary A, Creutzberg C, Abu-Rustum N, Darai E. Endometrial cancer. Lancet. 2016;387:1094-1108.

Interesting Image

Mol Imaging Radionucl Ther 2026;35(2):114-116 ***DOI:****10.4274/mirt.galenos.2025.35253*

Bilateral Renal Metastases from Lung Adenocarcinoma Revealed on ^{18}F-FDG PET/CT

^{18}F-FDG PET/BT'de Saptanan Akciğer Adenokarsinomundan Kaynaklanan Bilateral Böbrek Metastazları

Intissar El Moatassim, Ayat Mouaden, Kenza Bouzidi, Imad Ghfir, Hasnae Guerrouj

Ibn Sina Teaching Hospital, Mohammed V University, Department of Nuclear Medicine, Rabat, Morocco

Abstract

Lung cancer is the leading cause of cancer-related deaths worldwide. While metastasis to distant organs is commonly described, renal metastasis remains rare and uncommon. In this paper, we present the case of a 53-year-old man with a history of left apical lung adenocarcinoma who underwent fluorodeoxyglucose (FDG) positron emission tomography/computed tomography (CT) for suspected recurrence. The scan revealed a recurrent pulmonary mass with metastatic spread, notably showing intense bilateral focal FDG uptake in the kidneys. A metastatic origin was suspected and subsequently confirmed by CT-guided renal biopsy.

Although rare and typically observed in advanced stages of the disease, this case underscores the importance of carefully evaluating focal FDG uptake in the renal cortex to ensure accurate staging and optimal management of oncologic patients.

Keywords: Fluorodesoxyglucose, positron emission tomography/CT, lung adenocarcinoma, renal metastasis

Öz

Akciğer kanseri, dünya çapında kansere bağlı ölümlerin önde gelen nedenidir. Uzak organlara metastaz sıklıkla bildirilirken, böbrek metastazı nadirdir. Bu yazıda, sol apikal akciğer adenokarsinomu öyküsü olan ve şüpheli nüks nedeniyle florodeoksiglukoz (FDG) pozitron emisyon tomografisi/bilgisayarlı tomografi (BT) çekilen 53 yaşında bir erkek hastayı sunuyoruz. Taramada, metastatik yayılımı olan ve özellikle böbreklerde yoğun bilateral fokal FDG tutulumu gösteren rekürren bir akciğer kitlesi tespit edildi. Metastatik kökenden şüphelenildi ve ardından BT eşliğinde böbrek biyopsisi ile doğrulandı.

Nadir olmasına ve genellikle hastalığın ileri evrelerinde görülmesine rağmen, bu olgu, onkolojik hastaların doğru evrelemesini ve optimal yönetimini sağlamak için böbrek korteksindeki fokal FDG tutulumunun dikkatlice değerlendirilmesinin önemini vurgulamaktadır.

Anahtar Kelimeler: Florodesoksiglukoz pozitron emisyon tomografisi/BT, akciğer adenokarsinomu, böbrek metastazı

Address for Correspondence: Intissar El Moatassim, Ibn Sina Teaching Hospital, Mohammed V University, Department of Nuclear Medicine, Rabat, Morocco
E-mail: intissar.elmoatassim@gmail.com **ORCID ID:** orcid.org/0009-0005-4510-4940
Received: 19.07.2025 **Accepted:** 13.10.2025 **Epub:** 26.11.2025 **Publication Date:** 04.06.2026

Cite this article as: El Moatassim I, Mouaden A, Bouzidi K, Ghfir I, Guerrouj H. Bilateral renal metastases from lung adenocarcinoma revealed on ^{18}F-FDG PET/CT. Mol Imaging Radionucl Ther. 2026;35(2):114-116.2026;35(2):114-116.

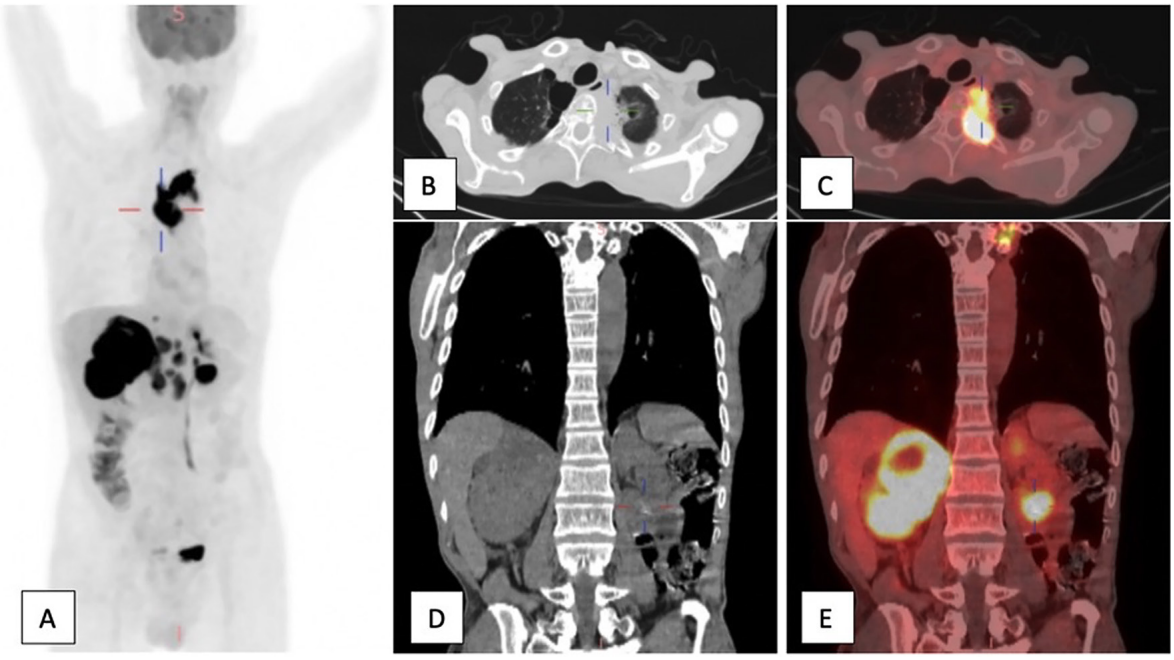

Figure 1. ^{18}F-fluorodeoxyglucose-positron emission tomography/computed tomography (^{18}F-FDG PET/CT) whole body maximum intensity projection image (A) axial CT image (B) and fused image (C) showing left apical lung mass with intense FDG uptake, consistent with recurrent lung adenocarcinoma. Coronal CT image (D) and fused image (E) demonstrate a voluminous right adreno-renal mass with intense hypermetabolism and focal uptake in the lower pole of the left kidney, suggesting bilateral metastases, which was subsequently confirmed histologically.

A 53-year-old man with a history of poorly differentiated adenocarcinoma of the left lung underwent whole-body ^{18}F-FDG PET/CT for suspected recurrence. The PET scan, coupled with a low-dose CT scan (dose length product =1321 mGy:cm), was performed 60 minutes after the injection of 6.7 mCi of FDG. It revealed a hypermetabolic left upper-lobe lung mass [maximum standard uptake values (SUV_{max}) =21.5] with contiguous vertebral involvement (B, C) and multiple supradiaphragmatic and infradiaphragmatic lymphadenopathy. Notably, bilateral renal involvement was identified: a large, isodense, hypermetabolic mass infiltrating the right kidney and the adrenal gland (SUV_{max} =22) and a second hypodense lesion demonstrating intense focal FDG uptake (SUV_{max} =22.6) in the lower pole of the left renal cortex (D,E). A CT-guided renal biopsy was performed, and immunohistochemical analysis confirmed metastatic adenocarcinoma of pulmonary origin. This resulted in disease upstaging and initiation of systemic pemetrexed monotherapy. Renal metastases are an uncommon finding; historically, they have been diagnosed only post-mortem and typically originate from lung tumors (1). They are often clinically silent, may be solitary, multifocal, unilateral, or bilateral, are difficult to distinguish from primary renal malignancies on conventional imaging, and are most often observed in advanced stages of the disease, generally in the context of widespread dissemination (2). ^{18}F-FDG PET/CT, commonly used in staging and restaging of lung cancer, plays a crucial role in identifying unusual metastatic patterns (3); its sensitivity in the detection of renal lesions is, however, limited due to the physiological excretion of ^{18}F-FDG through the urinary tract and depends on lesion size and location (4). Although kidney metastases are rare, the few reported cases of kidney metastases highlight that renal FDG uptake can be overlooked or misinterpreted as tracer retention because of the high background activity (4,5). To date, there are no specific PET/CT findings that reliably distinguish renal metastases from primary renal tumors. In this case, a metastatic origin was strongly suspected due to bilateral, large, and intensely hypermetabolic renal lesions, their hypodense appearance on CT, and the known metastatic spread to other organs. Nevertheless, histological confirmation was essential to exclude synchronous primary renal tumors, thereby ensuring adequate staging of the disease and the implementation of appropriate treatment strategies.

Ethics

Informed Consent: Informed consent was obtained from the patient for publication.

Footnotes

Authorship Contributions

Surgical and Medical Practices: I.E.M., A.M., I.G., H.G., Concept: I.E.M., A.M., K.B., H.G., Design: I.E.M., K.B., Data Collection or Processing: I.E.M., A.M., Analysis or Interpretation: I.E.M., A.M., I.G., H.G., Literature Search: I.E.M., Writing: I.E.M., A.M.

Conflict of Interest: No conflicts of interest were declared by the authors.

Financial Disclosure: The authors declare that this study has received no financial support.

References

1. Lian H, Pan X, Hong B, Min J, Huang F. Metastases to the kidney from primary lung cancer: clinicopathological analysis of six cases in a single center. Diagn Pathol. 2023;18:60.
2. Zhou C, Urbauer DL, Fellman BM, Tamboli P, Zhang M, Matin SF, Wood CG, Karam JA. Metastases to the kidney: a comprehensive analysis of 151 patients from a tertiary referral centre. BJU Int. 2016;117:775-782.
3. Halaç M, Özhan M, Yilmaz Aksoy S, Vatankulu B, Aliyev A, Asa S, Atahan E, Sağer MS, Sönmezoğlu K. The role of FDG-PET/CT in detecting unsuspected and unknown distant metastasis in the initial staging of NSCLC. Turk J Med Sci. 2014;44:1029-1040.
4. Aras M, Dede F, Ones T, Inanır S, Erdil TY, Turoğlu HT. Is The value of FDG PET/CT in evaluating renal metastasis underestimated? A case report and review of the literature. Mol Imaging Radionucl Ther. 2013;22:109-112.
5. Zhang J, Dong A, Wang Y. FDG PET/CT in solitary isolated renal metastasis from squamous cell lung cancer. Clin Nucl Med. 2024;49:e50-e51.

Interesting Image

Mol Imaging Radionucl Ther 2026;35(2):117-119 ***DOI:****10.4274/mirt.galenos.2025.51196*

Complete Treatment Response of Isolated Lacrimal IgG4-Related Disease on ^{18}F-FDG PET/CT Imaging

İzole Lakrimal IgG4 İlişkili Hastalıkta ^{18}F-FDG PET/BT'de Tam Tedavi Yanıtı

Ali Kibar, Sertaç Asa, Onur Erdem Şahin, Lebriz Uslu-Beşli, Sait Sağer, Kerim Sönmezoğlu, Haluk Burçak Sayman

İstanbul University-Cerrahpaşa, Cerrahpaşa Faculty of Medicine, Department of Nuclear Medicine, İstanbul, Türkiye

Abstract

We describe a case of a 57-year-old woman with isolated immunoglobulin G4-related disorder affecting her lacrimal glands. Pre-treatment ^{18}F-fluorodeoxyglucose-positron emission tomography/computed tomography (^{18}F-FDG PET/CT) showed diffuse enlargement and increased FDG uptake in both lacrimal glands. After immunosuppressive treatment, ^{18}F-FDG PET/CT showed no significant FDG uptake, and the sizes of both glands returned to normal.

Keywords: Lacrimal, IgG4, FDG, PET, treatment

Öz

Elli yedi yaşında, izole lakrimal immünoglobulin G4 ilişkili hastalık tanısı almış bir kadın olgusu sunuyoruz. Tedavi öncesi yapılan, ^{18}F-florodeoksiglukoz pozitron emisyon tomografisi/bilgisayarlı tomografi (^{18}F-FDG PET/BT), her iki lakrimal bezde de yaygın boyut artışı ve FDG tutulumu göstermiştir. İmmünosüpresif tedavi sonrası yapılan ^{18}F-FDG PET/BT'de anlamlı bir FDG tutulumu izlenmemiş olup her iki bezin boyutları normale dönmüştür.

Anahtar Kelimeler: Lakrimal, IgG4, FDG, PET, tedavi

Address for Correspondence: Ali Kibar, İstanbul University-Cerrahpaşa, Cerrahpaşa Faculty of Medicine, Department of Nuclear Medicine, İstanbul, Türkiye
E-mail: alikibar01@gmail.com **ORCID ID:** orcid.org/0000-0003-0073-2343

Received: 18.02.2025 **Accepted:** 26.10.2025 **Epub:** 26.11.2025 **Publication Date:** 04.06.2026

Cite this article as: Kibar A, Asa S, Şahin OE, Uslu-Beşli L, Sağer S, Sönmezoğlu K, Sayman HB. Complete treatment response of isolated lacrimal IgG4-related disease on ^{18}F-FDG PET/CT imaging. Mol Imaging Radionucl Ther. 2026;35(2):117-119.

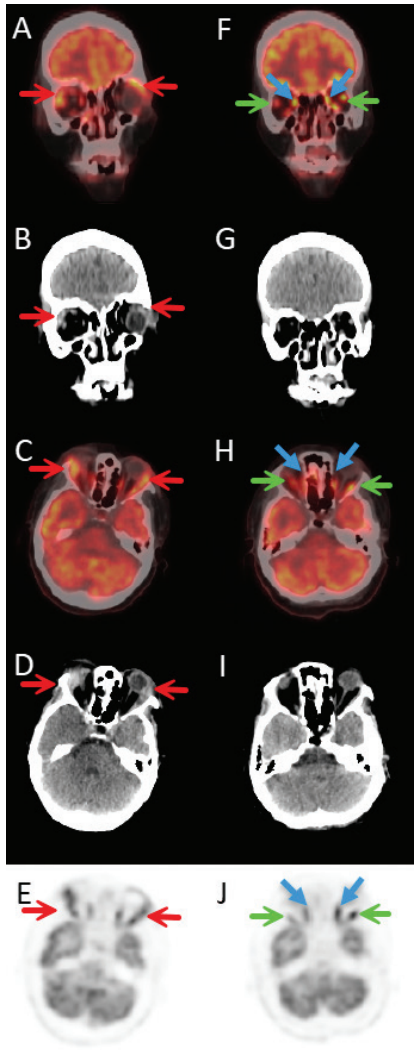

Figure 1. Immunoglobulin G4-related disease (IgG4-RD) is an immune-mediated, chronic inflammatory disorder that can affect multiple organ systems (1,2). The pathogenesis involves lymphocytic infiltration of tissues with subsequent secretion of IgG4 (3). The most commonly affected sites include the orbits, lacrimal and salivary glands, pancreas, lungs, biliary ducts, kidneys, aorta, and retroperitoneum (4,5,6). Due to its varied presentation, IgG4-RD can be mistaken for malignancy, infection, or other autoimmune diseases, necessitating a comprehensive evaluation encompassing clinical, radiological, and pathological data for accurate diagnosis (6).

^{18}F-fluorodeoxyglucose-positron emission tomography/computed tomography (^{18}F-FDG PET/CT) is a valuable imaging modality for identifying increased metabolic activity in affected organs, guiding biopsy sites, and assessing therapeutic response (7,8,9). Various studies have demonstrated the utility of ^{18}F-FDG PET/CT in evaluating treatment response in IgG4-RD (8,9,10,11). Rare manifestations, such as IgG4-related sclerosing mesenteritis and sacroiliac involvement, have also been documented in the literature (12,13). ^{18}F-FDG PET/CT is particularly beneficial in identifying the extent of multiorgan involvement.

We report a case of IgG4-RD diagnosed by lacrimal gland biopsy. The patient presented with eyelid swelling and elevated inflammatory markers. ^{18}F-FDG PET/CT was performed to assess systemic involvement, revealing increased FDG uptake and enlargement of both lacrimal glands, more pronounced on the right, without evidence of involvement of other organs.

The patient underwent corticosteroid and rituximab therapy. A follow-up ^{18}F-FDG PET/CT conducted six months post-treatment demonstrated normalization of the lacrimal gland size and the absence of FDG uptake, indicating a favorable therapeutic response. To our knowledge, this is the first ^{18}F-FDG PET/CT image of isolated lacrimal IgG4-RD demonstrating its complete response to treatment.

This case underscores the significance of ^{18}F-FDG PET/CT in evaluating treatment response in IgG4-RD. Pre-treatment coronal fusion (A), coronal CT (B), axial fusion (C), axial CT (D), and axial PET (E) images demonstrate increased size and FDG uptake in the bilateral lacrimal glands, more prominent on the right (red arrows). Post-treatment coronal fusion (F), coronal CT (G), axial fusion (H), axial CT (I), and axial PET (J) images show normalization of lacrimal gland size and absence of pathological FDG uptake. Physiological uptake in lateral rectus (green arrows) and medial rectus (blue arrows) muscles can also be seen.

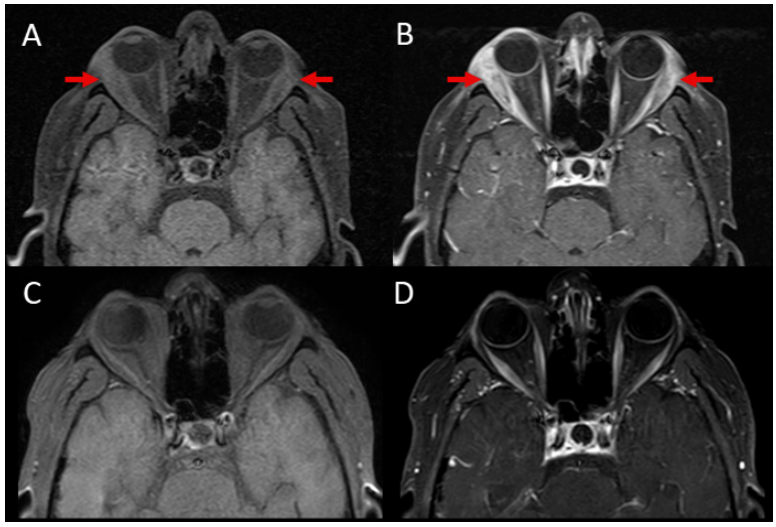

Figure 2. On pre-treatment magnetic resonance images, T1-weighted non-contrast images (A) demonstrated enlargement of both lacrimal glands (red arrows), while contrast-enhanced images (B) revealed contrast enhancement of the lacrimal glands. On the post-treatment T1-weighted images (non-contrast, C; contrast-enhanced, D), regression was observed.

Ethics

Informed Consent: Informed consent was obtained from the patient for the use of their imaging data.

Footnotes

Authorship Contributions

Surgical and Medical Practices: A.K., S.A., Concept: A.K., S.A., O.E.Ş., L.U.B., S.S., K.S., H.B.S., Design: A.K., S.A., Data Collection or Processing: A.K., S.A., Analysis or Interpretation: A.K., S.A., O.E.Ş., L.U.B., S.S., K.S., H.B.S., Literature Search: A.K., Writing: A.K.

Conflict of Interest: No conflicts of interest were declared by the authors.

Financial Disclosure: The authors declare that this study has received no financial support.

References

1. Ren H, Mori N, Sato S, Mugikura S, Masamune A, Takase K. American College of Rheumatology and the European League Against Rheumatism classification criteria for IgG4-related disease: an update for radiologists. Jpn J Radiol. 2022;40:876-893.
2. Hao FY, Yang FX, Bian HY, Zhao X. Immunoglobulin G4-related lymph node disease with an orbital mass mimicking castleman disease: a case report. World J Clin Cases. 2021;9:10999-11006.
3. Perugino CA, Stone JH. IgG4-related disease: an update on pathophysiology and implications for clinical care. Nat Rev Rheumatol. 2020;16:702-714.
4. Sekiguchi H, Horie R, Kanai M, Suzuki R, Yi ES, Ryu JH. IgG4-related disease: retrospective analysis of one hundred sixty-six patients. Arthritis Rheumatol. 2016;68:2290-2299.
5. Kuroda N, Nao T, Fukuhara H, Karashima T, Inoue K, Taniguchi Y, Takeuchi M, Zen Y, Sato Y, Notohara K, Yoshino T. IgG4-related renal disease: clinical and pathological characteristics. Int J Clin Exp Pathol. 2014;7:6379-6385.
6. Wallace ZS, Naden RP, Chari S, Choi H, Della-Torre E, Dicaire JF, Hart PA, Inoue D, Kawano M, Khosroshahi A, Kubota K, Lanzillotta M, Okazaki K, Perugino CA, Sharma A, Saeki T, Sekiguchi H, Schleinitz N, Stone JR, Takahashi N, Umehara H, Webster G, Zen Y, Stone JH; American College of Rheumatology/European League Against Rheumatism IgG4-Related Disease Classification Criteria Working Group. The 2019 American College of Rheumatology/European League Against Rheumatism classification criteria for IgG4-related disease. Arthritis Rheumatol. 2020;72:7-19.
7. Tang CYL, Chua WM, Cheng LTJ, Fong W, Zaheer S, Lam WW. ^{18}F-FDG PET/CT manifestations of IgG4-related disease. Br J Radiol. 2021;94:20210105.
8. Zhang J, Chen H, Ma Y, Xiao Y, Niu N, Lin W, Wang X, Liang Z, Zhang F, Li F, Zhang W, Zhu Z. Characterizing IgG4-related disease with ^{18}F-FDG PET/CT: a prospective cohort study. Eur J Nucl Med Mol Imaging. 2014;41:1624-1634.
9. Bai Z, Zhou T, Yu Z, Chen Y, Dong L. Clinical value of ^{18}F-FDG PET/CT in IgG4-related disease. Ann Nucl Med. 2022;36:651-660.
10. Mitamura K, Arai-Okuda H, Yamamoto Y, Norikane T, Takami Y, Fujimoto K, Wakiya R, Ozaki H, Dobashi H, Nishiyama Y. Disease activity and response to therapy monitored by [^{18}F]FDG PET/CT using volume-based indices in IgG4-related disease. EJNMMI Res. 2020;10:153.
11. Ebbo M, Grados A, Guedj E, Gobert D, Colavolpe C, Zaidan M, Masseau A, Bernard F, Berthelot JM, Morel N, Lifermann F, Palat S, Haroche J, Mariette X, Godeau B, Bernit E, Costedoat-Chalumeau N, Papo T, Hamidou M, Harlé JR, Schleinitz N. Usefulness of 2-[^{18}F]-fluoro-2-deoxy-D-glucose-positron emission tomography/computed tomography for staging and evaluation of treatment response in IgG4-related disease: a retrospective multicenter study. Arthritis Care Res (Hoboken). 2014;66:86-96.
12. Fu Z, Chen G, Liu M, Li Z, Li Q. ^{18}F-FDG PET/CT findings in a patient with IgG4-related sclerosing mesenteritis. Clin Nucl Med. 2018;43:294-295.
13. Elsobky S, Dattani V, Wagner T, Mandumula S, Tavare A. FDG PET/CT in sacroiliac IgG4 disease. Clin Nucl Med. 2021;46:e548-e550.

Interesting Image

Mol Imaging Radionucl Ther 2026;35(2):120-122 ***DOI:****10.4274/mirt.galenos.2025.98475*

^{68}Ga-PSMA PET/CT Detects a Rare Case of Breast Metastasis from Prostate Cancer

^{68}Ga-PSMA PET/BT ile Prostat Kanserinden Kaynaklanan Nadir Bir Meme Metastazının Tespiti

Georgi Gaydarov[1], Petya Nikolova[1], Mihaela Ilcheva[1], Nikolay Halachev[2], Valeria Hadzhiyska[1]

[1]*Alexandrovska University Hospital, Clinic of Nuclear Medicine, Sofia, Bulgaria*
[2]*Medical Institute of the Ministry of Interior, Clinic of Urology, Sofia, Bulgaria*

Abstract

Positron emission tomography/computed tomography (PET/CT) with Galium-68 prostate-specific membrane antigen (^{68}Ga-PSMA) PET/CT) is a valuable tool for initial staging, recurrence detection, and assessment of treatment response in men with prostate cancer. Metastatic spread to regional and distant lymph nodes, bone, lung and liver is well known and expected in patients with castration-resistant disease. However, the application of a highly sensitive whole-body imaging modality such as ^{68}Ga-PSMA PET/CT can reveal metastatic foci in rare or unusual locations. We present the case of an 82-year-old patient with prostate adenocarcinoma who underwent long-term androgen deprivation therapy. A ^{68}Ga-PSMA PET/CT scan was performed in June 2021 due to significant prostate-specific antigen elevation and revealed disease progression with widespread regional and distant metastases, including a soft-tissue mass in the right breast that demonstrated intense radiotracer uptake; this mass was subsequently resected and histologically confirmed. This case underscores the excellent diagnostic performance of ^{68}Ga-PSMA PET/CT for atypical metastatic sites.

Keywords: Prostate cancer, breast metastasis, ^{68}Ga-PSMA PET/CT

Öz

Gallium-68 prostat spesifik membran antijeni pozitron emisyon tomografisi/bilgisayarlı tomografi (^{68}Ga-PSMA PET/BT), prostat kanseri olan erkeklerde başlangıç evrelemesi, nüks tespiti ve tedavi yanıtının değerlendirilmesi için değerli bir araçtır. Bölgesel ve uzak lenf düğümlerine, kemiğe, akciğere ve karaciğere metastatik yayılım, kastrasyona dirençli hastalığı olan hastalarda iyi bilinen ve beklenen bir durumdur. Bununla birlikte, ^{68}Ga-PSMA PET/BT gibi yüksek hassasiyetli bir tüm vücut görüntüleme yönteminin uygulanması, nadir ve alışılmadık lokalizasyona sahip metastatik odakları ortaya çıkarabilir. Uzun süreli androjen deprivasyon tedavisi gören 82 yaşında bir prostat adenokarsinomlu hastayı sunuyoruz. Haziran 2021'de, prostat spesifik antijen düzeyinde belirgin yükselme nedeniyle ^{68}Ga-PSMA PET/BT taraması yapıldı ve bu tarama, yaygın bölgesel ve uzak metastazlarla birlikte hastalığın ilerlediğini ortaya koydu. Sağ memede yoğun radyoaktif madde tutulumu gösteren bir yumuşak doku kitlesi tespit edildi ve bu kitle daha sonra rezeke edilerek histolojik olarak doğrulandı. Bu olgu, atipik metastaz bölgelerinde bile ^{68}Ga-PSMA PET/BT'nin mükemmel tanısal performansını vurgulamaktadır.

Anahtar Kelimeler: Prostat kanseri, meme metastazı, ^{68}Ga-PSMA PET/BT

Address for Correspondence: Georgi Gaydarov, Alexandrovska University Hospital, Clinic of Nuclear Medicine, Sofia, Bulgaria
E-mail: gaydarov17@gmail.com **ORCID ID:** orcid.org/0009-0008-2223-3231
Received: 29.06.2025 **Accepted:** 11.11.2025 **Epub:** 08.01.2026 **Publication Date:** 04.06.2026

Cite this article as: Gaydarov G, Nikolova P, Ilcheva M, Halachev N, Hadzhiyska V. ^{68}Ga-PSMA PET/CT detects a rare case of breast metastasis from prostate cancer. Mol Imaging Radionucl Ther. 2026;35(2):120-122.

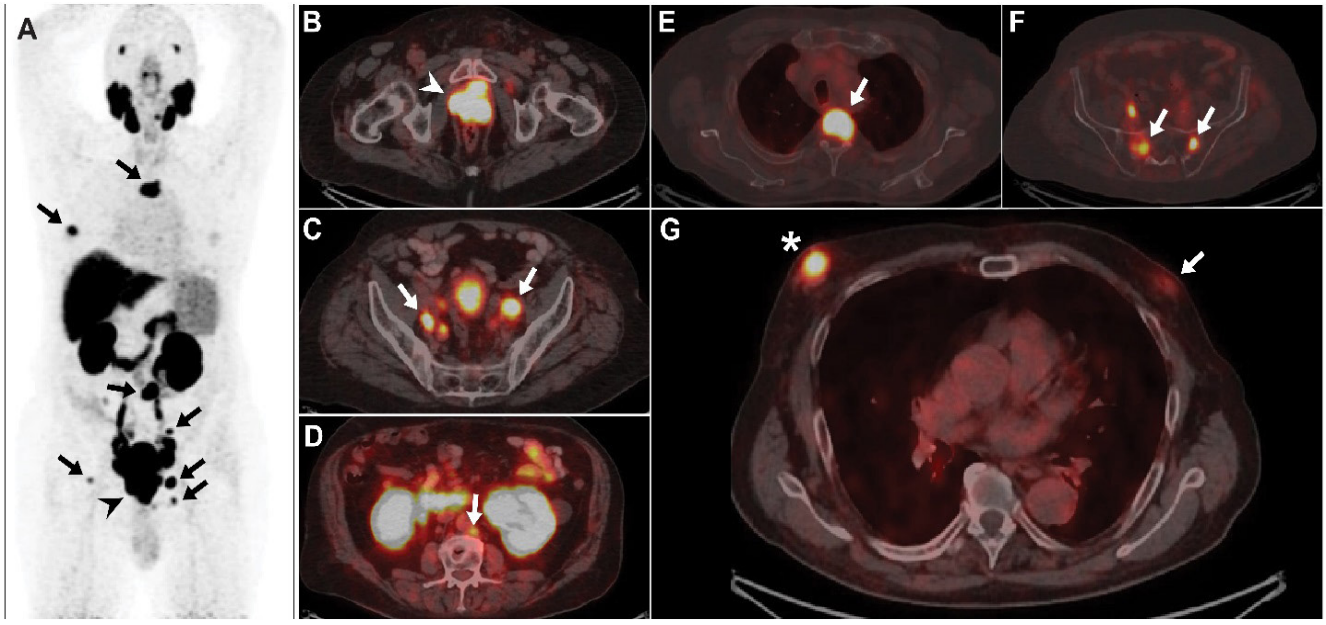

Figure 1. An 82-year-old patient, who had been diagnosed with high-grade prostate adenocarcinoma in November 2014 (then aged 75) with a Gleason score of 8 (4+4) and a pre-biopsy serum prostate-specific antigen (PSA) concentration of 135 µg/L, was admitted to our department for further evaluation. Initial staging with bone scintigraphy and abdominopelvic computed tomography (CT) revealed locally advanced disease, without evidence of regional or distant dissemination. The patient underwent long-term androgen deprivation therapy until June 2021, when he was referred for restaging with Galium-68 prostate-specific membrane antigen (^{68}Ga-PSMA) positron emission tomography (PET)/CT because of a significant PSA elevation (182 µg/L). Prior to the scan, the patient reported a painful right breast lump that he had noticed one month earlier. The scan was performed after obtaining a written consent and in accordance with the standard protocol, 60 min after intravenous administration of 4.5 mCi ^{68}Ga-PSMA-11 (1). Maximum-intensity projection images demonstrated intense PSMA uptake in the prostate gland (A, arrowhead) and in multiple metastatic sites (A, arrows). Fused images revealed an enlarged prostate with lobulated margins and intense PSMA uptake throughout the gland (B, arrowhead). Multiple PSMA-avid parailiac and paraaortic lymph nodes (C and D; arrows) and several bone lesions (E and F; arrows) were identified. Remarkably, there was evidence of a focal soft-tissue lesion in the right breast with intense uptake, measuring 23 × 20 mm in axial diameter (G, asterisk). Increased subareolar glandular tissue with faint activity was also noted in the contralateral left breast (G; arrow). Following the PET/CT, the patient was referred for further evaluation with mammography, which demonstrated benign gynecomastia in the left breast and a lesion with malignant characteristics in the right breast. To definitively exclude a primary breast tumor, the patient was referred for surgical excision of the lesion. Histopathological examination and immunohistochemistry confirmed the presence of breast metastasis from prostate carcinoma. Breast metastases from prostate cancer are uncommon, with only a few cases reported in the literature (2). Long-term hormonal treatment is considered a predisposing factor, often causing gynecomastia and increased breast vascularity, which facilitate hematogenous metastatic spread (3). Kumar Chauhan et al. (4) report a similar case of a patient with metastatic castration-resistant prostate cancer (after surgical castration and anti-androgen therapy) who had a metastasis in the left breast that was also PSMA-positive, considerably larger, and even infiltrated the adjacent chest wall. Previous studies have shown that increased PSMA expression can also occur in benign changes associated with gynecomastia, which may be unilateral or asymmetric (5,6). Synchronous breast cancer should also be considered, given the increased expression of PSMA in the tumor-associated neovasculature of various non-prostatic malignancies. Polverari et al. (7) described a PSMA-avid breast lesion detected on restaging PET/CT that was confirmed histologically as primary male breast cancer. In contrast, their patient presented with an isolated locoregional recurrence after radical prostatectomy (a PSMA-positive para-iliac lymph node) rather than widespread metastatic prostate cancer and had no prior anti-androgen therapy. Our report underscores the excellent diagnostic performance of ^{68}Ga-PSMA PET/CT for the detection of unusual metastatic sites and emphasizes potential pitfalls in the interpretation of such findings.

Ethics

Informed Consent: Informed consent was obtained from the patient for the publication of his anonymized images and relevant clinical information.

Footnotes

Authorship Contributions

Concept: G.G., Design: N.H., V.H., Data Collection or Processing: M.I., N.H., Analysis or Interpretation: P.N., M.I., V.H., Literature Search: P.N., M.I., Writing: G.G.

Conflict of Interest: No conflicts of interest were declared by the authors.

Financial Disclosure: The authors declare that this study has received no financial support.

References

1. Fendler WP, Eiber M, Beheshti M, Bomanji J, Calais J, Ceci F, Cho SY, Fanti S, Giesel FL, Goffin K, Haberkorn U, Jacene H, Koo PJ, Kopka K, Krause BJ, Lindenberg L, Marcus C, Mottaghy FM, Oprea-Lager DE, Osborne JR, Piert M, Rowe SP, Schöder H, Wan S, Wester HJ, Hope TA, Herrmann K. PSMA PET/CT: joint EANM procedure guideline/SNMMI procedure standard for prostate cancer imaging 2.0. Eur J Nucl Med Mol Imaging. 2023;50:1466-1486.
2. Zhang S, Peng W, Cheng L, Pei B, Zhou X, Wang M, Jiang L, Lu C, Xu L. Metastasis of prostate cancer to breast: A case report. Front Oncol. 2025;15:1580441.
3. Lima V, Martinez-Lapus FG, Demegillo KJ. Breast metastasis from castrate-resistant prostatic adenocarcinoma mimicking as a second primary: a case report. World J Oncol. 2020;11:37-40.
4. Kumar Chauhan P, Jain M, Adiga P, Shivalingaiah M. Breast lump: an uncommon metastasis of prostate cancer. archives of Clinical and Medical Case Reports. 2020;4:624-628.
5. Sasikumar A, Joy A, Nair BP, Pillai MRA, Madhavan J. False positive uptake in bilateral gynecomastia on ^{68}Ga-PSMA PET/CT scan. Clin Nucl Med. 2017;42:e412-e414.
6. Metwalley KA, Farghaly HS. Gynecomastia in adolescent males: current understanding of its etiology, pathophysiology, diagnosis, and treatment. Ann Pediatr Endocrinol Metab. 2024;29:75-81.
7. Polverari G, Ceci F, Calderoni L, Cervati V, Farolfi A, Castellucci P, Fanti S. Male breast cancer detected by ^{68}Ga-PSMA-11 PET/CT in a patient with prostate cancer with pelvic lymph node metastasis. Clin Genitourin Cancer. 2019;17:154-156.

Interesting Image

Mol Imaging Radionucl Ther 2026;35(2):123-126 ***DOI:****10.4274/mirt.galenos.2025.43925*

Extrapulmonary Tuberculosis Mimicking Malignancy

Maligniteyi Taklit Eden Ekstrapulmoner Tüberküloz

Cansu Güneren, Rabia Lebriz Uslu Beşli, Haluk Burçak Sayman

İstanbul University-Cerrahpaşa Cerrahpaşa Faculty of Medicine, Department of Nuclear Medicine, İstanbul, Türkiye

Abstract

Tuberculosis (TB) remains a significant public health problem in developing countries, but its diagnosis can be challenging as it may mimic malignancy or other granulomatous diseases. Although pulmonary TB is the most common form, TB can spread hematogenously, lymphatically, or by direct extension to any tissue or organ. We report a 62-year-old female who underwent ^{18}F-fluorodeoxyglucose positron emission tomography/computed tomography (^{18}F-FDG PET/CT) for malignancy evaluation, was diagnosed with extrapulmonary TB, and had her treatment response assessed with ^{18}F-FDG PET/CT.

Keywords: Tuberculosis, malignancy, FDG PET, extrapulmonary, PET/CT

Öz

Tüberküloz (TB), gelişmekte olan ülkelerde önemli bir sağlık sorunu olmaya devam etmektedir. Ancak malignite veya diğer granülomatöz hastalıklarla karışabileceğinden tanısı güçleşebilmektedir. Pulmoner TB hastalığın en yaygın formu olmasına rağmen, TB hematolojik, lenfatik yolla veya komşuluk yoluyla herhangi bir doku veya organa yayılabilir. Bu olgu sunumunda malignite şüphesiyle ^{18}F-florodeoksiglukoz pozitron emisyon tomografisi/bilgisayarlı tomografi (^{18}F-FDG PET/BT) görüntülemesi yapılan, ekstrapulmoner TB tanısı alan ve ^{18}F-FDG PET/BT ile tedavi yanıtı değerlendirilen 62 yaşında kadın hasta bildirilmiştir.

Anahtar Kelimeler: Tüberküloz, malignite, FDG PET, extrapulmoner, PET/BT

Address for Correspondence: Cansu Güneren, İstanbul University-Cerrahpaşa Cerrahpaşa Faculty of Medicine, Department of Nuclear Medicine, İstanbul, Türkiye

E-mail: cansu.guneren@iuc.edu.tr **ORCID ID:** orcid.org/0009-0006-6766-2166

Received: 25.09.2025 **Accepted:** 23.11.2025 **Epub:** 19.12.2025 **Publication Date:** 04.06.2026

Cite this article as: Güneren C, Uslu Beşli RL, Sayman HB. Extrapulmonary tuberculosis mimicking malignancy. Mol Imaging Radionucl Ther. 2026;35(2):123-126.

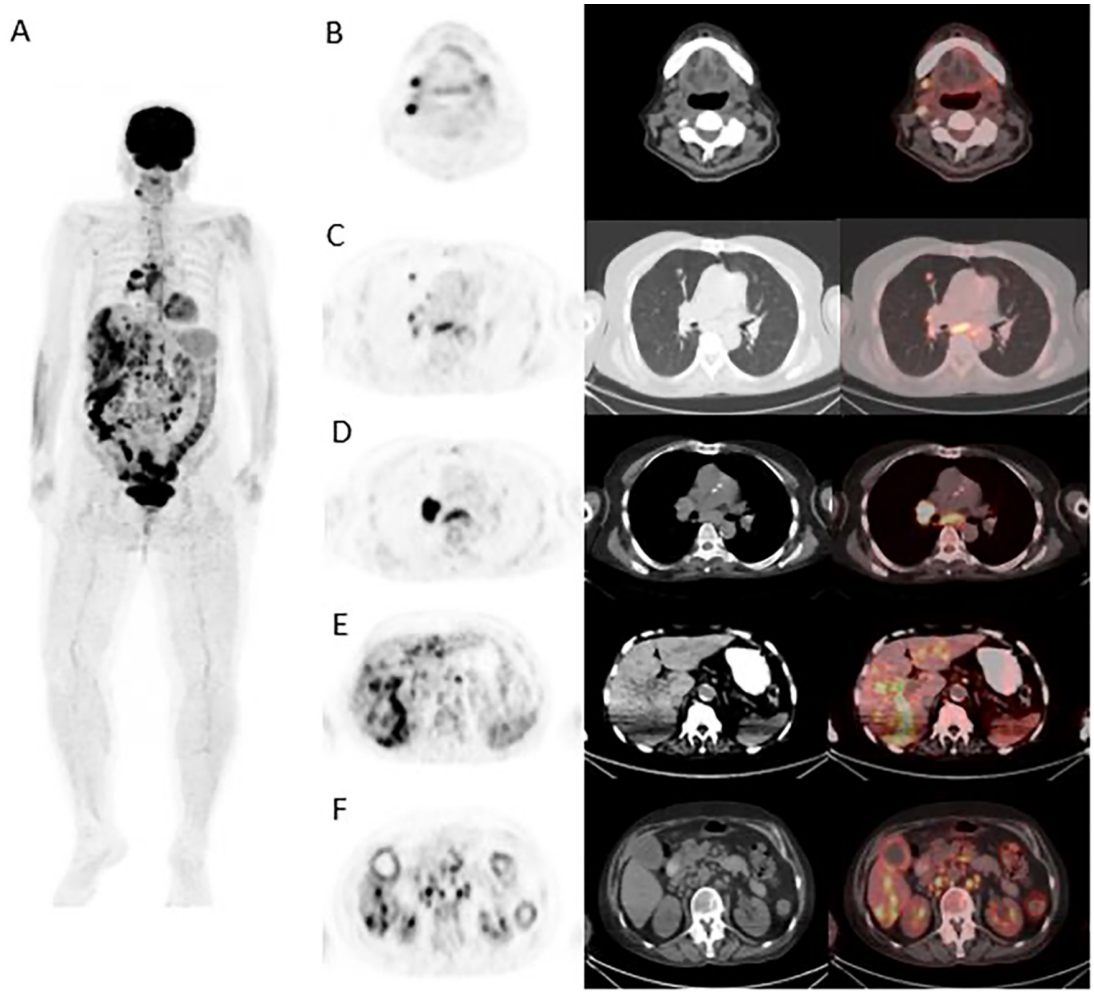

Figure 1. A 62-year-old female patient presenting with newly onset fatigue, weakness, night sweats, and weight loss underwent an ^{18}F-fluorodeoxyglucose positron emission tomography/computed tomography (PET/CT) scan for malignancy screening. Maximum intensity projection image (A), together with transaxial PET, CT, and PET/CT fusion images, demonstrated multiple intensely hypermetabolic lymph nodes in supra- and infradiaphragmatic lymphatic stations (B, D, F); hypermetabolic nodular lesions in the parenchyma of both lungs (C); hypermetabolic hypodense lesions in both lobes of the liver (E); and diffuse hypermetabolism in the spleen and segments of the colon (E, F). Excisional biopsy of a cervical lymph node demonstrated tuberculous lymphadenitis, while colonoscopy revealed a granulomatous appearance consistent with tuberculosis. Biopsy of the hypermetabolic liver lesions showed no evidence of malignancy.

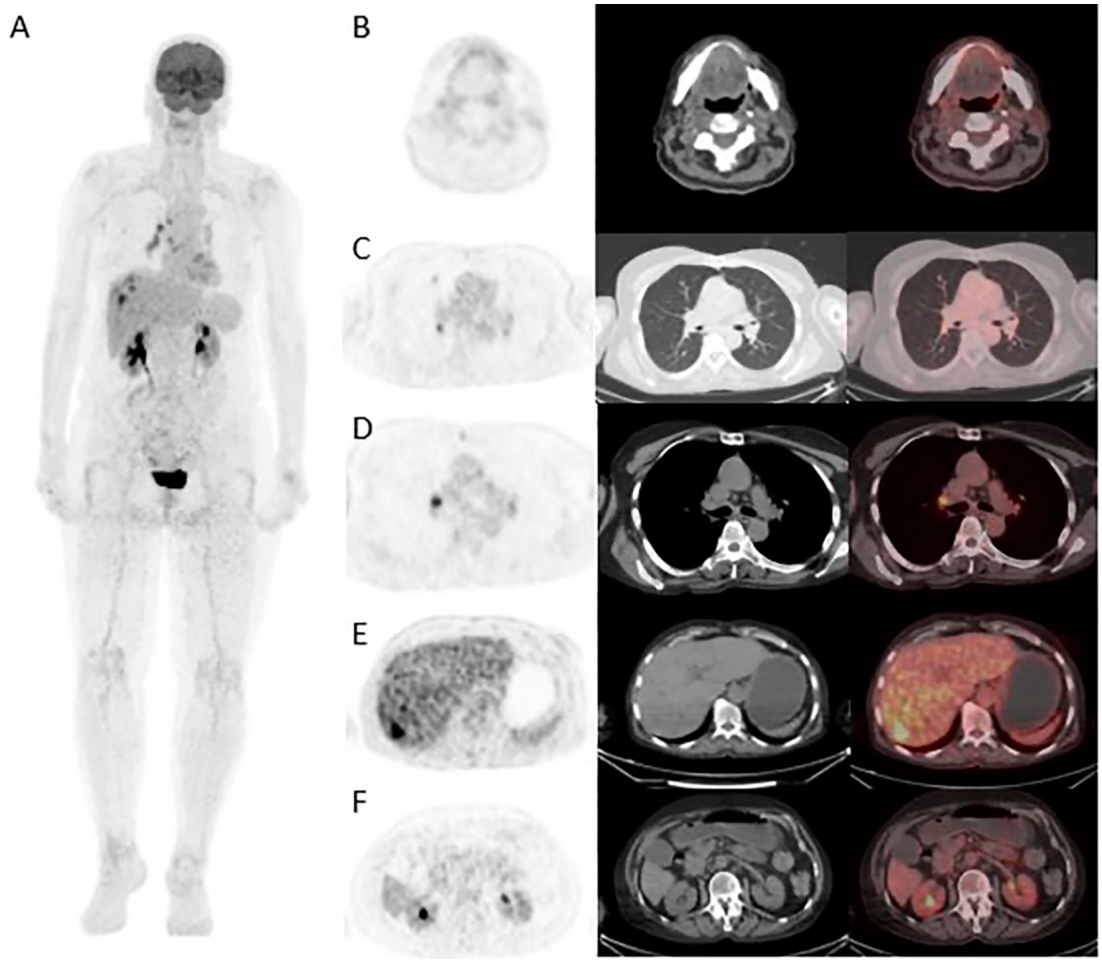

Figure 2 (A-F). Standard quadruple anti-tuberculosis (TB) therapy was initiated for the patient. After treatment, a partial response was observed in the hypermetabolic lesions in the liver and mediastinum identified on the pretreatment ^{18}F-fluorodeoxyglucose positron emission tomography/computed tomography (^{18}F-FDG PET/CT), while a complete response was observed in the remaining lesions.

Although pulmonary TB is the most common form of the disease, TB can spread hematogenously, lymphatically, or by direct extension to virtually any tissue or organ. Hepatobiliary TB is a rare extrapulmonary manifestation that can mimic malignancy and may lead to diagnostic delays due to its nonspecific symptoms. TB should be considered in the differential diagnosis of patients, particularly immunocompromised individuals, presenting with multiple hypermetabolic hepatic lesions (1,2). ^{18}F-FDG PET/CT is a valuable modality for detecting tuberculous lymphadenitis and serves as a complementary tool in the diagnosis of extrapulmonary TB. Owing to the intense FDG uptake by tuberculous granulomas, it is highly effective in identifying tuberculous lymphadenitis. Additionally, maximum standard uptake values provides information on the degree of inflammatory activity even in the absence of bacteriological confirmation. ^{18}F-FDG PET/CT can detect lesions that may be overlooked on morphological imaging, assist in selecting optimal biopsy sites, and differentiate active from inactive disease by evaluating early treatment response. However, ^{18}F-FDG PET/CT cannot reliably distinguish tuberculous lymphadenitis from lymphoma, sarcoidosis, or metastatic lymphadenopathy. In countries where TB is endemic, tuberculous lymphadenitis should be considered in the differential diagnosis of patients with enlarged lymph nodes, and lymph node biopsy plays a crucial role in establishing the diagnosis in light of ^{18}F-FDG PET/CT findings (3-5).

Ethics

Informed Consent: Informed consent was obtained from the patient for publication.

Footnotes

Authorship Contributions

Concept: R.L.U.B., H.B.S., Design: R.L.U.B., H.B.S., Data Collection or Processing: C.G., Literature Search: C.G., Writing: C.G., R.L.U.B., H.B.S.

Conflict of Interest: No conflicts of interest were declared by the authors.

Financial Disclosure: The authors declare that this study has received no financial support.

References

1. Wang X, Shi X, Yi C, Chen Z, Zhang B, Zhang X. Hepatic tuberculosis mimics metastasis revealed by ^{18}F-FDG PET/CT. Clin Nucl Med. 2014;39:e325-e327.
2. Di Renzo C, Tabrizian P, Kozuch DE, Fiel MI, Schwartz ME. Abdominal tuberculosis mimicking cancer clinically and on fluorodeoxyglucose (FDG)-positron emission tomography (PET) imaging: a two-case series. Am J Case Rep. 2020;21:e918901.
3. Liao F, Huang Z, Xu R, Luo Z, Qi W, Fan B, Yu J. Analysis of misdiagnosis and ^{18}F-FDG PET/CT findings of lymph node tuberculosis. J Xray Sci Technol. 2022;30:941-951.
4. Yu WY, Lu PX, Assadi M, Huang XL, Skrahin A, Rosenthal A, Gabrielian A, Tartakovsky M, Wáng YXJ. Updates on ^{18}F-FDG-PET/CT as a clinical tool for tuberculosis evaluation and therapeutic monitoring. Quant Imaging Med Surg. 2019;9:1132-1146.
5. Sathekge M, Maes A, D'Asseler Y, Vorster M, Gongxeka H, Van de Wiele C. Tuberculous lymphadenitis: FDG PET and CT findings in responsive and nonresponsive disease. Eur J Nucl Med Mol Imaging. 2012;39:1184-1190.

Interesting Image

Mol Imaging Radionucl Ther 2026;35(2):127-130 ***DOI:****10.4274/mirt.galenos.2025.13540*

Hydatic Cyst Infection of the Tibia Mimicking Chondrosarcoma on ^{18}F-FDG PET/CT Scan

^{18}F-FDG PET/BT Taramasında Kondrosarkomu Taklit Eden Tibial Kist Hidatik Enfeksiyonu

Furkan Avcı[1], Batuhan Kocabeyoğlu[1], İpek Tamsel[2], Hüseyin Kaya[3], Başak Doğanavşargil[4], Zehra Özcan[1]

[1]*Ege University Faculty of Medicine, Department of Nuclear Medicine, İzmir, Türkiye*
[2]*Ege University Faculty of Medicine, Department of Radiology, İzmir, Türkiye*
[3]*Ege University Faculty of Medicine, Department of Orthopedics, İzmir, Türkiye*
[4]*Ege University Faculty of Medicine, Department of Pathology, İzmir, Türkiye*

Abstract

A hydatid cyst is a zoonotic infection caused by *Echinococcus granulosus*. The liver and lungs are the most affected organs. Although rare, osseous involvement by hydatid cyst disease can occur because the rigid bone trabeculae prevent formation of the characteristic adventitia. While fluorodeoxyglucose (FDG) positron emission tomography (PET) findings in hepatic and pulmonary hydatid cysts are well described, this case, to the best of our knowledge, represents the first report of bone hydatid disease located in an extremity evaluated by ^{18}F-FDG PET/computed tomography.

Keywords: Hytadic cyst, bone diseases, infection, ^{18}F-FDG PET/CT

Öz

Hidatik kist, *Echinococcus granulosus* tarafından oluşturulan zoonotik bir enfeksiyondur ve en sık karaciğer ile akciğerleri tutar. Nadir olmakla birlikte, kemik trabeküllerinin sert yapısı karakteristik adventisya oluşumunu engellediğinden, hidatik kist hastalığı kemik dokusunu da etkileyebilir. Karaciğer ve akciğer hidatik kistlerinde florodeoksiglukoz (FDG) pozitron emisyon tomografi (PET) bulguları iyi tanımlanmış olsa da, bildiğimiz kadarıyla bu olgu, ekstremite yerleşimli kemik hidatik hastalığının ^{18}F-FDG PET/bilgisayarlı tomografi ile değerlendirildiği ilk olgu olma özelliğini taşımaktadır.

Anahtar Kelimeler: Kist hidatik, kemik hastalıkları, enfeksiyon, ^{18}F-FDG PET/BT

Address for Correspondence: Furkan Avcı, Ege University Faculty of Medicine, Department of Nuclear Medicine, İzmir, Türkiye
E-mail: furkan.avci@ege.edu.tr **ORCID ID:** orcid.org/0009-0002-2392-2190
Received: 16.07.2025 **Accepted:** 25.11.2025 **Epub:** 19.12.2025 **Publication Date:** 04.06.2026

Cite this article as: Avcı F, Kocabeyoğlu B, Tamsel İ, Kaya H, Doğanavşargil B, Özcan Z. Hydatic cyst infection of the tibia mimicking chondrosarcoma on ^{18}F-FDG PET/CT scan. Mol Imaging Radionucl Ther. 2026;35(2):127-130.

Figure 1. A 54-year-old male patient presented with progressively worsening pain and swelling localized to the left knee. Initial radiological evaluation using anteroposterior X-ray imaging demonstrated extensive lytic-destructive lesions predominantly involving the proximal metaphysis of the left tibia. Radiographic features included marked trabecular disruption, cortical thinning, and expansion of the medullary cavity. Given these aggressive radiological findings, a primary bone malignancy, particularly chondrosarcoma, was considered a preliminary diagnosis.

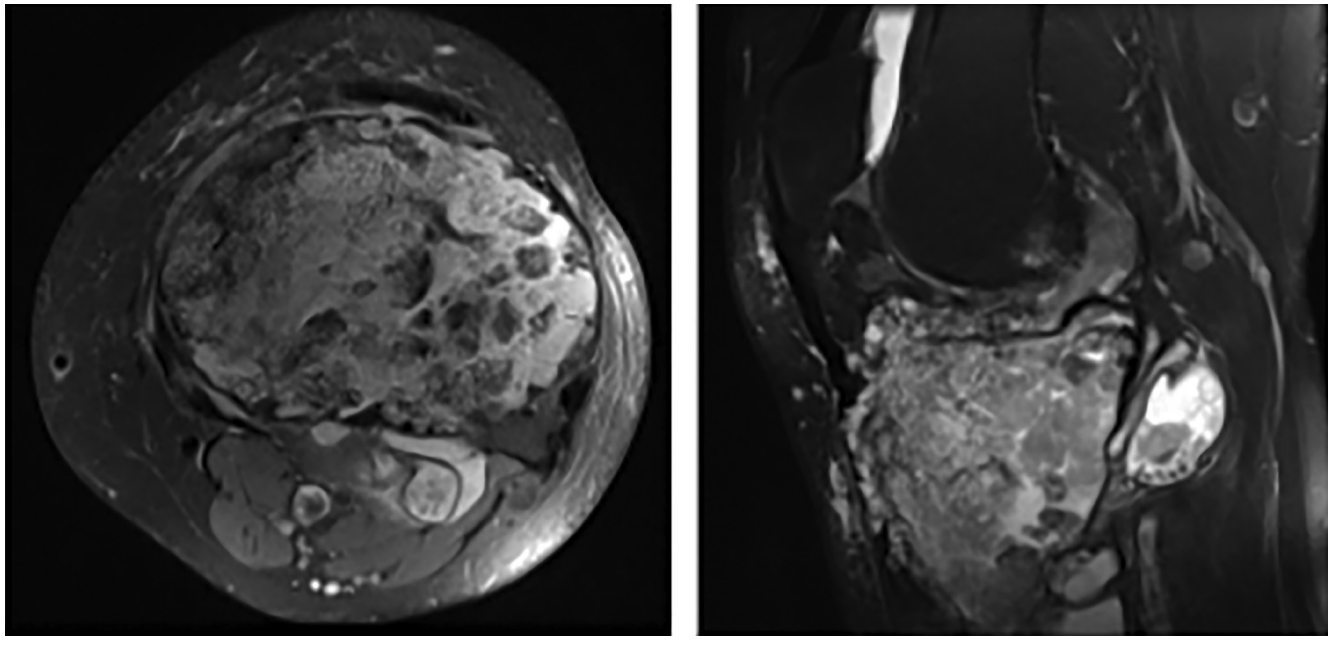

Figure 2. Subsequent magnetic resonance imaging (MRI) was conducted to further characterize the lesion. Axial (A) and sagittal (B) T2-weighted MRI sequences revealed a large, cystic lesion localized at the epiphyseal-metaphyseal junction of the proximal tibia. The lesion exhibited characteristic internal septations, focal chondroid-like calcifications, and prominent soft-tissue infiltration extending beyond the bone marrow cavity into surrounding musculature and adipose tissue. These radiological findings strongly supported the initial clinical suspicion of chondrosarcoma, necessitating further staging investigations.

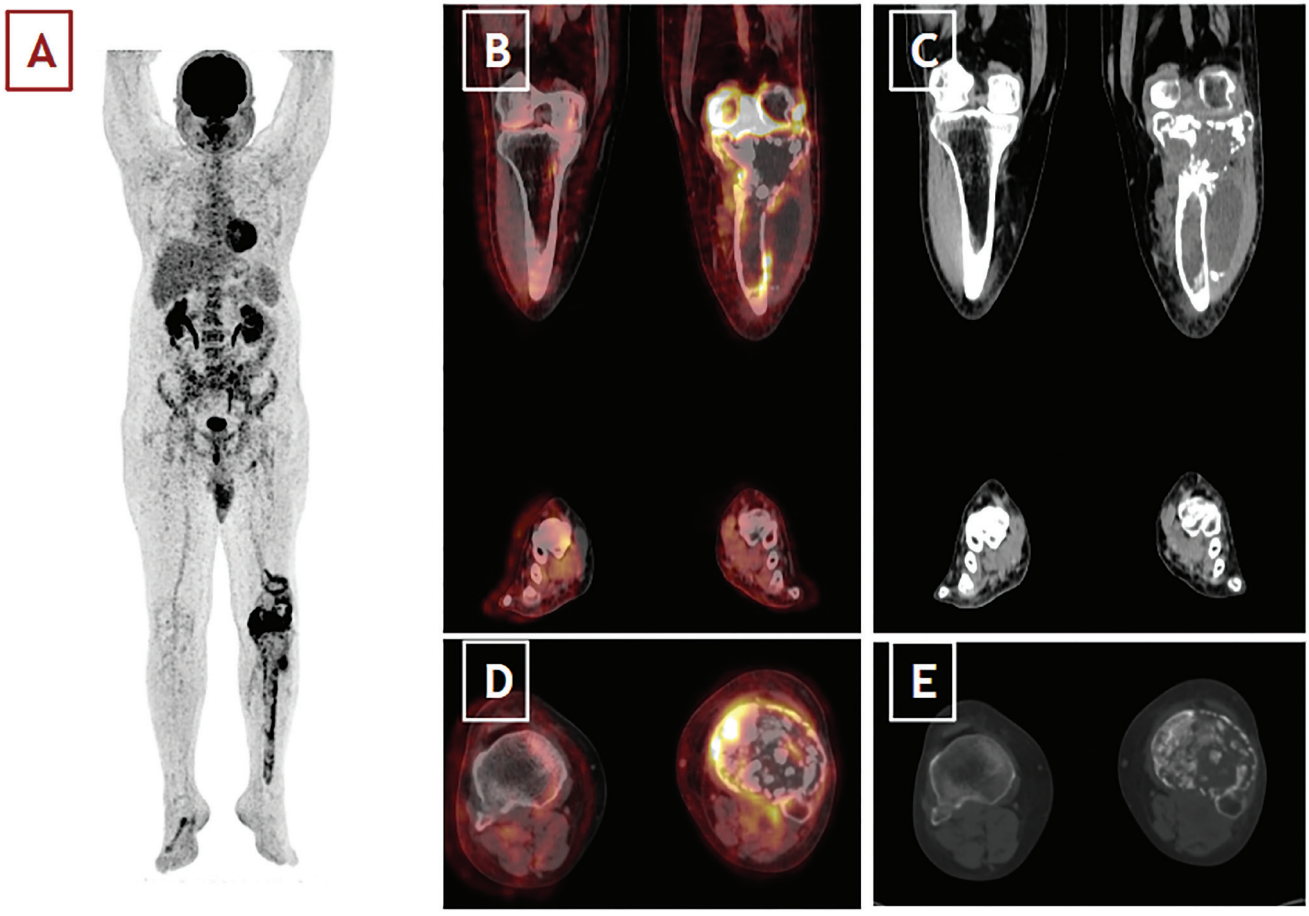

Figure 3. To assess systemic involvement and metastatic potential, an ^{18}F-fluorodeoxyglucose positron emission tomography/computed tomography (^{18}F-FDG PET/CT), scan was performed. Maximum-intensity projection imaging (A) identified intensely hypermetabolic foci (maximum standard uptake values: 27.3) in the proximal left tibia and distal femur. On coronal (B, C) and axial (D, E) fused PET/CT images, the lesions demonstrated marked cortical destruction with irregular margins and peripheral, heterogeneous FDG uptake. Within the bone marrow, cystic and lytic areas showed relatively low or absent tracer accumulation, suggestive of necrotic or fluid-filled components, whereas the surrounding soft-tissue extensions were markedly hypermetabolic and contained partially calcified densities. Mild periosteal reaction and adjacent soft-tissue edema were also evident, indicating biologic aggressiveness. Additionally, mild FDG uptake was noted in the left inguinal lymph nodes and was interpreted as reactive rather than metastatic. Because of persistent suspicion of malignancy on imaging, a tru-cut biopsy was performed. Histopathological analysis unexpectedly identified a solitary osseous hydatid cyst (caused by *Echinococcus granulosus*). No additional disease foci were detected upon further systemic evaluation with abdominal and thoracic CT imaging. The patient received antiparasitic therapy with albendazole, followed by successful surgical excision of the lesion. Although rare, hydatid cyst disease can also involve osseous structures because the rigidity of trabecular bone prevents formation of the characteristic adventitia 1-5. While FDG PET findings in hepatic 6 and pulmonary 7 hydatid cysts are well described, this case highlights the importance of considering osseous hydatid disease in the differential diagnosis of aggressive bone lesions, particularly in endemic regions.

Ethics

Informed Consent: Informed consent was obtained from the patient for publication of this case and accompanying images.

Footnotes

Authorship Contributions

Surgical and Medical Practices: H.K., B.D., Design: B.K., Data Collection or Processing: F.A., İ.T., Analysis or Interpretation: İ.T., Literature Search: F.A., Z.Ö., Writing: F.A., Z.Ö.

Conflict of Interest: No conflicts of interest were declared by the authors.

Financial Disclosure: The authors declare that this study has received no financial support.

References

1. Takenaka J, Hirata K, Watanabe S, Takahata M, Kudo K. Bone echinococcosis mimicking malignancy on FDG PET. Clin Nucl Med. 2023;48:e523-e525. Epub 2023 Sep 18.
2. Arkun R, Mete BD. Musculoskeletal hydatid disease. Semin Musculoskelet Radiol. 2011;15:527-540. Epub 2011 Nov 11.
3. Jamshidi K, Zandrahimi F, Haji Agha Bozorgi M, Mirkamali SF, Esmaeli Dahaj A, Mirzaei A. Non-spinal hydatid disease of bone: a series of nine cases. Arch Bone Jt Surg. 2022;10:447-452.
4. Kalinova K, Proichev V, Stefanova P, Tokmakova K, Poriazova E. Hydatid bone disease: a case report and review of the literature. J Orthop Surg (Hong Kong). 2005;13:323-325.
5. Manenti G, Censi M, Pizzicannella G, Pucci N, Pitocchi F, Calcagni A, Amico A, Collura A, Ryan CP. Vertebral hydatid cyst infection. A case report. Radiol Case Rep. 2020;15:523-527.
6. Alghofaily KA, Saeedan MB, Aljohani IM, Alrasheed M, McWilliams S, Aldosary A, Neimatallah M. Hepatic hydatid disease complications: review of imaging findings and clinical implications. Abdom Radiol (NY). 2017;42:199-210.
7. Aydin Y, Ulas AB, Ahmed AG, Eroglu A. Pulmonary hydatid cyst in children and adults: diagnosis and management. Eurasian J Med. 2022;54(Suppl1):133-140.

Interesting Image

Mol Imaging Radionucl Ther 2026;35(2):131-133 **DOI:***10.4274/mirt.galenos.2025.21347*

A Rare Case of Primary Squamous Cell Urachal Carcinoma Staged with ^{18}F-FDG PET/CT

^{18}F-FDG PET/BT ile Evrelendirilmiş Nadir Bir Primer Skuamöz Hücreli Urakal Karsinom Olgusu

Yavor Gramatikov[1], Alexander Stoychev[2], Georgi Gaydarov[1], Stamen Andreev[2], Nikolay Halachev[2], Valeria Hadzhiyska[1]

[1]*University Hospital Alexandrovska, Clinic of Nuclear Medicine, Sofia, Bulgaria*
[2]*Medical Institute of the Ministry of Interior, Clinic of Urology, Sofia, Bulgaria*

Abstract

Primary squamous cell urachal carcinoma is an exceedingly rare epithelial neoplasm and an aggressive malignancy, originating from the urachal remnants. In contrast to mucinous adenocarcinoma, the most common histological type, squamous cell urachal carcinoma demonstrates high 2-deoxy-2-^{18}F-fluorodeoxyglucose (^{18}F-FDG) uptake, making ^{18}F-FDG positron emission tomography/computed tomography (PET/CT) a valuable tool for evaluating regional lymph node involvement and detecting distant metastases. Optimal surgical management, the need for systemic therapy, and the overall prognosis are largely determined by accurate clinical staging, which is mainly based on the widely recognized Sheldon and Mayo classifications. We present a rare case of primary squamous cell urachal carcinoma on ^{18}F-FDG PET/CT in a young woman, with correlation to surgical and histopathological findings.

Keywords: Rare malignancy, primary urachal carcinoma, squamous cell carcinoma, ^{18}F-FDG PET/CT

Öz

Primer skuamöz hücreli urakus karsinomu urakal kalıntılardan kaynaklanan agresif bir malignitedir. En yaygın histolojik tip olan müsinöz adenokarsinomun aksine, skuamöz hücreli urakal karsinom yüksek 2-deoksi-2-^{18}F-florodeoksiglukoz (^{18}F-FDG) tutulumu gösterir; bu da ^{18}F-FDG pozitron emisyon tomografisi/bilgisayarlı tomografi (PET/BT) bölgesel lenf düğümü tutulumunu değerlendirmek ve uzak metastazları tespit etmek için değerli bir araç haline getirir. Optimal cerrahi yönetim, sistemik tedavi ihtiyacı ve genel prognoz büyük ölçüde, esas olarak yaygın olarak kabul edilen Sheldon ve Mayo sınıflandırmalarına dayanan doğru klinik evreleme ile belirlenir. Bu çalışmada, genç bir kadında ^{18}F-FDG PET/BT ile saptanan nadir bir primer skuamöz hücreli urakal karsinom olgusunu, cerrahi ve histopatolojik bulgularla ilişkilendirerek sunuyoruz.

Anahtar Kelimeler: Nadir malignite, primer urakal karsinom, skuamöz hücreli karsinom, ^{18}F-FDG PET/BT

Address for Correspondence: Yavor Gramatikov, University Hospital Alexandrovska, Clinic of Nuclear Medicine, Sofia, Bulgaria
E-mail: yavorgramatikov@abv.bg **ORCID ID:** orcid.org/0009-0001-2901-2940
Received: 27.09.2025 **Accepted:** 26.12.2025 **Epub:** 25.03.2026 **Publication Date:** 04.06.2026

Cite this article as: Gramatikov Y, Stoychev A, Gaydarov G, Andreev S, Halachev N, Hadzhiyska V. A rare case of primary squamous cell urachal carcinoma staged with ^{18}F-FDG PET/CT. Mol Imaging Radionucl Ther. 2026;35(2):131-133.

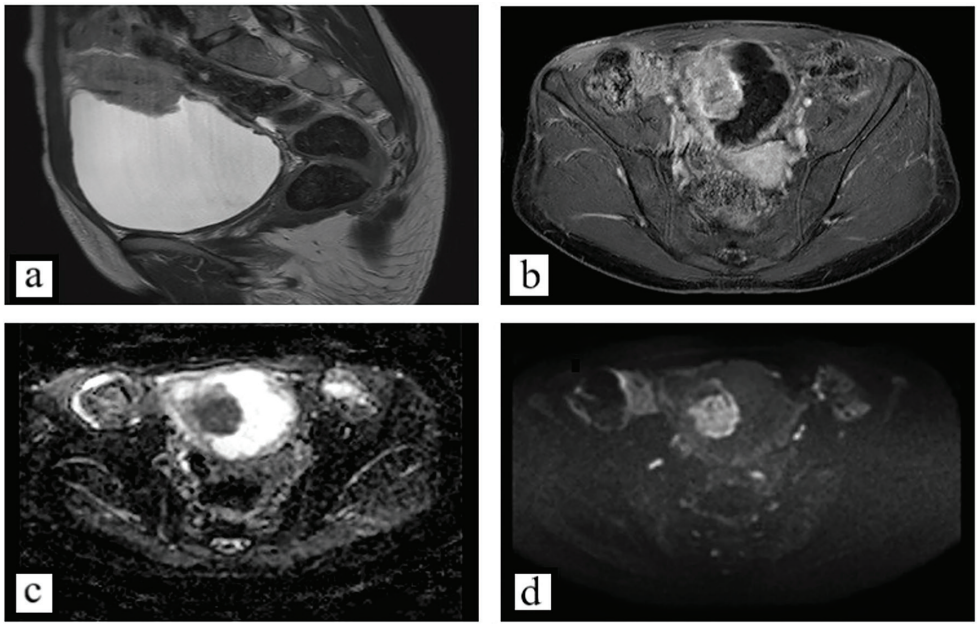

Figure 1. A 34-year-old woman presented with dysuria and recurrent urinary tract infections. Initial ultrasonography demonstrated a lesion in the bladder area. Subsequent magnetic resonance imaging (MRI) revealed a midline supravesical solid mass along the course of the urachal ligament and contiguous with the bladder dome, radiologically consistent with originating from urachal remnants. On MRI, the lesion appeared iso- to hypointense on T2-weighted sequences (Figure 1a), showed homogeneous post-gadolinium enhancement (Figure 1b), and showed restricted diffusion (Figures 1c,d). Written informed consent was obtained from the patient for the publication of her clinical information and imaging data.

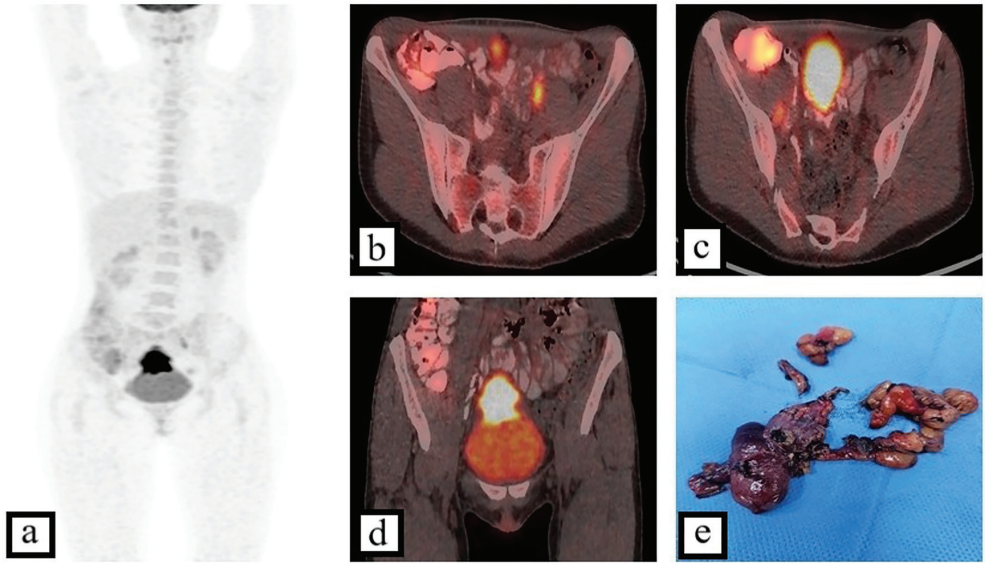

Figure 2. Cystoscopy confirmed a dome-based lesion, and transurethral biopsy specimens were obtained. Histopathological analysis revealed a squamous cell carcinoma. Primary urachal carcinoma is an uncommon malignancy arising from embryonic urachal remnants, accounting for less than 1% of all bladder cancers (1). According to a recent meta-analysis of registry data published in 2024, adenocarcinoma represents the predominant histological type, comprising approximately 86% of cases. By contrast, squamous cell carcinoma is an exceedingly rare variant, representing only about 2% of urachal tumors, with no more than 30 cases documented in the literature to date (2). The extreme rarity of this malignancy poses a significant therapeutic challenge, as its optimal management strategies remain poorly defined. The therapeutic approach and the overall prognosis are largely determined by clinical stage. Several staging systems have been proposed for urachal carcinoma, the most widely applied being those of Sheldon (3) and Mayo (4). To facilitate accurate staging, the patient underwent whole-body positron emission tomography/computed tomography (PET/

CT) with 2-deoxy-2-^{18}F-fluorodeoxyglucose (^{18}F-FDG). The maximum intensity projection image (Figure 2a) and the coronal fused PET/CT slice (Figure 2d) demonstrated a hypermetabolic solid soft-tissue mass extending along the urachal ligament to the bladder dome, with a maximum standardized uptake value (SUV_{max}) of 25.1. No evidence of distant metastatic disease was observed. However, axial fused PET/CT images of the pelvis revealed solitary ^{18}F-FDG -avid lymph nodes (SUV_{max} up to 5.4) along the left (Figure 2b) and right (Figure 2c) external iliac vessels. Although the therapeutic value of lymphadenectomy in urachal carcinoma remains a matter of debate, the suspicion of regional nodal involvement warranted an aggressive surgical approach in this case. The subsequent surgical procedure consisted of partial cystectomy with en bloc resection of the urachal ligament and umbilicus, combined with extended pelvic lymph node dissection (Figure 2e). Histopathological examination confirmed a low-grade, pure squamous cell urachal carcinoma with negative surgical margins and no nodal metastases, corresponding to stage II according to the Mayo classification and stage IIIA according to the Sheldon classification. Because the disease was node-negative, adjuvant chemotherapy was not considered mandatory in accordance with the National Comprehensive Cancer Network guidelines (5). Nevertheless, given the aggressive biological behavior of this malignancy and the marked glucose metabolism characteristic of this histological type, as demonstrated in the presented case, ^{18}F-FDG PET/CT may serve as a valuable tool for surveillance, particularly when there is clinical suspicion of local recurrence or distant metastasis.

Ethics

Informed Consent: Written informed consent was obtained from the patient for the publication of her clinical information and imaging data.

Footnotes

Authorship Contributions

Surgical and Medical Practices: Y.G., A.S., S.A., N.H., Concept: Y.G., A.S., Design: Y.G., G.G., Data Collection or Processing: Y.G., G.G., N.H., Analysis or Interpretation: Y.G., Literature Search: Y.G., V.H., Writing: Y.G., V.H.

Conflict of Interest: No conflicts of interest were declared by the authors.

Financial Disclosure: The authors declare that this study has received no financial support.

References

1. Bruins HM, Visser O, Ploeg M, Hulsbergen-van de Kaa CA, Kiemeney LA, Witjes JA. The clinical epidemiology of urachal carcinoma: results of a large, population based study. J Urol. 2012;188:1102-1107.
2. Olah C, Kubik A, Mátrai P, Engh MA, Barna V, Hegyi P, Reis H, Nyirády P, Szarvas T. Estimation of the incidence of urachal cancer: a systematic review and meta-analysis of registry-based studies. Urol Oncol. 2024;42:221.e1-221.e7.
3. Sheldon CA, Clayman RV, Gonzalez R, Williams RD, Fraley EE. Malignant urachal lesions. J Urol. 1984;131:1-8.
4. Ashley RA, Inman BA, Sebo TJ, Leibovich BC, Blute ML, Kwon ED, Zincke H. Urachal carcinoma: clinicopathologic features and long-term outcomes of an aggressive malignancy. Cancer. 2006;107:712-720.
5. National Comprehensive Cancer Network. Bladder Cancer. Version 1.2025. NCCN Clinical Practice Guidelines in Oncology. Available at: https://www.nccn.org/professionals/physician_gls/pdf/bladder.pdf

Interesting Image

Mol Imaging Radionucl Ther 2026;35(2):134-136 **DOI:***10.4274/mirt.galenos.2026.43179*

Impact of ^{18}F-FDG-PET/CT in Managing a Case of Fungal Prosthetic Valve Endocarditis

Mantar Kaynaklı Protez Kapak Endokarditi Olgusunun Yönetiminde ^{18}F-FDG-PET/BT'nin Etkisi

Komal Bishnoi[1], P Sai Sradha Patro[1], Girish Kumar Parida[1], Kanhaiyalal Agrawal[1], Debananda Sahoo[2]

[1]*All India Institute of Medical Sciences, Department of Nuclear Medicine, Bhubaneswar, India*
[2]*All India Institute of Medical Sciences, Department of General Medicine, Bhubaneswar, India*

Abstract

Approximately 0.1% of all prosthetic cardiac valves are affected by fungal endocarditis (bacterial endocarditis being the most common cause), which has a high case fatality rate. Post-treatment clinical improvement and a negative blood culture do not definitively rule out the presence of residual active disease. Among imaging techniques, trans-oesophageal echocardiography has higher sensitivity than transthoracic echocardiography, but has its own limitations. Functional imaging with ^{18}F-fluorodeoxyglucose positron emission tomography/computed tomography (^{18}F-FDG PET/CT) has shown to have high overall sensitivity, specificity, and accuracy for the diagnosis and follow-up evaluation of prosthetic valve infective endocarditis, thereby significantly influencing clinical management. Here, we report a rare case of a patient with Marfan syndrome and fungal prosthetic valve endocarditis, in which ^{18}F-FDG-PET/CT played a significant role in management decision.

Keywords: Marfan syndrome, fungal endocarditis, ^{18}F-FDG-PET/CT, prosthetic valve endocarditis, Candida endocarditis

Öz

Tüm protez kalp kapaklarının yaklaşık 0,1'i mantar endokarditinden etkilenir (en yaygın nedeni bakteriyeldir) ve yüksek bir ölüm oranına sahiptir. Tedavi sonrası klinik iyileşme ve negatif kan kültürü, kalan aktif hastalığın varlığını kesin olarak dışlamaz. Görüntüleme tekniklerinde, transözofageal ekokardiyografi, transtorasik ekokardiyografiye göre daha yüksek duyarlılığa sahiptir, ancak kendine özgü kısıtlılıkları da vardır. ^{18}F-florodeoksiglukoz pozitron emisyon tomografisi/bilgisayarlı tomografi (^{18}F-FDG PET/BT) ile fonksiyonel görüntüleme, protez kapak enfektif endokarditinin tanı ve takip değerlendirmesinde yüksek genel duyarlılık, özgüllük ve doğruluk göstererek klinik yönetimi önemli ölçüde etkilemektedir. Burada, Marfan sendromu ve fungal protez kapak endokarditi olan nadir bir olguyu sunuyoruz; bu olguda ^{18}F-FDG-PET/BT, tedavi kararında önemli bir rol oynamıştır.

Anahtar Kelimeler: Marfan sendromu, fungal endokardit, ^{18}F-FDG-PET/BT, protez kapak endokarditi, Candida endokarditi

Address for Correspondence: P Sai Sradha Patro, All India Institute of Medical Sciences, Department of Nuclear Medicine, Bhubaneswar, India
E-mail: drpsaisradha@gmail.com **ORCID ID:** orcid.org/0000-0002-8217-6565
Received: 22.10.2025 **Accepted:** 20.01.2026 **Epub:** 06.03.2026 **Publication Date:** 04.06.2026

Cite this article as: Bishnoi K, Patro PSS, Parida GK, Agrawal K, Sahoo D. Impact of ^{18}F-FDG-PET/CT in managing a case of fungal prosthetic valve endocarditis. Mol Imaging Radionucl Ther. 2026;35(2):134-136.

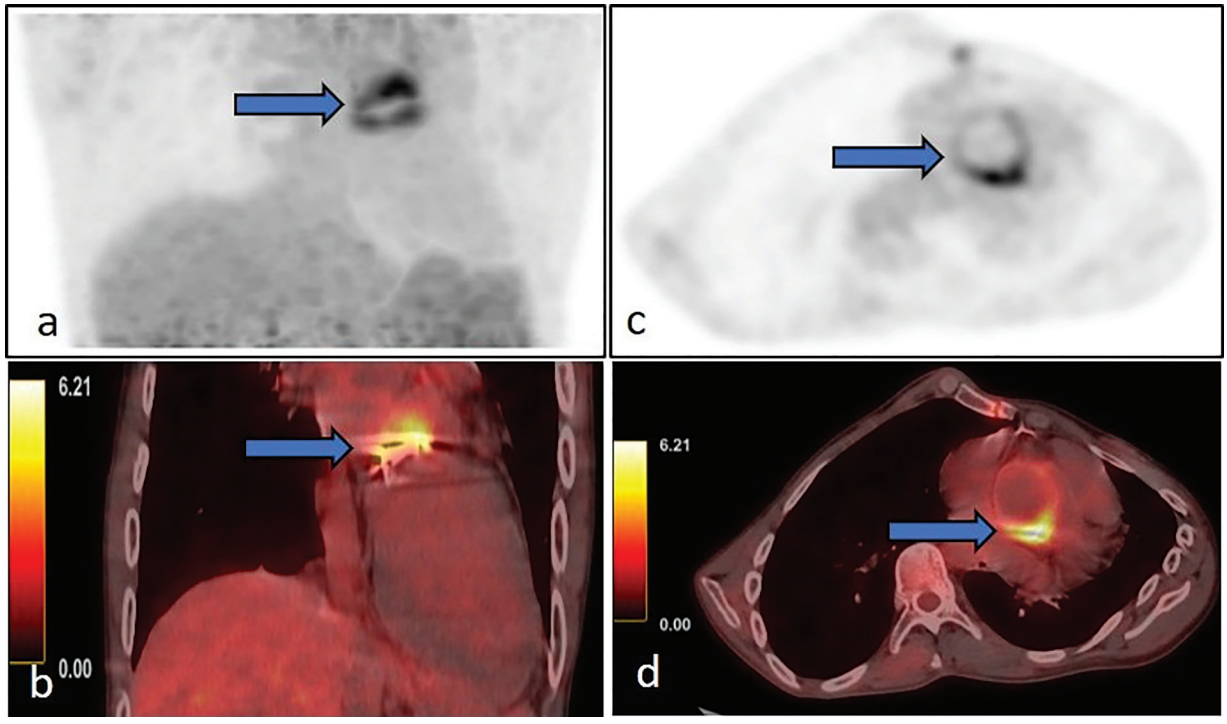

Figure 1. A 28 years-old-male patient with Marfan syndrome associated with severe aortic regurgitation and dilated aorta underwent aortic valve replacement surgery. One month later, he developed fungal prosthetic valve endocarditis with positive blood culture (*Candida albicans* and *Candida parapsilosis*), and 2D transthoracic echocardiography (TTE) showed multiple vegetations on the anterior mitral leaflet and the prosthetic aortic valve. After 6 weeks of treatment, repeat blood culture, 2D TTE and transesophageal echocardiography were negative for residual active disease.^{18}F-fluorodeoxyglucose positron emission tomography/computed tomography (^{18}F-FDG PET/CT) (a-d) was performed to confirm any residual active focus in the heart before proceeding towards step-down approach to therapy. Cardiac non-attenuation corrected (NAC) maximum intensity projection and axial images (a,c) and corresponding fused PET/CT coronal and axial images (b,d) showed circumferential heterogeneously increased metabolic activity along the aortic prosthetic valve, suggestive of persistent residual infection. Increased metabolic activity on the NAC image ruled out a false-positive result due to overcorrection by the metallic prosthesis. Positive ^{18}F-FDG-PET/CT led to continuation of antifungal treatment in this case. Fungal endocarditis accounts for 1% to 3% of all infective endocarditis (IE) cases, affects nearly 0.1% of all prosthetic cardiac valves, and is disproportionately associated with a high morbidity and case fatality rate (>70%); it also presents greater diagnostic challenges compared with bacterial IE (1). *Candida* species are the most common cause of fungal endocarditis (2). Blood cultures and echocardiography can be falsely negative, as in this case. ^{18}F-FDG-PET/CT has high sensitivity and specificity of 86% and 84%, respectively for IE (3). 2023 Duke-International Society for Cardiovascular Infectious Diseases Criteria for Infective Endocarditis Criteria has incorporated ^{18}F-FDG-PET/CT in the major imaging criteria for its diagnosis owing to its high positive predictive value (4).

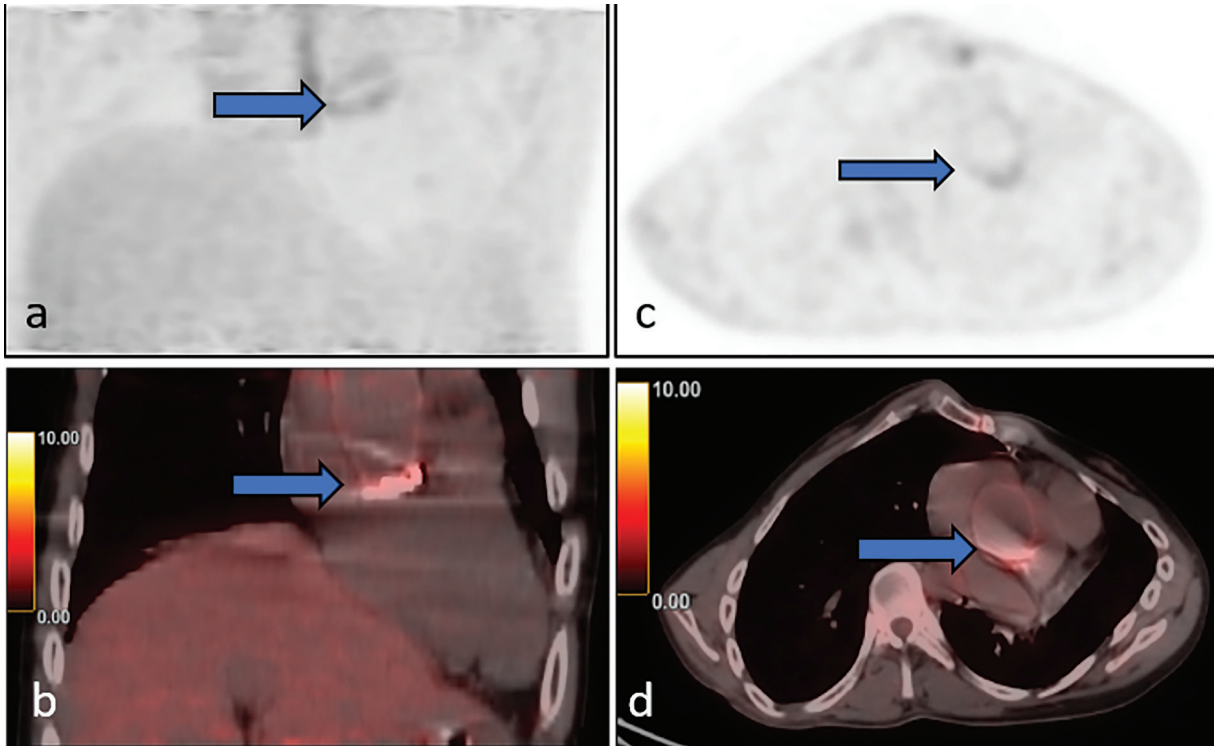

Figure 2. Corresponding follow up [18]F-fluorodeoxyglucose positron emission tomography/computed tomography ([18]F-FDG PET/CT) images (a-d) after 8 months of treatment showed near complete resolution of the metabolic activity suggesting complete metabolic response to therapy, thus guiding treatment discontinuation. The Step-down approach to therapy is relatively common in fungal prosthetic valve endocarditis, as the infection resolves following an initial course of antifungal agents. However, long-term suppressive antifungal therapy is indicated in selected groups of patients in whom the infection persists (5). This case of fungal prosthetic valve endocarditis highlights the important role and high diagnostic value of [18]F-FDG-PET/CT in finding occult/residual disease in cases of negative routine diagnostic results, guiding further management and also for final response evaluation.

Ethics

Informed Consent: The participants signed a consent regarding publishing their data and photographs.

Footnotes

Authorship Contributions

Surgical and Medical Practices: D.S., Concept: K.B., P.S.S.P., G.K.P., K.A., D.S., Design: K.B., P.S.S.P., G.K.P., K.A., D.S., Data Collection or Processing: K.B., P.S.S.P., D.S., Analysis or Interpretation: K.B., P.S.S.P., G.K.P., K.A., D.S., Literature Search: K.B., P.S.S.P., Writing: K.B., P.S.S.P., G.K.P., K.A., D.S.

Conflict of Interest: No conflicts of interest were declared by the authors.

Financial Disclosure: The authors declare that this study has received no financial support.

References

1. Antinori S, Ferraris L, Orlando G, Tocalli L, Ricaboni D, Corbellino M, Sollima S, Galli M, Milazzo L. Fungal endocarditis observed over an 8-year period and a review of the literature. Mycopathologia. 2014;178:37-51.
2. Clancy CJ, Nguyen MH. Non-culture diagnostics for invasive candidiasis: promise and unintended consequences. Journal of Fungi. 2018;4:27.
3. Wang TKM, Sánchez-Nadales A, Igbinomwanhia E, Cremer P, Griffin B, Xu B. Diagnosis of infective endocarditis by subtype using 18f-fluorodeoxyglucose positron emission tomography/computed tomography: a contemporary meta-analysis. Circ Cardiovasc Imaging. 2020;13:e010600.
4. Fowler VG, Durack DT, Selton-Suty C, Athan E, Bayer AS, Chamis AL, Dahl A, DiBernardo L, Durante-Mangoni E, Duval X, Fortes CQ, Fosbøl E, Hannan MM, Hasse B, Hoen B, Karchmer AW, Mestres CA, Petti CA, Pizzi MN, Preston SD, Roque A, Vandenesch F, van der Meer JTM, van der Vaart TW, Miro JM. The 2023 Duke-international society for cardiovascular infectious diseases criteria for infective endocarditis: updating the modified duke criteria. Clin Infect Dis. 2023;77:518-526.
5. Arnold CJ, Johnson M, Bayer AS, Bradley S, Giannitsioti E, Miró JM, Tornos P, Tattevin P, Strahilevitz J, Spelman D, Athan E, Nacinovich F, Fortes CQ, Lamas C, Barsic B, Fernández-Hidalgo N, Muñoz P, Chu VH. Candida infective endocarditis: an observational cohort study with a focus on therapy. Antimicrob Agents Chemother. 2015;59:2365-2373.

Interesting Image

Mol Imaging Radionucl Ther 2026;35(2):137-141 **DOI:***10.4274/mirt.galenos.2026.09475*

Metabolically Silent Diffuse Hepatic Involvement in Multiple Myeloma: An ^{18}F-FDG-PET/CT Pitfall

Multipl Miyelomda Metabolik Olarak Sessiz Diffüz Hepatik Tutulum: ^{18}F-FDG- PET/BT'de Bir Tanısal Tuzak

Seçkin Bilgiç[1], Merve Okuyan[2], Efrah İbrahim[1]

[1]*Bursa Uludağ University Faculty of Medicine, Department of Nuclear Medicine, Bursa, Türkiye*
[2]*Recep Tayyip Erdoğan University Training and Research Hospital, Clinic of Nuclear Medicine, Rize, Türkiye*

Abstract

Diffuse hepatic involvement in multiple myeloma is rare and may present a diagnostic challenge ^{18}F-fluorodeoxyglucose positron emission tomography/computed tomography (^{18}F-FDG PET/CT). We present the case of a 59-year-old man with a 3-year history of multiple myeloma who developed progressive hepatomegaly and perihepatic ascites. ^{18}F-FDG PET/CT demonstrated marked diffuse liver enlargement without any focal or diffuse hepatic ^{18}F-FDG uptake, while mild diffuse skeletal uptake suggested a globally ^{18}F-FDG-low myeloma phenotype. Given the discordance between severe morphological findings and the absence of hepatic metabolic activity, a liver biopsy was performed, which revealed diffuse sinusoidal infiltration by CD138-positive, lambda-restricted plasma cells and excluded hepatic amyloidosis. Following systemic therapy, hepatomegaly and ascites regressed, while hepatic ^{18}F-FDG uptake remained absent. Written informed consent for publication was obtained from the patient. This case highlights an important limitation of ^{18}F-FDG PET/CT in detecting diffuse hepatic myeloma and emphasizes the need for multimodal diagnostic integration.

Keywords: ^{18}F-FDG PET/CT, hepatic myeloma, diagnostic pitfall, multiple myeloma, hepatomegaly, liver biopsy

Öz

Multipl miyelomda diffüz hepatik tutulum nadirdir ve ^{18}F-florodeoksiglukoz pozitron emisyon tomografisi/bilgisayarlı tomografi (^{18}F-FDG PET/BT) tanısal güçlük oluşturabilir. Bu yazıda, üç yıldır multipl miyelom tanısı bulunan ve progresif hepatomegali ile perihepatik asit gelişen 59 yaşında bir erkek hasta sunulmaktadır. ^{18}F-FDG PET/BT'de karaciğerde belirgin diffüz büyüme izlenmesine karşın, fokal ya da diffüz hepatik ^{18}F-FDG tutulumu saptanmamış; iskelette izlenen hafif diffüz ^{18}F-FDG tutulumu ise global ^{18}F-FDG düşük bir miyelom fenotipini düşündürmüştür. Belirgin morfolojik bulgular ile hepatik metabolik aktivitenin yokluğu arasındaki uyumsuzluk nedeniyle karaciğer biyopsisi yapılmış ve CD138 pozitif, lambda ile sınırlı plazma hücrelerinin diffüz sinüzoidal infiltrasyonu saptanarak hepatik amiloidoz dışlanmıştır. Sistemik tedavi sonrası hepatomegali ve asitte gerileme izlenirken, hepatik ^{18}F-FDG tutulumu olmaması devam etmiştir. Yayın için hastadan yazılı bilgilendirilmiş onam alınmıştır. Bu olgu, diffüz hepatik miyelom tutulumunun saptanmasında ^{18}F-FDG PET/BT'nin önemli bir sınırlılığını ortaya koymakta ve tanıda multimodal yaklaşımın gerekliliğini vurgulamaktadır.

Anahtar Kelimeler: ^{18}F-FDG PET/BT, karaciğer miyelomu, tanı hatası, multipl miyelom, hepatomegali, karaciğer biyopsisi

Address for Correspondence: Seçkin Bilgiç, Bursa Uludağ University Faculty of Medicine, Department of Nuclear Medicine, Bursa, Türkiye
E-mail: seckinbilgic@uludag.edu.tr **ORCID ID:** orcid.org/0000-0002-3429-7549
Received: 11.12.2025 **Accepted:** 10.02.2026 **Epub:** 06.03.2026 **Publication Date:** 04.06.2026

Cite this article as: Bilgiç S, Okuyan M, İbrahim E. Metabolically silent diffuse hepatic involvement in multiple myeloma: an ^{18}F-FDG-PET/CT pitfall. Mol Imaging Radionucl Ther. 2026;35(2):137-141.

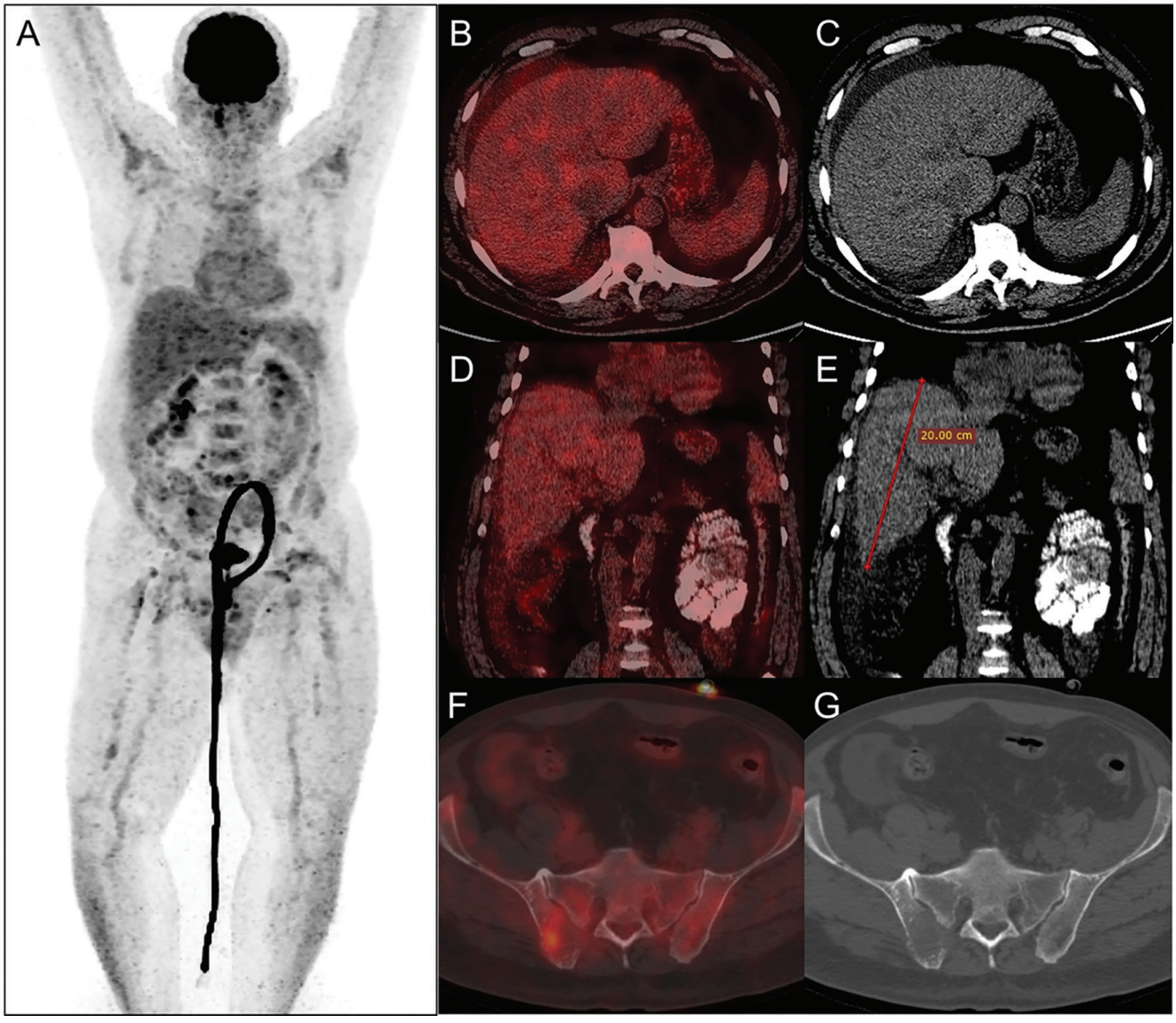

Figure 1. ^{18}F-fluorodeoxyglucose positron emission tomography/computed tomography (^{18}F-FDG PET/CT) findings in a 59-year-old male with a 3-year history of multiple myeloma who developed progressive hepatomegaly and perihepatic ascites 1A. Maximum-intensity projection image demonstrates marked hepatomegaly with no abnormal hepatic ^{18}F-FDG uptake 1B,C. Axial fused ^{18}F-FDG PET/CT and CT images show diffuse hepatic enlargement and mild parenchymal heterogeneity without abnormal metabolic activity 1D-E. Coronal fused ^{18}F-FDG PET/CT and CT images illustrate hepatomegaly with a craniocaudal measurement of approximately 20 cm 1F-G. Axial fused ^{18}F-FDG PET/CT and CT images at the pelvic level reveal mild-low ^{18}F-FDG-avid lytic lesions in the posterior iliac bones. Given the absence of focal hypermetabolic lesions and the low-grade, diffuse pattern of skeletal uptake, these findings are compatible with a globally ^{18}F-FDG -low myeloma phenotype rather than highly active focal disease (1,2).

According to the IMWG-endorsed Italian Myeloma Criteria for PET Use (IMPeTUs), the imaging findings were consistent with a low-^{18}F-FDG-avid myeloma phenotype. Bone marrow uptake demonstrated a Deauville score of 3 (BM3) with a mixed diffuse-focal pattern. Six lytic lesions were identified (L3 group), with the highest ^{18}F-FDG uptake at the iliac bone biopsy site [maximum standardized uptake value (SUV_{max}): 4.8], comparable to hepatic reference activity (SUV_{max}: 4.1). No paramedullary or extramedullary metabolically active disease was detected. Overall, the IMPeTUs profile was classified as BM3 Sp F2 L3. Bone marrow biopsy demonstrated marked plasma-cell infiltration (approximately 85% of marrow cellularity) with CD138 and MUM1 positivity and lambda light-chain restriction (kappa/lambda ratio 1/80), consistent with relapsed plasma cell myeloma.

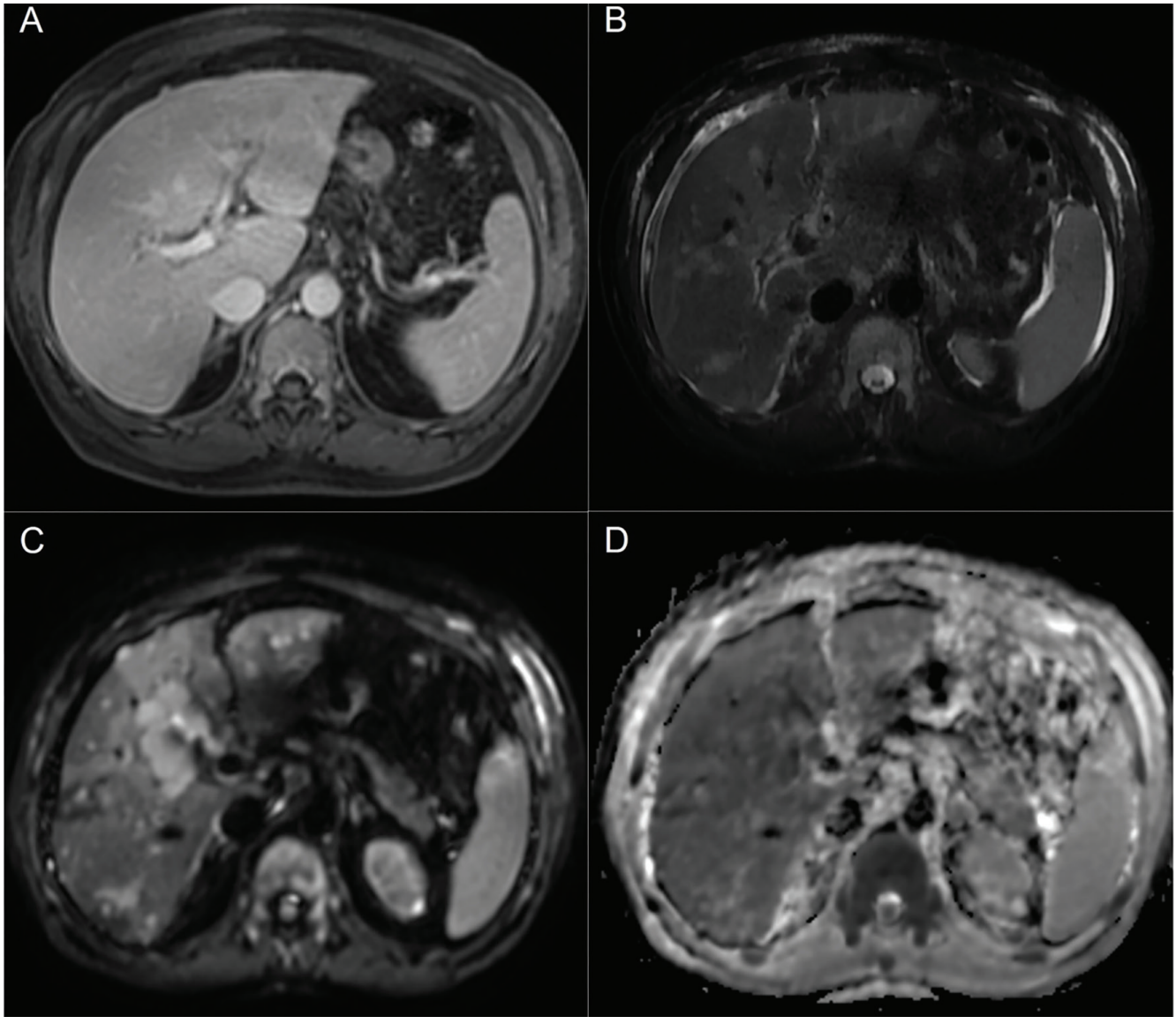

Figure 2. Liver magnetic resonance imaging demonstrating diffuse hepatic infiltration in multiple myeloma 2A. Axial contrast-enhanced T1-weighted image shows heterogeneous parenchymal enhancement without discrete focal lesion 2B. Axial T2-weighted image demonstrates hepatomegaly with heterogeneous, mildly increased parenchymal signal intensity without discrete focal lesions 2C. Diffusion-weighted image (b=800) shows heterogeneous parenchymal hyperintensity without discrete focal lesions 2D. Apparent diffusion coefficient map shows diffusely reduced signal intensity, supporting restricted diffusion in keeping with diffuse plasma-cell infiltration. As previously reported in the literature, magnetic resonance images findings of diffuse hepatic myeloma may be subtle and non-specific, often manifesting as heterogeneous parenchymal signal alterations without discrete mass formation (3,4).

Hepatic involvement in multiple myeloma is uncommon, and tumor-forming hepatic lesions are particularly rare. Reported histopathological patterns include extramedullary plasmacytoma, light-chain deposition disease, amyloidosis, and diffuse infiltrative forms such as sinusoidal plasma-cell infiltration, which may present radiologically as hepatomegaly with ascites in the absence of discrete focal lesions (3).

The striking discrepancy between severe hepatomegaly with ascites and complete absence of hepatic ^{18}F-fluorodeoxyglucose uptake prompted further diagnostic evaluation. Percutaneous liver biopsy demonstrated diffuse sinusoidal infiltration by plasma cells with strong CD138 expression and lambda light-chain restriction, confirming hepatic involvement by multiple myeloma. Congo red staining was negative, excluding hepatic amyloidosis (5,6).

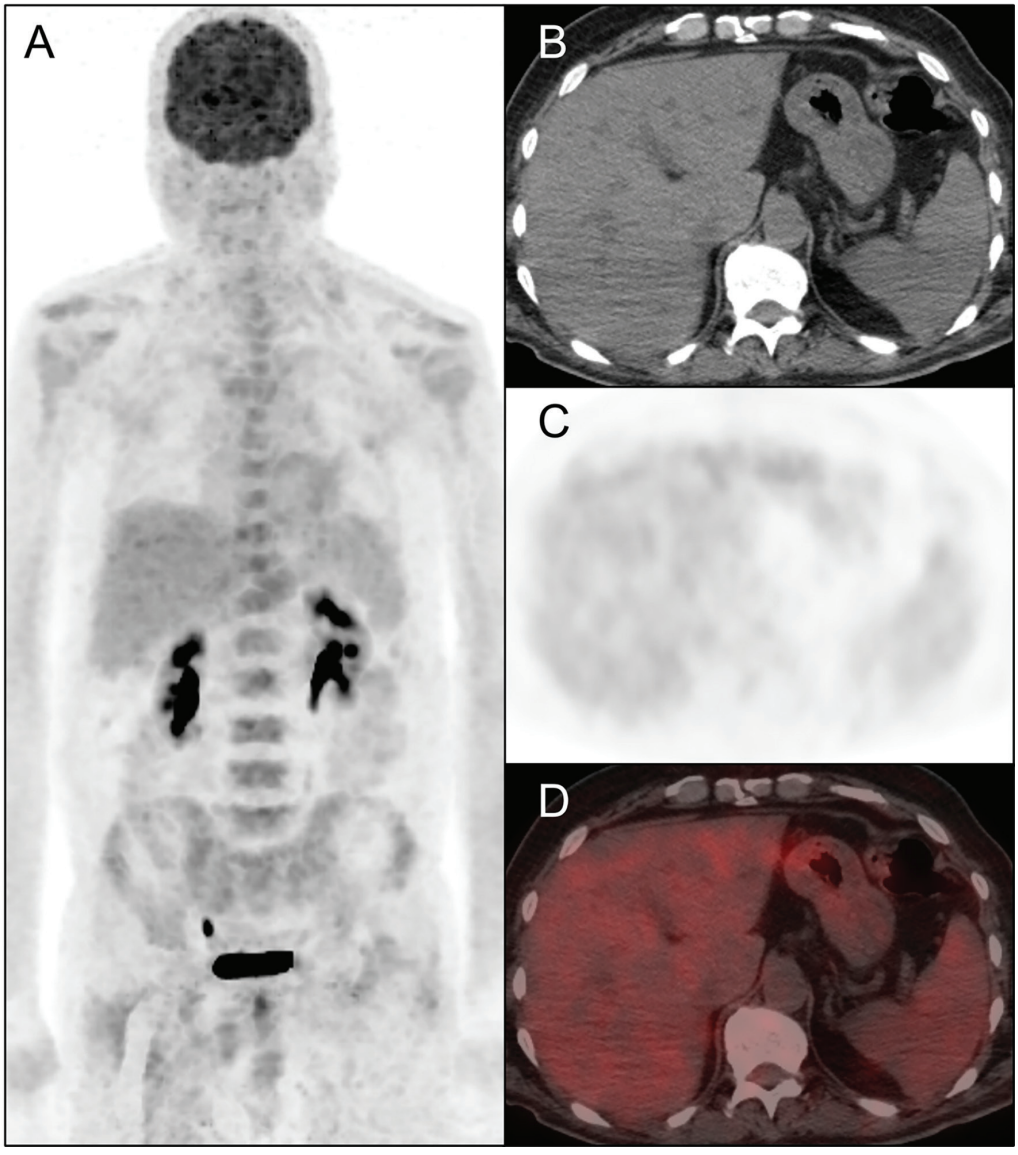

Figure 3. Follow-up [18]F-fluorodeoxyglucose positron emission tomography/computed tomography ([18]F-FDG PET/CT) findings after systemic therapy 3A. MIP image demonstrates interval decrease in diffuse skeletal [18]F-FDG uptake compared with baseline, with no newly emerged focal hypermetabolic lesions. Hepatic[18]F-FDG activity remains homogeneous and within physiological limits 3B. Axial low-dose CT image shows regression of hepatomegaly with improved hepatic contour and parenchymal homogeneity, with the craniocaudal liver length measuring approximately 15.6 cm 3C. Axial PET image at the hepatic level demonstrates persistently low-grade, diffuse [18]F-FDG uptake within the liver parenchyma, without abnormal focal activity. 3D. Axial fused [18]F-FDG PET/CT image confirms the absence of focal hepatic [18]F-FDG uptake and demonstrates interval improvement of hepatic findings following systemic therapy, in keeping with the observed clinical improvement.

Hepatic involvement in multiple myeloma is uncommon, with reported frequencies ranging from approximately 0.3-3%, and diffuse infiltrative patterns are far less frequently encountered than focal plasmacytomas. Histopathological manifestations include diffuse sinusoidal plasma-cell infiltration, light-chain deposition disease, amyloidosis, and less commonly tumor-forming lesions. This case illustrates a well-recognized but underappreciated limitation of [18]F-FDG PET/CT in detecting diffuse hepatic involvement; low [18]F-FDG avidity in such presentations has been proposed to relate to reduced hexokinase-2 expression and alternative metabolic pathways in certain plasma-cell phenotypes, as supported by prior translational and imaging studies rather than being directly demonstrated in the present case (7,8,9). In patients presenting with unexplained hepatomegaly and discordant metabolic imaging findings, histopathological confirmation remains essential. In this context, alternative PET tracers most notably CXCR4-targeted agents and, more recently, fluorocholine PET may provide complementary information in [18]F-FDG -low myeloma phenotypes (10,11,12).

Ethics

Informed Consent: Written informed consent for publication was obtained from the patient.

Footnotes

Authorship Contributions

Surgical and Medical Practices: S.B., Concept: S.B., E.A.İ., Design: S.B., M.O., E.A.İ., Data Collection or Processing: S.B., E.A.İ., Analysis or Interpretation: S.B., E.A.İ., Literature Search: M.O., E.A.İ., Writing: S.B., M.O., E.A.İ.

Conflict of Interest: No conflicts of interest were declared by the authors.

Financial Disclosure: The authors declare that this study has received no financial support.

References

1. Cavo M, Terpos E, Nanni C, Moreau P, Lentzsch S, Zweegman S, Hillengass J, Engelhardt M, Usmani SZ, Vesole DH, San-Miguel J, Kumar SK, Richardson PG, Mikhael JR, da Costa FL, Dimopoulos MA, Zingaretti C, Abildgaard N, Goldschmidt H, Orlowski RZ, Chng WJ, Einsele H, Lonial S, Barlogie B, Anderson KC, Rajkumar SV, Durie BGM, Zamagni E. Role of ^{18}F-FDG PET/CT in the diagnosis and management of multiple myeloma and other plasma cell disorders: a consensus statement by the International Myeloma Working Group. Lancet Oncol. 2017;18:e206-e217.
2. Tirumani SH, Sakellis C, Jacene H, Shinagare AB, Munshi NC, Ramaiya NH, Van den Abbeele AD. Role of FDG-PET/CT in extramedullary multiple myeloma: correlation of FDG-PET/CT findings with clinical outcome. Clin Nucl Med. 2016;41:e7-e13.
3. Tirotta D, Lena C, Torre M, Muratori P. Hematologic focal hepatic lesions in the absence of liver cirrhosis: consider lymphoma and myeloma. Clin Res Hepatol Gastroenterol. 2026;50:102749.
4. Tomasian A, Sandrasegaran K, Elsayes KM, Shanbhogue A, Shaaban A, Menias CO. Hematologic malignancies of the liver: spectrum of disease. Radiographics. 2015;35:71-86.
5. Pu Z, Zhan L, Zha Y, Li Y, Qiu S, He Y, Yang Y, Feng Z, Zhu X. Hepatic involvement as an initial manifestation of multiple myeloma: a case report with atypical imaging features. Front Oncol. 2025;15:1640981.
6. Singh M, Singh H, Pham P, Rizvi B, Rao R. Extramedullary multiple myeloma with hepatic involvement. Cureus. 2021;13:e13515.
7. Abe Y, Ikeda S, Kitadate A, Narita K, Kobayashi H, Miura D, Takeuchi M, O'uchi E, O'uchi T, Matsue K. Low hexokinase-2 expression-associated false-negative ^{18}F-FDG PET/CT as a potential prognostic predictor in patients with multiple myeloma. Eur J Nucl Med Mol Imaging. 2019;46:1345-1350.
8. Rasche L, Angtuaco E, McDonald JE, Buros A, Stein C, Pawlyn C, Thanendrarajan S, Schinke C, Samant R, Yaccoby S, Walker BA, Epstein J, Zangari M, van Rhee F, Meissner T, Goldschmidt H, Hemminki K, Houlston R, Barlogie B, Davies FE, Morgan GJ, Weinhold N. Low expression of hexokinase-2 is associated with false-negative FDG-positron emission tomography in multiple myeloma. Blood. 2017;130:30-34.
9. Zamagni E, Patriarca F, Nanni C, Zannetti B, Englaro E, Pezzi A, Tacchetti P, Buttignol S, Perrone G, Brioli A, Pantani L, Terragna C, Carobolante F, Baccarani M, Fanin R, Fanti S, Cavo M. Prognostic relevance of 18-F FDG PET/CT in newly diagnosed multiple myeloma patients treated with up-front autologous transplantation. Blood. 2011;118:5989-5995.
10. Shekhawat AS, Singh B, Malhotra P, Watts A, Basher R, Kaur H, Hooda M, Radotra BD. Imaging CXCR4 receptors expression for staging multiple myeloma by using ^{68}Ga-pentixafor PET/CT: comparison with ^{18}F-FDG PET/CT. Br J Radiol. 2022;95:20211272.
11. Kaya G, Akin S, Buyukasik Y, Bozkurt MF, Tuncel M, Kiratli PO. PET in myeloma redefined: a comparative imaging study with FDG and fluorocholine PET/CT. Eur J Nucl Med Mol Imaging. 2026;53:2325-2336.
12. Chavoshi M, Mirshahvalad SA, Kohan A, Ortega C, Metser U, Farag A, Kridel R, Hodgson D, Bhella S, Kukreti V, Veit-Haibach P. CXCR4-targeted PET imaging in hematologic malignancies: a systematic review and meta-analysis. Clin Nucl Med. 2025;50:e7-e16.

Interesting Image

Mol Imaging Radionucl Ther 2026;35(2):142-144 **DOI:***10.4274/mirt.galenos.2026.83097*

^{18}F-FDG-PET/MRI Demonstration of Extensive Spinal Cord Metastases in a Patient with Ovarian Carcinoma

Over Karsinomlu Bir Hastada Yaygın Spinal Kord Metastazlarının ^{18}F-FDG-PET/MRG ile Görüntülenmesi

Cansu Güneren[1], Sertaç Asa[2], Haluk Burçak Sayman[2]

[1]*University of Health Sciences Türkiye, İstanbul Şişli Hamidiye Etfal Training and Research Hospital, Clinic of Nuclear Medicine, İstanbul, Türkiye*

[2]*İstanbul University-Cerrahpaşa, Cerrahpaşa Faculty of Medicine, Department of Nuclear Medicine, İstanbul, Türkiye*

Abstract

Spinal cord involvement is a rare manifestation of metastatic ovarian carcinoma. We report a case of high-grade serous ovarian cancer initially diagnosed in 2020. After cytoreductive surgery and multiple chemotherapy regimens, the patient developed brain metastases followed by small hypermetabolic foci along the spinal canal detected on ^{18}F-fluorodeoxyglucose positron emission tomography/magnetic resonance imaging (^{18}F-FDG PET/MRI). These lesions, primarily located in the cervical region, were confirmed by contrast-enhanced spinal MRI but were more clearly visualized on ^{18}F-FDG PET/MRI. Intramedullary spinal cord metastases are extremely rare and often underdiagnosed. While MRI remains the standard for anatomical assessment, ^{18}F-FDG PET/MRI demonstrated superior lesion detection and definition in this case. This highlights the potential of hybrid imaging for improved diagnostic sensitivity in patients with suspected central nervous system involvement.

Keywords: ^{18}F-FDG PET/MRI, ovarian carcinoma, spinal cord metastasis, hybrid imaging

Öz

Spinal kord tutulumu, metastatik over karsinomunun nadir bir bulgusudur. Bu yazıda, 2020 yılında tanı almış yüksek dereceli seröz over karsinomlu bir olgu sunulmaktadır. Sitoredüktif cerrahi ve çoklu kemoterapi rejimlerinin ardından hastada önce beyin metastazları gelişmiş, sonrasında ise ^{18}F-florodeoksiglukoz pozitron emisyon tomografisi/manyetik rezonans görüntüleme (^{18}F-FDG PET/MRG) görüntülemede spinal kanal boyunca hipermetabolik odaklar saptanmıştır. Bu lezyonlar, ağırlıklı olarak servikal bölgede yerleşimli olup kontrastlı spinal MRG ile doğrulanmış, ancak ^{18}F-FDG PET/MRG görüntülemede daha net olarak izlenmiştir. İntramedüller spinal kord metastazları son derece nadir olup sıklıkla gözden kaçabilmektedir. Anatomik değerlendirme için MRG standart yöntem olmaya devam etmekle birlikte, bu olguda ^{18}F-FDG PET/MRG daha üstün lezyon saptama ve tanımlama sağlamıştır. Bu bulgular, santral sinir sistemi tutulumu şüphesi olan hastalarda hibrit görüntülemenin tanısal duyarlılığı artırma potansiyeline işaret etmektedir.

Anahtar Kelimeler: ^{18}F-FDG PET/MRG, over karsinomu, spinal kord metastazı, hibrit görüntüleme

Address for Correspondence: Cansu Güneren, University of Health Sciences Türkiye, İstanbul Şişli Hamidiye Etfal Training and Research Hospital, Clinic of Nuclear Medicine, İstanbul, Türkiye

E-mail: mdcansuguneren@gmail.com **ORCID ID:** orcid.org/0009-0006-6766-2166

Received: 17.12.2025 **Accepted:** 19.02.2026 **Epub:** 06.03.2026 **Publication Date:** 04.06.2026

Cite this article as: Güneren C, Asa S, Sayman HB. ^{18}F-FDG-PET/MRI demonstration of extensive spinal cord metastases in a patient with ovarian carcinoma. Mol Imaging Radionucl Ther. 2026;35(2):142-144.

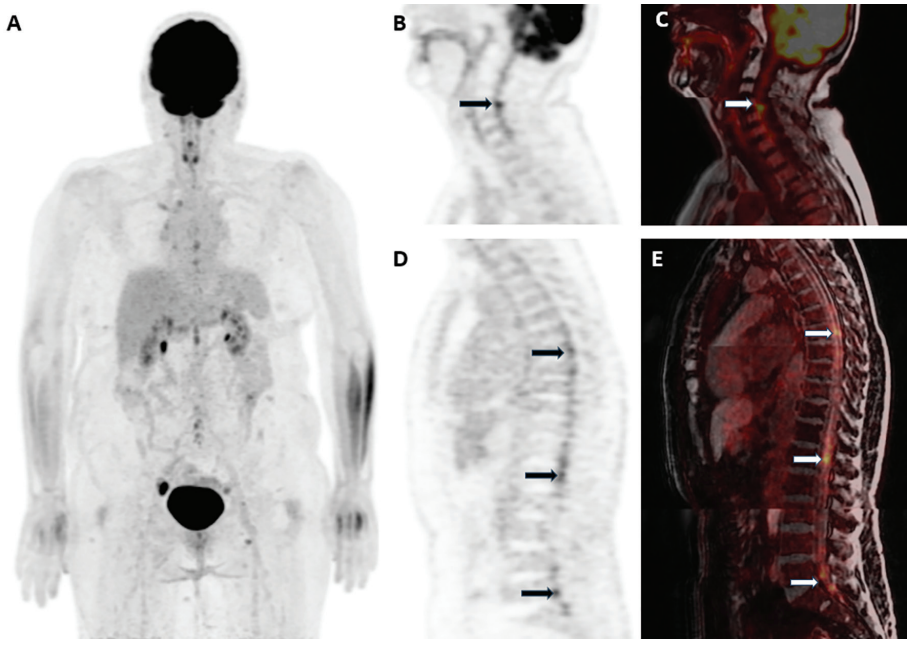

Figure 1. Hypermetabolic spinal cord metastases are observed in the cervical and thoracolumbar regions of a patient under follow-up for high-grade serous ovarian carcinoma [A: maximum intensity projection; sagittal B: positron emission tomography (PET), black arrow; C: fused PET/magnetic resonance imaging (MRI), white arrow; sagittal D: PET, black arrow; E: fused PET/MRI, white arrow]. Following intravenous administration of 3.75 mCi ^{18}F-fluorodeoxyglucose (^{18}F-FDG) PET/MRI imaging from the vertex to the upper thighs was performed 50 minutes post-injection using a 3-Tesla time-of-flight PET/MRI system available at our institution (GE Signa PET/MRI, GE Healthcare, Waukesha, WI, USA). For anatomical correlation and attenuation correction, MRI-based attenuation correction images were acquired, and vertex-to-upper-thigh, T1-weighted, three-dimensional, dual-echo, fast spoiled gradient-recalled echo liver-accelerated volume acquisition sequences were used for PET/MRI fusion imaging.

Central nervous system (CNS) involvement is an uncommon manifestation of metastatic ovarian carcinoma. Though the liver is the most frequent site of distant spread, spinal cord metastases remain rare. The anatomical distribution of metastases is an independent prognostic factor (1). We present a case of spinal cord metastasis from high-grade serous ovarian carcinoma, emphasizing the diagnostic value of ^{18}F-FDG PET/MRI compared to conventional MRI.

The patient was a 42-year-old female initially diagnosed in 2020 with high-grade serous ovarian carcinoma following cytoreductive surgery that included total hysterectomy, bilateral salpingo-oophorectomy, omentectomy, and excision of multiple peritoneal implants. Based on surgical pathology, the disease was classified as FIGO stage IIIC. Between 2020 and 2024, the patient received multiple lines of systemic chemotherapy, including carboplatin–paclitaxel, gemcitabine, and bevacizumab-based regimens. During follow-up in 2024, brain metastases developed; palliative whole-brain radiotherapy was administered at a total dose of 30 Gy in 10 fractions. Subsequently, ^{18}F-FDG PET/MRI revealed small hypermetabolic foci along the spinal canal particularly in the cervical region adjacent to the spinal cord, suggestive of metastases. Contrast-enhanced spinal MRI confirmed nodular enhancement in the corresponding regions. Contrast-enhanced spinal MRI on post-contrast T1-weighted images demonstrated nodular, contrast-enhancing lesions within the spinal canal along the spinal cord and interspersed between the cauda equina nerve roots, consistent with intraspinal metastatic spread, compatible with leptomeningeal disease. However, compared with the hypermetabolic foci observed on ^{18}F-FDG PET/MRI, precise anatomical delineation of individual lesions was challenging on MRI alone. PET/MRI provided complementary value to spinal MRI by improving lesion detection and delineation through the addition of metabolic imaging. Based on the PET/MRI findings, targeted radiotherapy was initiated.

Spinal cord metastases are extremely rare, occurring in 0.9-2.1% of cancer autopsies and accounting for 8.5% of all CNS metastases. Ovarian cancer cases with spinal involvement are rarely reported and are mostly identified by MRI (2-5). Nevertheless, several case reports have demonstrated the contribution of ^{18}F-FDG PET/computed tomography to detecting spinal cord metastases in ovarian cancer and other malignancies (6-8). While MRI remains the gold standard for anatomical evaluation and surgical planning (9), ^{18}F-FDG PET/MRI adds diagnostic value, especially for detecting subtle or widespread lesions. As demonstrated in this patient, PET/MRI may represent a diagnostically superior modality in selected clinical contexts.

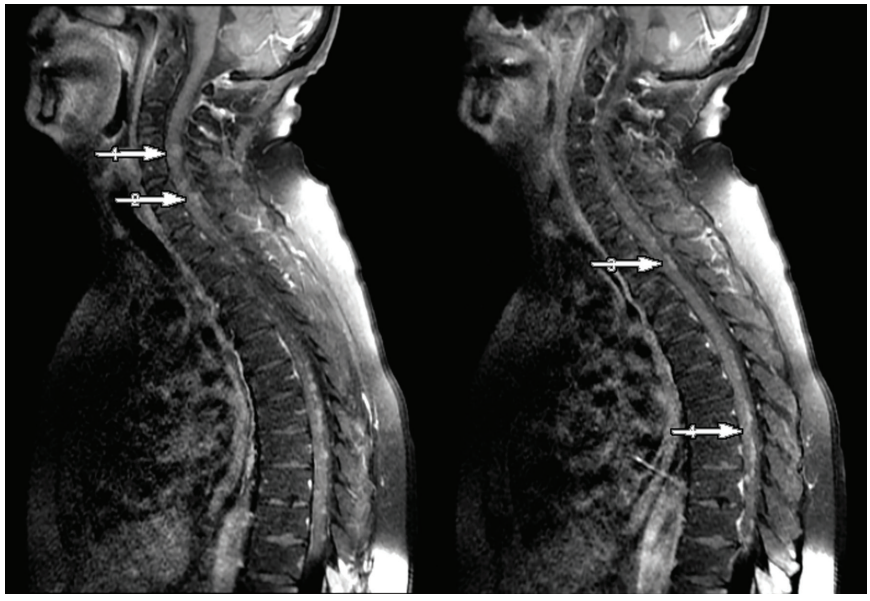

Figure 2. Post-contrast sagittal T1-weighted spinal magnetic resonance imaging (MRI), images of the same patient reveal subtle nodular contrast enhancement (white arrows) in the cervical and thoracic spinal cord, corresponding to the hypermetabolic foci observed on [18]F-fluorodeoxyglucose positron emission tomography/MRI, although lesion conspicuity is limited.

Ethics

Informed Consent: Informed consent was obtained from the patient for publication.

Footnotes

Authorship Contributions

Concept: C.G., S.A., H.B.S., Design: C.G., S.A., H.B.S., Data Collection or Processing: C.G., Literature Search: C.G., Writing: C.G., S.A., H.B.S.

Conflict of Interest: No conflicts of interest were declared by the authors.

Financial Disclosure: The authors declare that this study has received no financial support.

References

1. Deng K, Yang C, Tan Q, Song W, Lu M, Zhao W, Lou G, Li Z, Li K, Hou Y. Sites of distant metastases and overall survival in ovarian cancer: a study of 1481 patients. Gynecol Oncol. 2018;150:460-465.
2. Kłębczyk AW, Wolszczak Z, Urbaniak-Wąsik S, Podlewski S. Metastasis of ovarian cancer to the spinal cord — case study. Oncology in Clinical Practice. 2021;17:81-84.
3. Miranpuri AS, Rajpal S, Salamat MS, Kuo JS. Upper cervical intramedullary spinal metastasis of ovarian carcinoma: a case report and review of the literature. J Med Case Rep. 2011;5:311.
4. Safadi S, Rendon P, Rutledge T, Mayasy S. Ovarian carcinoma with isolated spinal cord metastasis. J Investig Med High Impact Case Rep. 2016;4:2324709616657644.
5. Cormio G, Di Vagno G, Di Fazio F, Loverro G, Selvaggi L. Intramedullary spinal cord metastasis from ovarian carcinoma. Gynecol Oncol. 2001;81:506-508.
6. Kalimuthu LM, Ora M, Gambhir S. Recurrent renal carcinoma with solitary intramedullary spinal cord metastasis. Indian J Nucl Med. 2020;35:358-9.
7. Nguyen NC, Sayed MM, Taalab K, Osman MM. Spinal cord metastases from lung cancer: detection with F-18 FDG PET/CT. Clin Nucl Med. 2008;33:356-358.
8. Krupa M, Byun K. Leptomeningeal carcinomatosis and bilateral internal auditory canal metastases from ovarian carcinoma. Radiol Case Rep. 2017;12:386-390.
9. Waldron JS, Cha S. Radiographic features of intramedullary spinal cord tumors. Neurosurg Clin N Am. 2006;17:13-19.

Case Report

Mol Imaging Radionucl Ther 2026;35(2):145-149 **DOI:***10.4274/mirt.galenos.2026.02779*

^{18}F-FDG PET/CT in Progressive Oncocytic Carcinoma of the Parotid Gland-Case Study

Parotis Bezinin İlerleyici Onkositik Karsinomunda ^{18}F-FDG PET/BT-Olgu Sunumu

Dushica Todorova Stefanovski[1], Aleksandar Iliev[2], Goran Spirov[1], Sinisha Stojanoski[3], Nevena Manevska[1,3]

[1]*University Institute of Positron Emission Tomography, Skopje, North Macedonia*
[2]*University Clinic for Maxillofacial Surgery Faculty of Dentistry, Ss. Cyril and Methodius University in Skopje, Skopje, North Macedonia*
[3]*Institute of Pathophysiology and Nuclear Medicine Faculty of Medicine, Ss. Cyril and Methodius University in Skopje, Skopje, North Macedonia*

Abstract

Oncocytic carcinoma of the salivary glands is a very rare entity, that mainly presents in the parotid gland, either arises de-novo or is being associated with a benign oncocytoma in up to 50%. Our patient was a 60 years old male with histopathological finding of oncocytic (oxyphilic) carcinoma originating from the parotid gland with metastasis in cervical lymph nodes (postoperative stage IVA, pTNM = pT2 pN2b pMx G2 R0). On the initial preoperative ^{18}F-fluorodeoxyglucose positron emission tomography/computed tomography (PET/CT) increased metabolic activity was seen in level IB and IIA cervical lymph nodes, suspicious for metastasis. Surgical biopsy of the parotid gland revealed oncocytic carcinoma, and then radical surgery was performed. Afterwards, patients started with immunotherapy, but because of disease progression (metastasis in the cervical, axillary, mediastinal lymph nodes and thyroid) detected on the control PET/CT scans, he was switched to chemotherapy. The patient died four years after being diagnosed with the primary cancer.

Keywords: Oncocytic carcinoma, parotid gland, ^{18}F-FDG PET/CT

Öz

Tükürük bezlerinin onkositik karsinomu, çoğunlukla parotis bezinde ortaya çıkan, ya de novo gelişen ya da %50'ye varan oranda benign onkositom ile ilişkili olan çok nadir bir durumdur. Hastamız, parotis bezinden kaynaklanan ve servikal lenf düğümlerine metastaz yapmış onkositik (oksifilik) karsinom histopatolojik bulgusu olan 60 yaşında bir erkekti (ameliyat sonrası evre IVA, pTNM = pT2 pN2b pMx G2 R0). İlk ameliyat öncesi ^{18}F-florodeoksiglukoz pozitron emisyon tomografisi/bilgisayarlı tomografi'de (PET/BT), metastaz şüphesi uyandıran IB ve IIA seviye servikal lenf düğümlerinde artmış metabolik aktivite görüldü. Parotis bezinin cerrahi biyopsisi onkositik karsinomu ortaya çıkardı ve ardından radikal cerrahi uygulandı. Daha sonra hastaya immünoterapi uygulandı, ancak kontrol PET/BT taramalarında saptanan hastalık ilerlemesi (servikal, aksiller, mediastinal lenf düğümlerinde ve tiroidde metastaz) nedeniyle kemoterapiye geçildi. Hasta, primer kanser teşhisinden dört yıl sonra hayatını kaybetti.

Anahtar Kelimeler: Onkositik karsinom, parotis bezi, ^{18}F-FDG PET/BT

Address for Correspondence: Dushica Todorova Stefanovski, University Institute of Positron Emission Tomography, Skopje, North Macedonia
E-mail: dushica.stefanovski@uipet.mk **ORCID ID:** orcid.org/0000-0001-7629-7742
Received: 12.09.2025 **Accepted:** 15.01.2026 **Epub:** 02.04.2026 **Publication Date:** 04.06.2026

Cite this article as: Stefanovski DT, Iliev A, Spirov G, Stojanoski S, Manevska N. ^{18}F-FDG PET/CT in progressive oncocytic carcinoma of the parotid gland-case study. Mol Imaging Radionucl Ther. 2026;35(2):145-149.

Introduction

Oncocytic carcinoma (OC) of the salivary glands is a very rare entity, that either arises de-novo or is being associated with a benign oncocytoma in up to 50% of patients (1). Oncocytoma, is commonly found in the superficial lobe of the parotid gland well-circumscribed and encapsulated. OC is characterized by large polyhedral cells with abundant granular eosinophilic cytoplasm and round to oval vesicular nuclei, sometimes with double nuclei and prominent nucleoli. Recognizing the malignant histological characteristics, such as necrosis, peri-neural spread, pleomorphism, intra-vascular invasion, and distant metastasis are crucial when differentiating between benign and malignant oncocytic tumors (2). Distant metastasis to the cervical lymph nodes, kidneys, lungs, and mediastinum are the main features of this high-grade malignant tumor (3). This type of cancer occurs mainly in the 6th decade with male predominance. Male to female ratio has been reported to be approximately 2:1 (4,5).

Case Report

Our patient was a 60 years old male with left lateral neck lymphadenopathy, who underwent fine needle aspiration biopsy, revealing classification group V. Informed written consent was obtained from the patient before the imaging. Lymph node extirpation followed and pathology report was consistent with malignant neoplasm of epithelial origin, either Hurthle cell thyroid carcinoma or parotid carcinoma. He was referred for thyroid ultrasound, that revealed no thyroid pathology and excluded primary thyroid malignancy. On the other hand, many hypoechoic lesions were detected in the left parotid gland, the largest one in the upper pole ~10 mm, as well as submandibular lymph nodes up to 12 mm, that needed further investigation.

Patient was examined by ear, nose and throat specialist, which revealed thickened mucosa in the region of the left vallecula. Further on, biopsy was performed, that showed no sign of malignancy.

On the initial ^{18}F-fluorodeoxyglucose positron emission tomography/computed tomography (^{18}F-FDG PET/CT) scan left cervical lymph nodes with increased metabolic activity were detected in level IB and IIA [maximum standard uptake values (SUV_{max} =5.2, d=10 mm)], suspicious for metastasis, few metabolically active lesions in the left parotid gland with SUV_{max} up to 4,4 that needed to be investigated and increased metabolic activity (SUV_{max} =5.4) in the region of the left valecula, probably due to recent biopsy. Then surgical biopsy of left parotid gland was performed and finally oral cavity (OC) was revealed as a primary.

The planned surgical procedure included eliminating all residual parotid tissue and ipsilateral cervical lymphatics. The incision encompassed most of the previous incision in the parotid region, then went in a curvilinear fashion posteriorly and inferiorly behind the sternocleidomastoid muscle (SCM), ending near the midline, below the level of the clavicle. Two flaps in the subplatysmal plane (sub-mass in the parotid region) were developed anteriorly and posteriorly. Dissection began with identification of the main trunk of the left facial nerve. Next, the entire superficial and deep lobe of the parotid was removed with preservation of all branches of the facial nerve. Notable mass was found above the temporo-zygomatic branches of the nerve, but with a sufficient cuff of normal tissue between the mass and the nerves. Similarly, in the tail of the parotid, a palpable mass was found near the division of the marginal mandibular branch without direct contact with the nerve. The rest of the parotidectomy was done in the usual fashion without any difficulties.

Neck dissection started with identification of the Spinal accessory nerve in the posterior neck triangle above Erb's point. Then, dissection began from the Trapesius muscle and moved the fibro-fatty tissue of level V anteriorly, sparing the SAN. The lower border of the dissection was below the previous lymphadenectomy and encompassed all fibro-fatty tissue in the supraclavicular region. Dissection proceeded anteriorly above the deep layer of the deep cervical fascia until the carotid sheet was reached. Dissection then started from the anterior border of SCM, removing its fascial covering and proceeding to dissect the entire length of the jugular chain, starting from level II-b, and ending inferiorly at the level of the clavicle. Internal jugular vein was preserved, with only the linguo-facial trunk ligated and transected. Enlarged and somewhat firm nodes were identified in the jugular chain, at level II-a and level III. When the entire SCM was circumferentially freed, the specimen from the posterior neck was flipped under the muscle and connected with the anterior part of the specimen, which was removed "en block." No significant bleeding was encountered; the wound was closed in layers over two Redon drains. Recovery from general anesthesia and subsequent healing was uneventful (Figure 1).

Subsequently the histopathological finding obtained from the operative material revealed oncocytic (oxyphilic) carcinoma originating from the parotid gland with identified metastatic changes in three of total of 28 extirpated lymph nodes (stage IVA, pTNM = pT2 pN2b pMx G2 R0). Postoperative adjuvant radiotherapy was performed. Next year follow up on magnetic resonance imaging (MRI) showed no signs of local recurrence or distant metastasis.

The second PET/CT scan, performed almost two years after surgery was indicated for further investigation of enlarged axillary lymph nodes seen on the follow up CT. PET/CT findings revealed metabolically active lymph nodes in the right neck region level 3 (SUV_{max} =4.1), left supraclavicular region (SUV_{max} =4.4,d~11 mm), metabolically active nodular lesion in the left pectoral muscle (SUV_{max} =3.7,d~13 mm) and enlarged metabolically active bilateral axillary lymph nodes (SUV_{max} =4.4,d~11 mm). All these lesions were suspicious for metastasis (Figure 2). Then bilateral cervical lymph node extirpation was done, followed by extirpation of cutaneous and subcutaneous metastases in left pectoral region. Patient started with immunotherapy pembrolizumab.

Three months later the follow up PET/CT scan revealed disease progression and new sites od metastasis in the cervical lymph nodes and new metabolically active lesion in the thyroid gland, that needed to be correlated with ultrasonography/fine-needle aspiration biopsy (Figure 3).

Ultrasound of the thyroid showed well vascularized hypoechogenic inhomogeneous lesion in the lower part of the left thyroid lobe with microcalcifications. Fine needle aspiration biopsy that was very difficult to perform due to impaired skin due to surgery and radiation therapy (Figure 4) reported Bethesda V classification group, possible metastasis from salivary gland carcinoma.

Patient continued with immunotherapy, but the next PET/CT scan, done 6 months later, showed again disease progression with metastasis in right cervical lymph nodes, mediastinal, bilateral hilar, interpectoral, left brachial and bilateral axillary lymph nodes (Figure 5). Subcutaneous metastasis in right pectoral and skin metastasis in left supraclavicular region were detected as well.

Patient started with chemotherapy, but considering many side effects and his low performance status, two months later agreement with the oncologist was made to cease it, continuing with symptomatic and palliative therapy only. The patient died the next year, four years after being diagnosed with this type of primary cancer.

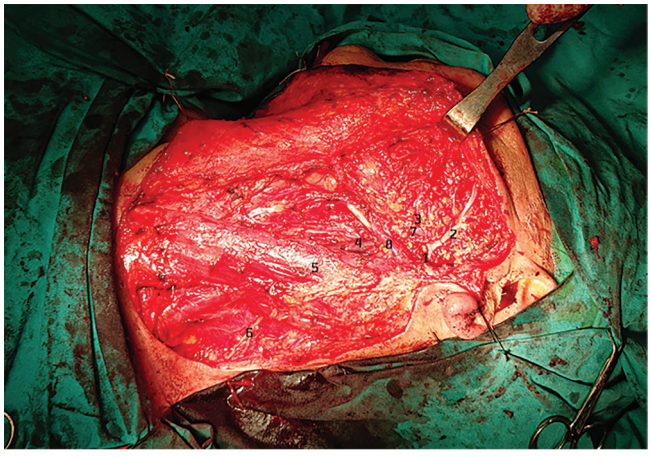

Figure 1. Operative field prior closure
(1) Main trunk of left facial nerve, (2) Temporo-zygomatic branch, (3) Cervico-mandibular branch, (4) Internal jugular vein, (5) Sternocleidomastoid muscle, (6) Accessory nerve, (7) Retromandibular vein, (8) Stylohioid and posterior venter of digastric muscle

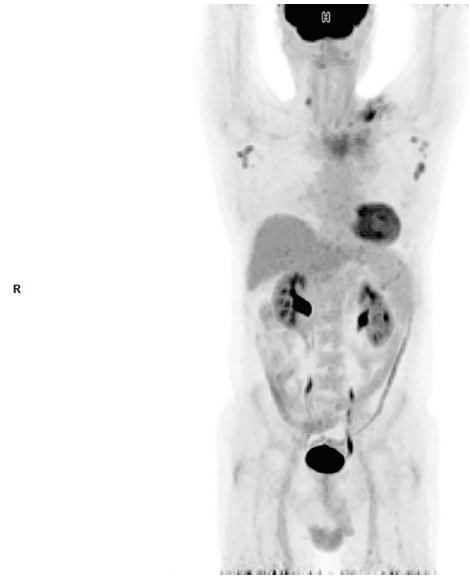

Figure 2. MIP image of the second PET/CT
Right cervical, bilateral axillary, left supraclavicular and lesion in the left pectoral muscle suspicios for metastasis
MIP: Maximum intensity projection, PET/CT: Positron emission tomography/computed tomography

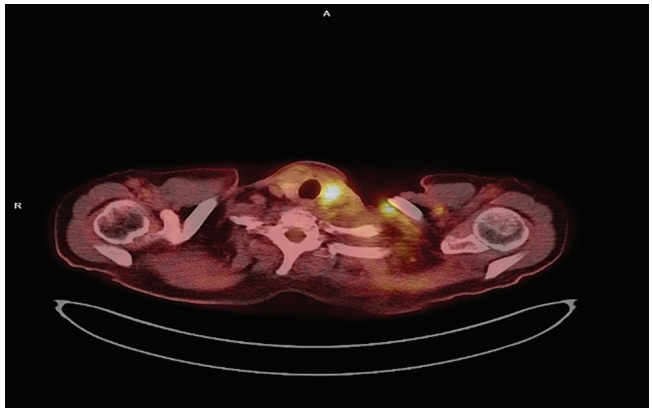

Figure 3. ^{18}F-FDG PET/CT fusion image of thyroid lesion
^{18}F-FDG PET/CT: ^{18}F-fluorodeoxyglucose positron emission tomography/computed tomography

Discussion

OC together with oncocytosis and oncocytoma present very exceptional oncocytic neoplasms of the salivary gland. Very few cases have been reported in the literature so far. It accounts for 11% of all oncocytic salivary gland neoplasms, 0.5% of all epithelial salivary gland malignancies and 0.18% of all epithelial salivary gland tumours (6). In the study of Capone at al. (7) twenty-one parotid oncocytic neoplasms were identified in the period 1984-2000, with OC being the rarest (9.5%), then oncocytosis (28.5%) and the most frequent was oncocytoma (62%).

Figure 4. Skin lesions after surgery and radiation therapy

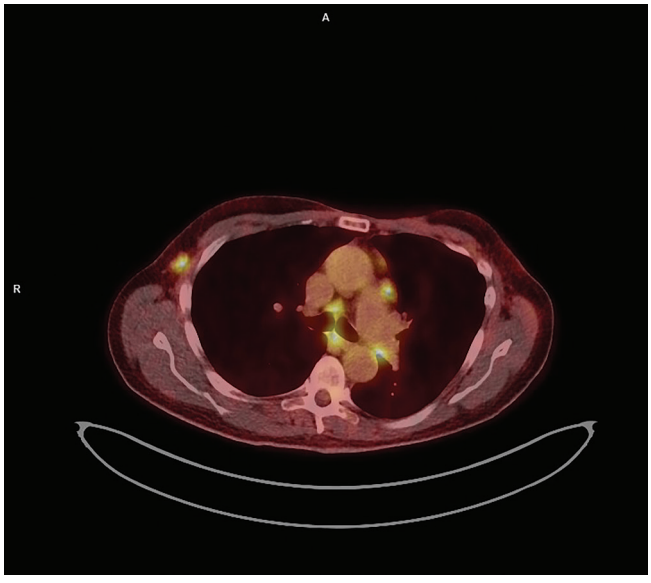

Figure 5. ^{18}F-FDG PET/CT fusion image of lymph node metastasis Mediastinal and right axillar metastasis
^{18}F-FDG PET/CT: ^{18}F-fluorodeoxyglucose positron emission tomography/computed tomography

Since similarities between oncocytic neoplasms do exist, and fine needle aspiration biopsy can not confirm the diagnosis, consequently the patohistology analysis remains the gold standard. Nonetheless, features such as rapid enlargement, facial nerve involvement, or fixation to adjacent structures should be taken into consideration for prompt suspicion for malignancy (8).

The surgical management of parotid oncocytic carcinoma, usually involves a total or partial parotidectomy. This is preferred due to the tumor's aggressive nature and potential for recurrence. Enucleations are usually followed by a recurrence and are not considered as optimal treatment choices, especially given the fact that every subsequent parotid surgery is levels of magnitude more and more difficult and technically complicated. Wherever possible, the facial nerve is dissected and preserved, though extended resections may be necessary if nearby tissues are affected (9).

Neck dissection may also be included in the surgical plan when lymph node involvement is present. The general plan needs to be aggressive since all recurrences have a poor outcome (10).

Cinar et al. (11) reported 48-year-old woman whose disease had metastasized to regional lymph nodes, was treated by radical parotidectomy, with sacrifice of the facial nerve, and radical neck dissection. At the 3-year follow-up, she remained free of disease.

A case of a 70-year-old man was reported by Wan Ahmad Kammal et al. (12) that had a history of left parotid swelling over the past 10 years. A parotid tumor 3x3 cm was identified and grade 4 facial nerve palsy. He was treated with a left total parotidectomy, selective neck dissection and adjuvant radiotherapy with a total dose of 66 Gy within six weeks.

New biomarker research has identified promising prognostic indicators, such as p53 mutations, Ki-67 proliferation index, and mitochondrial DNA mutations. These biomarkers can help predict the tumor's behavior, guiding more tailored decisions about adjuvant radiotherapy and other postoperative treatments. Immunohistochemical markers, including cytokeratins and oncocytic markers, have further refined diagnostic accuracy, enabling more effective surgical planning (13).

Conclusion

According to the Management of Salivary Gland Malignancy in the guideline, ^{18}F-FDG PET/CT has no role when used for the initial evaluation of a parotid mass, but may more accurately predict the extent of nodal and distant metastatic disease in high-grade tumors and identify locoregionally recurrent and metastatic disease. Post-treatment baseline imaging with PET/CT should be obtained 3 months after completion of all treatment (14).

Westergaard-Nielsen et al. (15) found that PET/CT diagnosed cervical lymph node metastases in four patients where MRI did not. These patients were still treated with curative intent, but the surgical procedure with neck dissection was changed based on PET/CT report. Overall, PET/CT changed treatment in three patients with distant metastases and four patients with regional metastases, representing 21% (7/33) of the patients with salivary gland carcinoma.

The prognosis of OC in salivary gland depends primarily on the tumor grade, stage and completeness of resection. The 5-year survival rate for low-grade types goes over 80%-90% and these tumors have favorable outcomes. On the other hand, high-grade carcinoma, show lower 5-year survival ranging between 40% and 60%, due to higher risks of local recurrence, perineural invasion, and metastasis and thus have poorer prognosis (8). Patients with malignant oncocytoma appear to have good short-term survival, but poor long-term survival. The average survival period has been estimated at 3.8 years with metastasizing tumors (3).

Ethics

Informed Consent: Informed written consent was obtained from the patient before the imaging.

Footnotes

Authorship Contributions

Surgical and Medical Practices: D.T.S., A.I., G.S., Concept: S.S., N.M., Design: S.S., N.M., Data Collection or Processing: D.T.S., N.M., Analysis or Interpretation: G.S., Literature Search: D.T.S., N.M., Writing: D.T.S., A.I.

Conflict of Interest: No conflicts of interest were declared by the authors.

Financial Disclosure: The authors declare that this study has received no financial support.

References

1. Lee WY, Chang SL. Fine needle aspiration cytology of oncocytic carcinoma of the submandibular gland with pre-existing oncocytoma: a case report. Cytopathology. 2010;21:339-341.
2. Parmar R, Kalaria AN, Patel KA. Oncocytic lesions of salivary glands: morphological, immunohistochemical, and molecular findings. Cureus. 2024;16:e59328.
3. Gallego L, García-Consuegra L, Fuente E, Calvo N, Junquera L. Oncocytic carcinoma of the parotid gland with late cervical lymph node metastases: a case report. J Med Case Rep. 2011;5:11.
4. Ellis GL, Auclair PL. Tumors of the salivary glands. AFIP Atlas of Tumor Pathology, 4th Series, Fascicle 9. Silver Spring, MD: ARP Press; 2008.
5. Nakada M, Nishizaki K, Akagi H, Masuda Y, Yoshino T. Oncocytic carcinoma of the submandibular gland: a case report and literature review. J Oral Pathol Med. 1998;27:225-228.
6. Lee TH, Lin YS, Lee WY, Wu TC, Chang SL. Malignant transformation of a benign oncocytoma of the submandibular gland: a case report. Kaohsiung J Med Sci. 2010;26:327-332.
7. Capone RB, Ha PK, Westra WH, Pilkington TM, Sciubba JJ, Koch WM, Cummings CW. Oncocytic neoplasms of the parotid gland: a 16-year institutional review. Otolaryngol Head Neck Surg. 2002;126:657-662.
8. Azouaghe Y, Haddadi Z, Zohir M, Banana Y, Sbai AA, Benfadil D, Lachkar A, Idrissi FEAE. Oncocytic carcinoma of the parotid gland: a rare malignancy with diagnostic and therapeutic challenges. Radiol Case Rep. 2025;20:5420-5426.
9. Locati LD, Ferrarotto R, Licitra L, Benazzo M, Preda L, Farina D, Gatta G, Lombardi D, Nicolai P, Vander Poorten V, Chua MLK, Vischioni B, Sanguineti G, Morbini P, Fonseca I, Sozzi D, Merlotti A, Orlandi E. Current management and future challenges in salivary glands cancer. Front Oncol. 2023;13:1264287.
10. Westergaard-Nielsen M, Godballe C, Andersen LJ, Primdahl H, Kristensen CA, Andersen E, Bjørndal K. Oncocytic carcinoma of the salivary glands: a Danish national study. Auris Nasus Larynx. 2018;45:825-830.
11. Cinar U, Vural C, Basak T, Turgut S. Oncocytic carcinoma of the parotid gland: report of a new case. Ear Nose Throat J. 2003;82:699-701.
12. Wan Ahmad Kammal WS, Azman M, Salleh AA, Md Pauzi SH, Abd Shukor N. Parotid gland oncocytic carcinoma: a rare entity in head and neck region. Malays J Pathol. 2020;42:283-286.
13. Alshammari A, Aljufairi E, Alsayed A. Oncocytic mucoepidermoid carcinoma of the parotid gland: case report. J Surg Case Rep. 2022;2022:rjac039.
14. Geiger JL, Ismaila N, Beadle B, Caudell JJ, Chau N, Deschler D, Glastonbury C, Kaufman M, Lamarre E, Lau HY, Licitra L, Moore MG, Rodriguez C, Roshal A, Seethala R, Swiecicki P, Ha P. Management of salivary gland malignancy: ASCO guideline. J Clin Oncol. 2021;39:1909-1941.
15. Westergaard-Nielsen M, Rohde M, Godballe C, Eriksen JG, Larsen SR, Gerke O, Nguyen N, Nielsen MK, Nielsen AL, Thomassen A, Asmussen JT, Diaz A, Høilund-Carlsen PF, Bjørndal K. Up-front F18-FDG PET/CT in suspected salivary gland carcinoma. Ann Nucl Med. 2019;33:554-563.

Review

Mol Imaging Radionucl Ther 2026;35(2):150-156 ***DOI:****10.4274/mirt.galenos.2026.84704*

Comparative Insights into ^{18}F-FDG and ^{68}Ga-FAPI PET Imaging in Glioma: Diagnostic Value, Tumor Grading, and Clinical Implications

Gliomada ^{18}F-FDG ve ^{68}Ga-FAPI PET Görüntülemeye İlişkin Karşılaştırmalı Bilgiler: Tanısal Değer, Tümör Derecelendirmesi ve Klinik Çıkarımlar

Raydel BrianKwee Amalo, Hendra Budiawan, Budi Darmawan

Universitas Padjajaran, Hasan Sadikin General Hospital,Faculty of Medicine, Department of Nuclear Medicine and Theranostic Molecular, Bandung, Indonesia

Abstract

Gliomas are the most common primary malignant brain tumors and are characterized by heterogeneous growth and complex biology, which complicate accurate diagnosis and management. While magnetic resonance imaging (MRI) remains the clinical standard, its limitations in delineating tumor margins and distinguishing recurrence from treatment-induced changes highlight the need for complementary molecular imaging. ^{18}F-fluorodeoxyglucose (^{18}F-FDG) positron emission tomography (PET) has been extensively studied, providing valuable prognostic information by reflecting tumor glycolytic activity. However, its diagnostic utility is hampered by high cortical background uptake and by poor sensitivity in detecting low-grade gliomas. Conversely, glioma-68 fibroblast activation protein inhibitor (FAPI) PET targets cancer-associated fibroblasts, offering superior tumor-to-background contrast and improved visualization of infiltrative margins. Comparative studies suggest that FAPI PET better discriminates between low- and high-grade gliomas, correlates with tumor stromal activity, and aids in therapy planning by differentiating true progression from post-treatment changes. Despite these advantages, the evidence base for FAPI remains limited, largely derived from small cohorts and pilot studies. Standardized imaging protocols and larger prospective trials are necessary to validate its role. Overall, ^{18}F-FDG and FAPI PET provide complementary insights into glioma biology, and their integration with MRI and amino acid tracers may refine diagnostic accuracy, therapeutic planning, and prognostic assessment in clinical neuro-oncology.

Keywords: Glioma, ^{18}F-FDG, PET, FAPI, tumor grading, molecular imaging

Öz

Gliomalar, en sık görülen primer malign beyin tümörleridir ve heterojen büyüme ile karmaşık biyoloji göstermeleri nedeniyle doğru tanı ve yönetimi güçleştirir. Manyetik rezonans görüntüleme (MRG), klinik standart olmaya devam etse de tümör sınırlarını belirlemedeki ve nüksü tedaviye bağlı değişikliklerden ayırt etmedeki sınırlılıkları, tamamlayıcı moleküler görüntüleme yöntemlerine olan gereksinimi ortaya koymaktadır. ^{18}F-florodeoksiglukoz (^{18}F-FDG) pozitron emisyon tomografisi (PET), tümörün glikolitik aktivitesini yansıtarak değerli prognostik bilgiler sağlaması nedeniyle kapsamlı biçimde araştırılmıştır. Ancak tanısal yararlılığı, kortekste yüksek arka plan tutulumu ve düşük dereceli gliomaları saptamadaki

Address for Correspondence: Raydel BrianKwee Amalo, Universitas Padjajaran, Hasan Sadikin General Hospital,Faculty of Medicine, Department of Nuclear Medicine and Theranostic Molecular, Bandung, Indonesia
E-mail: ray_amalo@hotmail.com **ORCID ID:** orcid.org/0009-0008-9224-8965
Received: 01.10.2025 **Accepted:** 23.01.2026 **Epub:** 24.03.2026 **Publication Date:** 04.06.2026

Cite this article as: BrianKwee Amalo R, Budiawan AH, Darmawan B. Comparative insights into ^{18}F-FDG and ^{68}Ga-FAPI PET imaging in glioma: diagnostic value, tumor grading, and clinical implications. Mol Imaging Radionucl Ther. 2026;35(2):150-156.

düşük duyarlılık nedeniyle sınırlanmaktadır. Buna karşılık, galyum-68 fibroblast aktivasyon proteini inhibitörü (FAPI) PET, kansere ilişkili fibroblastları hedef alarak daha üstün tümör-arka plan kontrastı ve infiltratif sınırların daha iyi görüntülenmesini sağlar. Karşılaştırmalı çalışmalar, FAPI PET'in düşük ve yüksek dereceli gliomaları ayırt etmede daha başarılı olduğunu, tümör stromal aktivitesi ile korelasyon gösterdiğini ve gerçek progresyonu tedavi sonrası değişikliklerden ayırarak tedavi planlamasına katkı sağladığını düşündürmektedir. Bununla birlikte, bu avantajlara rağmen FAPI'ye ilişkin kanıt temeli halen sınırlıdır ve büyük ölçüde küçük kohortlar ile pilot çalışmalara dayanmaktadır. Rolünün doğrulanabilmesi için standartlaştırılmış görüntüleme protokollerine ve daha büyük, prospektif çalışmalara ihtiyaç vardır. Genel olarak, ^{18}F-FDG ve FAPI PET, glioma biyolojisine ilişkin birbirini tamamlayıcı bilgiler sunmakta; MRG ve amino asit belirteçleri ile birlikte kullanımları, klinik nöro-onkolojide tanısal doğruluğu, tedavi planlamasını ve prognostik değerlendirmeyi geliştirebilir.

Anahtar Kelimeler: Glioma, ^{18}F-FDG, PET, FAPI, tümör derecelendirmesi, moleküler görüntüleme

Introduction

Gliomas are the most common primary malignant brain tumors, characterized by heterogeneous and infiltrative growth. Magnetic resonance imaging (MRI) is the standard imaging modality but has limitations in delineating tumor margins and distinguishing tumor progression from post-treatment changes. Molecular imaging with positron emission tomography (PET) provides complementary information. ^{18}F-florodeoksiglukoz (^{18}F-FDG) PET measures glucose metabolism and is useful for high-grade gliomas (HGG), with uptake correlating with tumor aggressiveness and overall survival, but is limited by high cortical background and reduced sensitivity to low-grade or small lesions (1,2).

Fibroblast activation protein inhibitor (FAPI) PET targets FAP in cancer-associated fibroblasts (CAF), offering high tumor-to-background contrast and better visualization of infiltrative margins. Pilot studies indicate FAPI PET may improve detection of residual or recurrent gliomas and provide prognostic information related to tumor stromal aggressiveness (3-5). Combining FDG and FAPI PET with MRI and advanced analysis may enhance diagnostic accuracy, treatment planning, and prognostic assessment in glioma patients.

Mechanism of Uptake

Molecular imaging with PET provides complementary information to MRI in glioma evaluation. ^{18}F-FDG PET measures glucose metabolism in tumor cells, reflecting the Warburg effect, and is widely used to assess tumor aggressiveness and to grade tumors. However, its clinical utility is limited by high cortical background, reduced sensitivity for low-grade or small lesions, and potential uptake confounded by inflammation or therapy Kawada et al. (6). Glucose loading prior to ^{18}F-FDG PET can enhance tumor-to-background contrast, improving delineation and characterization of gliomas Kim et al. (7).

FAPI-PET, targeting FAP expressed in CAFs, highlights stromal components and infiltrative tumor margins that are often underrepresented on MRI or ^{18}F-FDG PET. This modality offers high tumor-to-background contrast, aiding detection of residual or recurrent gliomas and potentially providing prognostic information related to stromal aggressiveness Mori et al. (4), Djekidel et al. (8). FAPI PET is particularly promising for visualizing infiltrative gliomas and complementing anatomical imaging, although current evidence is limited to pilot studies and small patient cohorts.

Overall, ^{18}F-FDG PET and FAPI PET provide complementary insights into glioma biology, with FDG reflecting metabolic activity and FAPI delineating stromal and infiltrative regions, supporting improved diagnosis, treatment planning, and prognostic assessment.

Diagnostic Value of ^{18}F-FDG PET in Glioma

^{18}F-FDG PET has been widely applied in glioma imaging due to its ability to reflect the glycolytic activity of tumor cells. Early studies, such as Padma et al. (9), demonstrated that higher FDG uptake strongly correlated with tumor grade and poorer survival outcomes, highlighting its prognostic significance. Subsequent work confirmed this trend, showing that standardized uptake values (SUVs) are generally higher in HGG than in low-grade gliomas (LGG) Takahashi et al. (10). This underscores the utility of ^{18}F-FDG PET in assessing tumor aggressiveness and predicting clinical outcomes.

However, the diagnostic accuracy of ^{18}F-FDG PET is limited by the intrinsically high glucose metabolism in normal cortical tissue, which reduces the lesion-to-background contrast, particularly in LGG. Meta-analyses by Nihashi et al. (11) and Zhao et al. (12) consistently showed that while ^{18}F-FDG PET has moderate sensitivity and specificity, amino acid tracers such as ^{11}C-methionine (MET) or ^{18}F-FDG in detecting recurrent gliomas and differentiating tumor tissue from treatment-related changes. Sharma et al. (13) further confirmed this in a direct comparison in which MET-PET was superior to ^{18}F-FDG PET in distinguishing tumor recurrence from post-treatment necrosis or pseudoprogression.

The role of ^{18}F-FDG PET has therefore shifted from primary diagnosis to prognostic evaluation. Treglia et al. (14), in a systematic review of meta-analyses, concluded that ^{18}F-FDG

provides meaningful information in predicting patient outcomes but is less effective than amino acid tracers for lesion detection. Similarly, Wang et al. (15) highlighted that PET, particularly with MET or fluoroethyltyrosine (FET), was more accurate than MRI spectroscopy in detecting recurrence, whereas ^{18}F-FDG was less reliable as a stand-alone tool. An earlier receiver-operating characteristic analysis of irradiated low-grade astrocytomas, Henze et al. (16), also found ^{18}F-FDG PET useful but inferior to MET-PET in distinguishing tumor progression from radiation-induced changes.

Advantages of FAPI PET in Glioma

The diagnostic evaluation of cancer of unknown primary (CUP) has long relied on ^{18}F-FDG PET/computed tomography (CT) as a functional imaging tool, given its ability to detect tumors based on glycolytic activity. However, several studies have consistently demonstrated the limitations of ^{18}F-FDG, particularly in tumors with low glucose metabolism or in anatomical regions with intrinsically high background uptake, such as the brain.

The introduction of FAPI has opened new avenues in molecular imaging. FAP, expressed predominantly in CAFs, is widely present in the stroma of multiple solid tumors but minimally expressed in normal tissues, including the brain. This biological property forms the basis for the high tumor-to-background contrast of glioma-68 (^{68}Ga)-FAPI PET/CT. Kratochwil et al. (17) highlighted the molecular rationale for targeting FAP, emphasizing its role in tumor proliferation, invasion, and stromal remodeling study by Giesel et al. (18) showed that ^{68}Ga-FAPI PET/CT has markedly lower background uptake in normal brain tissue compared to the high physiological uptake of ^{18}F-FDG, resulting in a much higher tumor-to-background ratio (TBR). This feature is particularly important for brain tumors, where ^{18}F-FDG often struggles due to high baseline glucose metabolism, making lesion detection and delineation difficult.

A broader perspective on the application of FAPI imaging was provided by Dendl et al. (19), who described the "perfect symbiosis" between FAP biology and FAPI imaging. While the high uptake in malignant stroma offers a powerful diagnostic advantage, the authors cautioned that FAP expression is not exclusively tumor-specific and may also occur in conditions such as fibrosis, chronic inflammation, or tissue repair, thereby posing a risk of false positives. This consideration is particularly important in neuro-oncology, where reactive gliosis and post-treatment changes are common.

The superiority of FAPI over ^{18}F-FDG in the CUP setting was further supported by the prospective trial by Gu et al. (20) in head and neck CUP. In this study, ^{68}Ga-FAPI PET/CT identified primary tumors in 51% of patients compared to only 25% with FDG PET/CT, with significant improvements in sensitivity, positive predictive value, and overall diagnostic accuracy. Importantly, the implementation of FAPI imaging altered clinical management in nearly one-quarter of patients, underscoring its real-world clinical impact. Although this study focused on head and neck malignancies, the results are directly translatable to CUP in the brain, where the detection of occult primary lesions remains a major diagnostic challenge.

FDG vs. FAPI for Tumor Grading and diagnostic

Recent evidence highlights important differences between^{18}F-FDG and FAPI PET in the assessment of glioma grading. Ruan et al. (21) demonstrated that ^{68}Ga-FAPI-46 uptake increases with glioma grade, with grade IV tumors showing a mean maximum standard uptake value (SUV_{max}) of 5.03 compared to only 1.14 in grade I-II (p=0.02), and exhibiting significantly higher TBR. This reflects the biological reality that FAP expression rises with tumor aggressiveness. In contrast, ^{18}F-FDG PET, as reported by Valentini et al. (22), shows higher uptake in HGG due to increased proliferation, angiogenesis, reflected by higher Ki-67 indices. However, its clinical utility is hampered by the intrinsically high glucose metabolism of normal cortex, resulting in low TBR and making the distinction between LGG and normal brain tissue unclear. A direct head-to-head study by Liu et al. (23) confirmed these limitations: although FAPI SUV_{max} values were generally lower than those of ^{18}F-FDG, the TBR of FAPI was markedly superior because normal brain tissue shows negligible uptake. This allows clearer discrimination between high- and LGG compared with FDG. Supporting these imaging findings, Oster et al. (24) demonstrated that FAPI uptake strongly correlates with FAP expression in tumor tissue, with gliosarcoma showing particularly high tracer accumulation in line with its stromal biology.

Lyu et al. (25) conducted a preliminary study on 25 patients using ^{18}F-FAPI-42 PET/CT. They found significantly higher SUV_{max} and TBR values in HGG compared with LGG. With cut-off values of SUV_{max} 1.20 and TBR 9.09, the diagnostic accuracy was high [area under the curve (AUC) 0.812-0.850]. The strength of FAPI lies in its low background uptake in the normal brain, providing superior contrast compared with FDG. No significant difference was observed between isocitrate dehydrogenase-mutant and wild-type gliomas, suggesting FAPI uptake reflects tumor grade rather than molecular subtype. Study Dev et al. (26), among six high-grade glioma patients, one grade IV lesion demonstrated ^{68}Ga-FAPI-04 uptake with SUV_{max}=2.8, corresponding to MRI enhancing regions and FET PET uptake. While the study primarily classified lesions

as FAPI-positive vs. FAPI-negative (based on uptake above background), it did not provide detailed per-grade averages or TBR values. Study by Kosaka et al. (27) reported that HGG (World Health Organization grade III-IV) showed an average SUV_{avg} of 8.6±2.7 and SUV_{max} of 11.6±3.7, higher than brain metastases, but with significant overlap that reduces discriminatory value. Dunet et al. (28) confirmed that ^{18}F-FDG reflects tumor aggressiveness. However, in (grade I-II), ^{18}F-FDG uptake is low and often indistinguishable from normal cortex, yielding only 38% sensitivity and a poor AUC (0.40). In contrast, HGG typically present with higher SUV_{max} values, yet specificity remains limited (86%) due to overlap with other enhancing lesions. This trend was reinforced by Pietrzak et al. (29), who retrospectively analyzed over 14,000 ^{18}F-FDG PET/CT scans and found that primary brain tumors had a mean SUV_{max} of 9.2±4.7, metastases were even higher at 12.4±5.6, while benign lesions remained low at ~1.0. Importantly, the range of uptake in primary tumors was broad (1.2-25.0), indicating that although HGG are generally more hypermetabolic than LGG, the absolute differences are often obscured by overlapping values. Katsanos et al. (30) performed a meta-analysis of 23 studies (994 patients) comparing ^{18}F-FDG with amino-acid tracers. ^{18}F-FDG had lower sensitivity (63%) but higher specificity (89%) than ^{11}C-MET (94% sensitivity, 55% specificity) and ^{18}F-FET (88% sensitivity, 57% specificity). Thus, high ^{18}F-FDG uptake is specific for high-grade glioma, but many high-grade cases may be missed because ^{18}F-FDG uptake has low sensitivity, highlighting the need for complementary tracers such as FAPI. Quartuccio et al. (31) reviewed 22 studies on ^{18}F-FDG PET combined with MRI. The combined approach consistently outperformed either modality alone, particularly in distinguishing HGG and in differentiating tumor recurrence from radionecrosis. The integration of PET metabolic parameters (SUV, T/N ratio) with MRI functional markers (apparent diffusion coefficient, cerebral blood volume, Cho/Cr) yielded AUC values >0.90. This shows that ^{18}F-FDG PET, despite its limitations, remains valuable when combined with advanced MRI, offering complementary metabolic information. Overall, ^{18}F-FDG PET demonstrates a clear trend of increased uptake with higher glioma grade, but its main limitations are poor contrast in LGG and considerable overlap with metastatic lesions and normal brain tissue. The comparison summary is shown in Table 1.

Implications for Therapy Planning and Monitoring

Accurate delineation of tumor extent is critical for effective neurosurgical intervention and radiotherapy planning in glioma patients. Conventional MRI often fails to precisely define tumor margins, particularly in infiltrative gliomas, and cannot reliably distinguish treatment-related changes from true tumor progression. Molecular imaging with PET provides complementary functional information that can address these limitations.

^{18}F-FDG PET, which measures glucose metabolism, has been widely used to assess tumor aggressiveness and guide therapy. However, its high uptake in normal cortical tissue can obscure tumor margins, limiting sensitivity for low-grade lesions and complicating early assessment of treatment response Kim et al. (5). PET tracers with higher tumor specificity, such as FAPI, target FAP expressed in CAFs within the tumor stroma, offering high tumor-to-background contrast and enabling visualization of infiltrative tumor regions that may not enhance on MRI Yao et al. (3), Dev et al. (26).

Studies have demonstrated that FAPI PET can effectively differentiate tumor recurrence from post-treatment changes, which is essential for determining whether additional therapy or biopsy is needed Dev et al. (26). Furthermore, pilot studies suggest that pre-radiotherapy FAPI PET can improve delineation of radiation target volumes, ensuring that infiltrative areas are included while minimizing exposure to normal tissue Yao et al. (3). The PET/RANO report by Galldiks et al. (32) emphasizes that PET imaging contributes to more precise radiotherapy planning and monitoring, allowing early detection of nonresponding tumor regions and informing adaptive treatment strategies to enhance therapeutic efficacy while reducing toxicity.

Limitations and Future Perspectives

Despite promising results, the clinical adoption of FAPI PET in glioma remains limited. Current evidence primarily derives from case series or pilot studies with small cohorts, thereby restricting the generalizability of the findings (8,26,33,34). While FAPI PET demonstrates high tumor-to-background contrast and the ability to visualize infiltrative tumor regions, standardized imaging protocols are lacking and diagnostic thresholds have not yet been validated.

Preliminary studies suggest that FAPI PET can differentiate tumor recurrence from post-treatment changes and may provide prognostic information related to stromal activity and aggressiveness Dev et al. (26), Hua et al. (34). Furthermore, combining FAPI PET with other tracers, such as amino acid PET (^{11}C-MET, ^{18}F-FET), could offer complementary information, potentially improving clinical decision-making and therapy planning Chandekar et al. (33), Djekidel et al. (8). To establish its clinical utility, larger prospective trials are required to assess reproducibility, diagnostic accuracy, and prognostic value in glioma patients.

Table 1. Comparison of ^{18}F-FDG and FAPI PET in glioma grading and diagnostic performance across key studies

Study	Tracer/method	Key findings	Implications for glioma grading
Ruan et al. (21), (2024)	^{68}Ga-FAPI-46 PET/CT	SUV_{max} ↑ with grade (grade IV = 5.03 vs. grade I-II=1.14, p=0.02); TBR significantly higher.	FAPI uptake reflects tumor aggressiveness; superior contrast vs. FDG.
Valentini et al. (22), 2017	^{18}F-FDG PET	Higher uptake in high-grade gliomas linked to proliferation, angiogenesis, Ki-67.	Confirms metabolic aggressiveness, but limited by high cortical background (low TBR).
Liu et al. (23), 2024	^{18}F-FDG vs. FAPI PET/CT	FDG SUV_{max} > FAPI SUV_{max}, but FAPI TBR > FDG (normal brain negligible uptake).	FAPI allows clearer discrimination of glioma grade.
Oster et al. (24), 2024	^{68}Ga-FAPI-46 PET + tissue	FAPI uptake strongly correlates with FAP expression; gliosarcoma shows very high uptake.	Validates biological basis of FAPI PET, esp. in stromal-rich tumors.
Lyu et al. (25), 2022	^{18}F-FAPI-42 PET/CT (25 pts)	HGG had higher SUV_{max} and TBR than LGG; cutoff SUV_{max} 1.20 (AUC 0.812), TBR 9.09 (AUC 0.850).	FAPI provides high diagnostic accuracy, independent of IDH status.
Dev et al. (26), 2024	^{68}Ga-FAPI-04 PET/CT vs. FET (6 patients)	5/6 recurrences detected by both FAPI and FET; 1 negative consistent with treatment change. example grade IV lesion SUV_{max}=2.8	Shows FAPI highlights recurrent high-grade gliomas with high contrast; useful in differentiating recurrence vs. treatment effects.
Kosaka et al. (27), 2008	^{18}F-FDG PET	HGG: SUV_{avg} 8.6±2.7, SUV_{max} 11.6±3.7; higher than brain metastases, but overlapping values.	Uptake higher in HGG, but overlap reduces specificity.
Dunet et al. (28), 2015	^{18}F-FDG PET	In LGG, FDG uptake often indistinguishable from cortex; sensitivity only 38%, AUC 0.40.	FDG unreliable in LGG detection; better in HGG.
Pietrzak et al. (29), 2021	^{18}F-FDG PET/CT (14,000 scans)	Primary brain tumors SUV_{max}=9.2±4.7; metastases=12.4±5.6; benign ~1.0; wide range (1.2-25.0).	Confirms trend of ↑ uptake with grade, but overlap with metastases.
Katsanos et al. (30), 2019	Meta-analysis FDG vs. MET/FET	FDG: sensitivity 63%, specificity 89%; MET/FET: higher sensitivity but lower specificity.	FDG highly specific for HGG, but low sensitivity → many missed cases.
Quartuccio et al. (31), 2020	^{18}F-FDG PET + MRI (22 studies)	PET+MRI > PET or MRI alone; AUC >0.90 for grading and recurrence detection.	Multimodal imaging maximizes accuracy; FDG retains complementary value.

^{18}F-FDG: ^{18}F-fluorodeoxyglucose, FAPI: Fibroblast activation protein inhibitor, PET/CT: Positron emission tomography/computed tomography, SUV_{max}: Maximum standardized uptake value, SUV_{avg}: Average standardized uptake value, TBR: Tumor-to-background ratio, FAP: Fibroblast activation protein, HGG: High-grade gliomas, LGG: Low-grade glioma, AUC: Area under the curve, IDH: Isocitrate dehydrogenase, FET: Fluoroethyltyrosine, MRI: Magnetic resonance imaging

Conclusion

^{18}F-FDG PET and FAPI PET each offer distinct and complementary contributions to glioma imaging. ^{18}F-FDG remains a well-established modality for evaluating tumor aggressiveness and predicting outcomes, although its diagnostic accuracy is limited by physiological cortical uptake and by poor sensitivity for low-grade lesions. In contrast, FAPI PET demonstrates superior lesion-to-background contrast, enabling improved delineation of tumor margins, tumor grading, and differentiation of recurrence from post-treatment effects. These properties make FAPI a promising tool for enhancing neurosurgical and radiotherapy planning. Nevertheless, clinical application is still constrained by the paucity of large-scale, standardized studies. Future research should focus on multicenter prospective trials, protocol harmonization, and the integration of FAPI with other tracers to maximize diagnostic and therapeutic impact. Ultimately, a multimodal imaging strategy that combines MRI, FDG, FAPI, and amino acid PET may represent the most effective approach to optimize glioma diagnosis, treatment monitoring, and patient outcomes.

Footnotes

Authorship Contributions

Surgical and Medical Practices: R.B.A., H.B., B.D., Concept: R.B.A., H.B., B.D., Design: R.B.A., H.B., Data Collection or Processing: R.B.A., B.D., Analysis or Interpretation: R.B.A., B.D., Literature Search: R.B.A., H.B., B.D., Writing: R.B.A.

Conflict of Interest: No conflict of interest was declared by the authors.

Financial Disclosure: The authors declared that this study received no financial support.

References

1. Cui M, Zorrilla-Veloz RI, Hu J, Guan B, Ma X. Diagnostic accuracy of PET for differentiating true glioma progression from post treatment-related changes: a systematic review and meta-analysis. Front Neurol. 2021;12:671867.
2. Shahriari A, Ghazanafar Ahari S, Mousavi A, Sadeghi M, Abbasi M, Hosseinpour M, Mir A, Zohouri Zanganeh D, Gharedaghi H, Ezati S, Sareminia A, Seyedi D, Shokouhfar M, Darzi A, Ghaedamini A, Zamani S, Khosravi F, Asadi Anar M. Machine learning-driven radiomics on 18 F-FDG PET for glioma diagnosis: a systematic review and meta-analysis. Cancer Imaging. 2025;25:106.
3. Yao Y, Tan X, Yin W, Kou Y, Wang X, Jiang X, Chen S, Liu Y, Dang J, Yin J, Cheng Z. Performance of 18 F-FAPI PET/CT in assessing glioblastoma before radiotherapy: a pilot study. BMC Med Imaging. 2022;22:226.
4. Mori Y, Dendl K, Cardinale J, Kratochwil C, Giesel FL, Haberkorn U. FAPI PET: fibroblast activation protein inhibitor use in oncologic and nononcologic disease. Radiology. 2023;306:e220749.
5. Kim D, Lee SH, Hwang HS, Kim SJ, Yun M. Recent update on PET/CT radiotracers for imaging cerebral glioma. Nucl Med Mol Imaging. 2024;58:237-245.
6. Kawada K, Iwamoto M, Sakai Y. Mechanisms underlying ^{18}F-fluorodeoxyglucose accumulation in colorectal cancer. World J Radiol. 2016;8:880-886.
7. Kim D, Ko HY, Lee S, Lee YH, Ryu S, Kim SY, Chung JI, Lee M, Moon JH, Chang JH, Yun M. Glucose loading enhances the value of ^{18}F-FDG PET/CT for the characterization and delineation of cerebral gliomas. Cancers (Basel). 2020;12:1977.
8. Djekidel M, Alsadi R, Abi Akl M, Bouhali O, O'Doherty J. Tumor microenvironment and fibroblast activation protein inhibitor (FAPI) PET: developments toward brain imaging. Front Nucl Med. 2023;3:1183471.
9. Padma MV, Said S, Jacobs M, Hwang DR, Dunigan K, Satter M, Christian B, Ruppert J, Bernstein T, Kraus G, Mantil JC. Prediction of pathology and survival by FDG PET in gliomas. J Neurooncol. 2003;64:227-237.
10. Takahashi M, Soma T, Mukasa A, Tanaka S, Yanagisawa S, Momose T. Pattern of FDG and MET distribution in high- and low-grade gliomas on PET images. Clin Nucl Med. 2019;44:265-271.
11. Nihashi T, Dahabreh IJ, Terasawa T. Diagnostic accuracy of PET for recurrent glioma diagnosis: a meta-analysis. AJNR Am J Neuroradiol. 2013;34:944-950, S1-S11.
12. Zhao C, Zhang Y, Wang J. A meta-analysis on the diagnostic performance of (18)F-FDG and (11)C-methionine PET for differentiating brain tumors. AJNR Am J Neuroradiol. 2014;35:1058-1065.
13. Sharma R, D'Souza M, Jaimini A, Hazari PP, Saw S, Pandey S, Singh D, Solanki Y, Kumar N, Mishra AK, Mondal A. A comparison study of (11)C-methionine and (18)F-fluorodeoxyglucose positron emission tomography-computed tomography scans in evaluation of patients with recurrent brain tumors. Indian J Nucl Med. 2016;31:93-102.
14. Treglia G, Muoio B, Trevisi G, Mattoli MV, Albano D, Bertagna F, Giovanella L. Diagnostic performance and prognostic value of PET/CT with different tracers for brain tumors: a systematic review of published meta-analyses. Int J Mol Sci. 2019;20:4669.
15. Wang X, Hu X, Xie P, Li W, Li X, Ma L. Comparison of magnetic resonance spectroscopy and positron emission tomography in detection of tumor recurrence in posttreatment of glioma: a diagnostic meta-analysis. Asia Pac J Clin Oncol. 2015;11:97-105.
16. Henze M, Mohammed A, Schlemmer HP, Herfarth KK, Hoffner S, Haufe S, Mier W, Eisenhut M, Debus J, Haberkorn U. PET and SPECT for detection of tumor progression in irradiated low-grade astrocytoma: a receiver-operating-characteristic analysis. J Nucl Med. 2004;45:579-586.
17. Kratochwil C, Flechsig P, Lindner T, Abderrahim L, Altmann A, Mier W, Adeberg S, Rathke H, Röhrich M, Winter H, Plinkert PK, Marme F, Lang M, Kauczor HU, Jäger D, Debus J, Haberkorn U, Giesel FL. ^{68}Ga-FAPI PET/CT: tracer uptake in 28 different kinds of cancer. J Nucl Med. 2019;60:801-805.
18. Giesel FL, Kratochwil C, Schlittenhardt J, Dendl K, Eiber M, Staudinger F, Kessler L, Fendler WP, Lindner T, Koerber SA, Cardinale J, Sennung D, Roehrich M, Debus J, Sathekge M, Haberkorn U, Calais J, Serfling S, Buck AL. Head-to-head intra-individual comparison of biodistribution and tumor uptake of ^{68}Ga-FAPI and ^{18}F-FDG PET/CT in cancer patients. Eur J Nucl Med Mol Imaging. 2021;48:4377-4385.
19. Dendl K, Koerber SA, Kratochwil C, Cardinale J, Finck R, Dabir M, Novruzov E, Watabe T, Kramer V, Choyke PL, Haberkorn U, Giesel FL. FAP and FAPI-PET/CT in malignant and non-malignant diseases: a perfect symbiosis? Cancers (Basel). 2021;13:4946.
20. Gu B, Yang Z, Du X, Xu X, Ou X, Xia Z, Guan Q, Hu S, Yang Z, Song S. Imaging of tumor stroma using ^{68}Ga-FAPI PET/CT to improve diagnostic accuracy of primary tumors in head and neck cancer of unknown primary: a comparative imaging trial. J Nucl Med. 2024;65:365-371.
21. Ruan D, Sun J, Han C, Cai J, Yu L, Zhao L, Pang Y, Zuo C, Sun L, Wang Z, Tan G, Qu X, Chen H. ^{68}Ga-FAPI-46 PET/CT in the evaluation of gliomas: comparison with ^{18}F-FDG PET/CT and contrast-enhanced MRI. Theranostics. 2024;14:6935-6946.
22. Valentini MC, Mellai M, Annovazzi L, Melcarne A, Denysenko T, Cassoni P, Casalone C, Maurella C, Grifoni S, Fania P, Cistaro A, Schiffer D. Comparison among conventional and advanced MRI, ^{18}F-FDG PET/CT, phenotype and genotype in glioblastoma. Oncotarget. 2017;8:91636-91653.
23. Liu Y, Ding H, Cao J, Liu G, Chen Y, Huang Z. [^{68}Ga]Ga-FAPI PET/CT in brain tumors: comparison with [^{18}F]F-FDG PET/CT. Front Oncol. 2024;14:1436009.
24. Oster C, Kessler L, Blau T, Keyvani K, Pabst KM, Fendler WP, Fragoso Costa P, Lazaridis L, Schmidt T, Feldheim J, Pierscianek D, Schildhaus HU, Sure U, Ahmadipour Y, Kleinschnitz C, Guberina N, Stuschke M, Deuschl C, Scheffler B, Herrmann K, Kebir S, Glas M. The role of fibroblast activation protein in glioblastoma and gliosarcoma: a comparison of tissue, ^{68}Ga-FAPI-46 PET data, and survival data. J Nucl Med. 2024;65:1217-1223.
25. Lyu J, Lin T, Hou P, Liu S, Lai M, Li H, Shan C, Cheng L, Wen X, Cai L, Wang X. The preliminary study for gliomas grading by 18 F-FAPI-42 PET/CT. Oncoradiology. 2022:380-387.
26. Dev ID, Puranik AD, Rangarajan V, Patra S, Purandare N, Sahu A, Choudhary A, Bhattacharya K, Gupta T, Chatterjee A, Dasgupta A, Moiyadi A, Shetty P, Singh V, Sridhar E, Sahay A, Shah A, Ghosh S, Choudhury S, Shah S, Agrawal A. Preliminary evaluation of FAPI-04-PET/CT for differentiating recurrence and post-treatment changes in high-grade gliomas. Explor Target Antitumor Ther. 2024;5:1289-1296.
27. Kosaka N, Tsuchida T, Uematsu H, Kimura H, Okazawa H, Itoh H. ^{18}F-FDG PET of common enhancing malignant brain tumors. AJR Am J Roentgenol. 2008;190:W365-W369.
28. Dunet V, Pomoni A, Hottinger A, Nicod-Lalonde M, Prior JO. Performance of ^{18}F-FET versus ^{18}F-FDG-PET for the diagnosis and grading of brain tumors: systematic review and meta-analysis. Neuro Oncol. 2016;18:426-434.
29. Pietrzak A, Marszałek A, Piotrowski T, Medak A, Pietrasz K, Wojtowicz J, Szweda H, Matuszewski K, Cholewi ski W. Primary and metastatic brain tumours assessed with the brain and torso [^{18}F]FDG PET/CT Study protocol-10 years of single-institutional experiences. Pharmaceuticals (Basel). 2021;14:722.
30. Katsanos AH, Alexiou GA, Fotopoulos AD, Jabbour P, Kyritsis AP, Sioka C. Performance of ^{18}F-FDG, 11C-methionine, and ^{18}F-FET PET for glioma grading: a meta-analysis. Clin Nucl Med. 2019;44:864-869.
31. Quartuccio N, Laudicella R, Vento A, Pignata S, Mattoli MV, Filice R, Comis AD, Arnone A, Baldari S, Cabria M, Cistaro A. The additional value of ^{18}F-FDG PET and MRI in patients with glioma: a review of the literature from 2015 to 2020. Diagnostics (Basel). 2020;10:357.

32. Galldiks N, Niyazi M, Grosu AL, Kocher M, Langen KJ, Law I, Minniti G, Kim MM, Tsien C, Dhermain F, Soffietti R, Mehta MP, Weller M, Tonn JC. Contribution of PET imaging to radiotherapy planning and monitoring in glioma patients - a report of the PET/RANO group. Neuro Oncol. 2021;23:881-893.
33. Chandekar KR, Prashanth A, Vinjamuri S, Kumar R. FAPI PET/CT imaging-an updated review. Diagnostics (Basel). 2023;13:2018.
34. Hua T, Huang Q, Zhou Z, Zhou W, Wen J, Xie F, Li M, Guan Y, Zhuang D. Fibroblast activation protein expression in the tumor microenvironment is crucial in survival prediction and differentiation of recurrent gliomas: a head-to-head comparison of ^{68}Ga-FAPI-04 and ^{18}F-FET in PET/CT imaging. EJNMMI Radiopharm Chem. 2025;10:57.